



# **POLITECNICO**

## **MILANO 1863**

School of Industrial and Information Engineering  
Department of Aerospace Science and Technology

Master of Science in Aeronautical Engineering

### **CONCEPTUAL DESIGN OF A 19-SEATER HYBRID-ELECTRIC AIRCRAFT FOR FUTURE AVIATION**

Supervisor:

**PROF. LORENZO TRAINELLI**

Co-Supervisors:

**PROF. CARLO E. D. RIBOLDI**

**PROF. ALBERTO L. M. ROLANDO**

Author:

**DANIELE SPADEA**  
**(898305)**

Academic Year 2019-2020

This page has been intentionally left blank.

*Thanks to my family and friends,  
that have been always patient  
and still bear with me.*

This page has been intentionally left blank.



## Sommario

Il trasporto aereo ha visto una crescita sempre più importante fin dalla sua nascita, ed è destinato ad espandersi ulteriormente. Questo mezzo di trasporto era riservato principalmente a lunghi viaggi, ma diventerà più fruibile anche negli spostamenti di media e breve durata grazie a servizi più dinamici come *miniliner* e *microfeeder*. Le aspettative di evoluzione del sistema di trasporto hanno attivato una intensificazione degli sforzi di ricerca per ridurre l'impatto ambientale dell'aviazione. Diversi progetti sono nati in questa direzione, tra cui *UNIFIER19*, un velivolo 19 posti a *quasi-zero emissioni* che ambisce ad essere "*facile come un autobus*". In questo documento fornisco il mio contributo verso un'aviazione ecosostenibile attraverso l'analisi e la selezione di una configurazione candidata per il progetto UNIFIER19.

Il processo di selezione è diviso in tre blocchi. Inizialmente, varie tecnologie vengono analizzate e combinate tra loro in una varietà di velivoli che spazzano un ampio spazio di progetto. Successivamente, un metodo decisionale multi criterio (MCDM) viene utilizzato per condurre la selezione qualitativa di alcuni promettenti aerei candidati. Infine, le alternative vengono dimensionate, analizzate e confrontate per evidenziare la più idonea rispetto agli obiettivi di progetto.

Il velivolo identificato ha un tradizionale layout del tipo tubo-ala con coda posteriore e propulsione elettrica distribuita (DEP). Sfrutta i benefici dell'interazione propulsione-velivolo per aumentare l'efficienza aerodinamica attraverso un'ala soffiata dotata di eliche d'estremità (WTP), e per migliorare l'efficienza propulsiva grazie ad un elica di coda (TCP) che consente l'ingestione dello strato limite (BLI). Elevate capacità di missione ed eccezionali prestazioni ambientali sono garantite con un'architettura ibrido-elettrica di tipo serie che conta su delle celle a combustibile alimentate da un sistema di stoccaggio dell'idrogeno in forma liquida (LH2).

This page has been intentionally left blank.

## Abstract

Aerial transport has always seen a fast growth since its birth, and it is bound to expand further. This means of transport was mainly reserved for long travel, but it is getting more suitable also in mid and short time transfers thanks to more dynamic services such as *miniliner* and *microfeeder*. Expectations on the evolution of transport system prompted an intensification of efforts to reduce the environmental impact of aviation. Many projects were born in this direction, among these *UNIFIER19*, a 19-seater *Near-Zero Emission* (NZE) aircraft that aims to be "as easy as a bus". In this document I give my contribution towards an eco-friendly aviation through the analysis and selection of a candidate configuration for the UNIFIER19 project.

The selection procedure is divided into three blocks. Initially, many technologies are analyzed and combined together in a variety of aircraft that sweep a vast design space. Then, a Multi Criteria Decision Making (MCDM) method is used to conduct the qualitative selection of a few promising candidate airplanes. Finally, the alternatives are sized, analyzed and compared to highlight the most suitable one with respect to the design goals.

The identified aircraft has a traditional tube-and-wing layout with aft-tail and Distributed Electric Propulsion (DEP). It exploits the benefits of propulsion-airframe interactions to increase aerodynamic efficiency through a blown wing equipped with Wing Tip Propellers (WTP), and to enhance propulsive efficiency thanks to a Tail Cone Propeller that enables Boundary Layer Ingestion (BLI). Great mission capabilities and outstanding environmental performance are ensured with a serial hybrid-electric architecture that relies on fuel cells fed by a Liquid Hydrogen storage system (LH2).

This page has been intentionally left blank.

# Contents

<b>Acknowledgements</b>	<b>I</b>
<b>List of Figures</b>	<b>III</b>
<b>List of Tables</b>	<b>V</b>
<b>Nomenclature</b>	<b>VII</b>
<b>Acronyms</b>	<b>XI</b>
<b>1 Introduction</b>	<b>1</b>
1.1 Motivation . . . . .	1
1.2 Background . . . . .	2
1.3 Aim . . . . .	3
1.4 Method . . . . .	4
1.5 Structure of the Work . . . . .	5
<b>2 Design Space and Technology Review</b>	<b>7</b>
2.1 Overview . . . . .	7
2.2 Multi-Criteria Decision-Making . . . . .	10
2.3 Aircraft Layout . . . . .	12
2.3.1 Blended Wing Body . . . . .	12
2.3.2 Box Wing Aircraft . . . . .	13
2.3.3 Truss Braced Wing . . . . .	14
2.4 Aircraft Propulsion . . . . .	14
2.4.1 Hydrogen . . . . .	15
2.4.2 High-lift Propellers . . . . .	16
2.4.3 Wing Tip Propellers . . . . .	17
2.4.4 Boundary Layer Ingestion . . . . .	18
2.4.5 Distributed Electric Propulsion . . . . .	19
2.5 Other Potentially Useful Technologies . . . . .	20
2.5.1 Propulsion Control . . . . .	20
2.5.2 Laminar Flow . . . . .	20
2.5.3 Morphing . . . . .	21
2.6 Similar Works . . . . .	22
<b>3 Candidate Configurations</b>	<b>25</b>
3.1 Design Space . . . . .	25
3.2 Approach to Generation of Candidates . . . . .	27
3.3 Initial List of Candidates . . . . .	27

<b>4</b>	<b>Qualitative Selection</b>	<b>31</b>
4.1	Initial Selection . . . . .	31
4.1.1	Method . . . . .	31
4.1.2	Further Candidates . . . . .	32
4.1.3	Results . . . . .	33
4.2	Accurate Selection . . . . .	34
4.2.1	Method . . . . .	34
4.2.2	Remarks on Ratings . . . . .	39
4.2.3	Results . . . . .	41
4.3	Candidate Configurations . . . . .	42
<b>5</b>	<b>Sizing Methodology</b>	<b>43</b>
5.1	Description of Sizing Tools . . . . .	43
5.1.1	Hyperion . . . . .	43
5.1.2	Argos . . . . .	44
5.1.3	Titan . . . . .	46
5.2	Modelling of New Technologies . . . . .	46
5.3	Strut Braced Wing . . . . .	48
5.3.1	Method . . . . .	49
5.3.2	Results . . . . .	52
5.3.3	Validation . . . . .	53
<b>6</b>	<b>Quantitative Selection</b>	<b>59</b>
6.1	Input Data . . . . .	59
6.1.1	Mission Requirements . . . . .	60
6.1.2	Baseline Aircraft . . . . .	61
6.1.3	Technology Level . . . . .	62
6.2	Results . . . . .	63
6.3	Final Assessment . . . . .	67
<b>7</b>	<b>Conclusion</b>	<b>69</b>

## **Bibliography**

<b>A</b>	<b>Strut Braced Wing Analytical Modeling</b>	<b>i</b>
A.1	Problem Setup . . . . .	i
A.1.1	Load Distributions . . . . .	i
A.1.2	Section Properties . . . . .	iv
A.2	Cantilever Wing . . . . .	iv
A.2.1	Nondimensionalization . . . . .	v
A.2.2	Reactions . . . . .	vi
A.2.3	Internal Forces . . . . .	vii
A.2.4	Stress . . . . .	ix
A.2.5	Mass . . . . .	x
A.3	Strut Braced Wing . . . . .	xi
A.3.1	Nondimensionalization . . . . .	xii
A.3.2	Reactions . . . . .	xiii
A.3.3	Internal Forces - First Chunk . . . . .	xiv
A.3.4	Internal Forces - Second Chunk . . . . .	xv
A.3.5	Internal Forces - Complete . . . . .	xvi

A.3.6	Internal Forces - Strut . . . . .	xvii
A.3.7	Stress . . . . .	xviii
A.3.8	Maximum Stress . . . . .	xx
A.3.9	Strut Buckling . . . . .	xxii
A.3.10	Mass . . . . .	xxiii
A.4	Comparison . . . . .	xxvii
A.5	Validation . . . . .	xxviii
A.6	Others . . . . .	xxxi
A.6.1	Displacements . . . . .	xxxi
A.6.2	Mass comparison coefficient . . . . .	xxxiv
A.6.3	Weight correction factor . . . . .	xxxvi
A.6.4	Aerodynamics . . . . .	xxxvi

This page has been intentionally left blank.



# Acknowledgements

I want to thank my supervisor Prof. Lorenzo Trainelli, and my co-supervisors Prof. Carlo E. D. Riboldi and Prof. Alberto L. M. Rolando. They gave me the fantastic opportunity of dealing with such a delicate and formative task in a great international project, and they helped me learning and proceeding during the entire period of my thesis.

I am immensely grateful to Yasir Mahmood Khan and Francesco Salucci that have been always at my side even during the most hard-working periods.

Along the path of this project I received support from many people, particularly Giulia Rovedatti, Isacco Raimo and Antonio Estrada Briz.

Still thank you to all Pipistrel Vertical Solution, especially to David Eržen for helping us during the validation of our proposal.

This page has been intentionally left blank.

## List of Figures

2.1	NASA N3-X, of interest the adoption of a BWB layout with DEP on the back to exploit also BLI [11]. . . . .	8
2.2	Boeing SUGAR Freeze, evident the presence of BLI and TBW technologies [11]. . . . .	8
2.3	Airbus ZEROe concept aircraft family (above) and the new "Pod" configuration (below) [15]. . . . .	9
2.4	Induced flow factor for various wing configurations [29]. . . . .	13
2.5	PARSIFAL project [30]. . . . .	13
2.6	NASA X-57 featuring a blown wing and WTP [37]. . . . .	17
2.7	Vought V-173 "Flying Pancake", a first application of the WTP. . . . .	18
2.8	Comparison between simplified non-BLI (above) and ideal BLI (below) configuration [42]. . . . .	18
2.9	Blohm & Voss BV 144 that adopted the VIW, of interest the easy boarding thanks to the fuselage closer to ground, and the absence of tail up sweep angle. . . . .	21
2.10	Faradair BEHA [61]. . . . .	23
4.1	Otto Celera 500 L [62]. . . . .	32
4.2	Pairwise comparison matrix for criteria priorities. . . . .	37
4.3	Ratings-to-priorities for criterion 3 "Aerodynamic Efficiency". . . . .	38
4.4	Ratings of candidate configurations. . . . .	38
5.1	Flow chart of the outermost Hyperion loop [7]. . . . .	44
5.2	Flow chart of the outermost Argos loop [8]. . . . .	45
5.3	Flow chart of Titan [8]. . . . .	47
5.4	Nondimensional lift distribution comparison. . . . .	50
5.5	Double plate (above) and semi-monocoque (below) structural idealizations of a wing section. . . . .	51
5.6	Bending moment comparison for different $\chi_s$ . . . . .	53
5.7	Wing mass comparison among various statistical equations valid for commercial aircraft and the proposed analytical model. . . . .	54
5.8	Wing mass comparison between the typical region occupied by sailplanes (i.e. high aspect ratio wings) and the proposed analytical model. . . . .	55
5.9	Mass of cantilever wing and strut braced wing calculated with statistical equations from Cessna Method. . . . .	56
5.10	Strut braced wing mass comparison between Cessna Method and the analytical model. . . . .	57
6.1	Cabin layout of the Cessna 408 SkyCourier [72]. . . . .	62

6.2	Distance and true airspeed over the mission (C6). . . . .	66
6.3	Altitude, throttle, fuel and battery levels along the mission (C6). . .	66
6.4	Schematic representation of the candidate configuration (C6). . .	68
A.1	Cantilever wing scheme and nomenclature. . . . .	v
A.2	Cantilever wing reaction forces. . . . .	vi
A.3	Strut-braced wing scheme and nomenclature, with a generic load distribution. . . . .	xi
A.4	Strut-braced wing reaction forces. . . . .	xiii
A.5	Summation of bending stress and normal stress (clarification on presence of absolute value in the stress equation). . . . .	xviii
A.6	Maximum bending moment and its span-wise location for differ- ent $\chi_s$ (numerical solution). . . . .	xxi
A.7	Numerical integration of $I_P(\chi_s)$ , $I_E(\chi_s)$ and $I_L(\chi_s)$ together with their correspondent polynomial interpolations. . . . .	xxvi
A.8	Nondimensional axial force comparison. . . . .	xxvii
A.9	Nondimensional shear force comparison. . . . .	xxviii
A.10	Nondimensional bending moment comparison. . . . .	xxix
A.11	Nondimensional stress comparison. . . . .	xxix
A.12	Nondimensional wing assembly mass comparison (including struts). . . . .	xxx
A.13	Effect of the axial displacement of wing and strut on vertical dis- placement of the wing. . . . .	xxxiii
A.14	Oswald's factor of wing, as function of taper ratio for various as- pect ratio [73]. . . . .	xxxviii

## List of Tables

2.1	A simple example of implementation of the Pugh's matrix. . . . .	11
3.1	Categorized list of technologies options considered in the assembling of candidates. . . . .	26
3.2	Initial list of candidate configurations. . . . .	28
3.2	Initial list of candidate configurations (continued). . . . .	29
4.1	List of candidates at intermediate qualitative selection stage. . . . .	33
4.2	Example of a pairwise comparison matrix used in the AHP. . . . .	35
4.3	The fundamental scale of absolute numbers (from [21]). . . . .	35
4.4	Ranked list of candidates with scores attained in the AHP. . . . .	41
4.5	List of aircraft for sizing and assessments. . . . .	42
5.1	Data and results from various articles compared to those found applying the analytical method developed in this report. Data with * have been assumed. . . . .	58
6.1	Mission requirements during various phases of the design. . . . .	60
6.2	Parameters defining the technological level expected for 2025 (interpolation between 2020 and 2035 of data from [35]). . . . .	62
6.3	Main sizing results with THE architecture. . . . .	64
6.4	Main sizing results with fuel cells based HE architecture and GH2. . . . .	64
6.5	Main sizing results with fuel cells based HE architecture and LH2. . . . .	65
A.1	Coefficients resulting from interpolation of $I_P$ , $I_E$ and $I_L$ , computed through numerical integration for various $\chi_s$ . . . . .	xxvii
A.2	Nomenclature and units adopted <i>only</i> for the statistical equations. . . . .	xxx
A.3	Skin roughness value for different type of aircraft [65]. . . . .	xxxvii

This page has been intentionally left blank.

# Nomenclature

Symbol	Description
$A$	Section area
$A_s$	Section area of strut
$A_0$	Reference section area
$b$	Wing span
$b_0$	Reference wing span
$b_e$	Arm of equivalent dump load
$b_s$	Strut breakpoint
$c$	Chord
$c_0$	Reference chord
$C_i$	Coefficients of polynomial interpolation function (with $i = 0, 1, \dots$ )
$c_s$	Strut chord
$D$	Drag
$E$	Young's modulus
$F$	Load resultant
$GI$	Gravimetric index
$g$	Gravity acceleration
$h_s$	Vertical distance between wing and strut hinges on fuselage
$I_E = I_E(\chi_s)$	Result of numerical integration with elliptical lift distribution
$I_P = I_P(\chi_s)$	Result of numerical integration with parabolic lift distribution
$I_L = I_L(\chi_s)$	Result of numerical integration with linear lift distribution
$L$	Lift
$m$	Mass
$m_0$	Reference mass
$m_{H_2}$	Mass of hydrogen
$m_{MTO}$	Maximum Take Off mass
$m_s$	Strut mass
$m_{\text{tank}}$	Mass of tank
$m_w$	Wing mass
$m_{wa}$	Wing assembly mass (includes strut)
$\tilde{m}$	Nondimensional mass
$M$	Bending moment
$\tilde{M}$	Nondimensional bending moment

Symbol	Description
$M_A$	Reaction moment at point $A$
$M_F$	Moment due to load $F$ (pole at origin)
$n_{\max}$	Maximum load factor
$n_{\min}$	Minimum load factor (maximum negative)
$n_{\text{ratio}}$	Ratio between maximum and minimum load factors
$n_{\text{ult}}$	Ultimate load factor
$N$	Axial force
$N_A$	Reaction force at point $A$
$N_B$	Reaction force at point $B$
$N_C$	Reaction force at point $C$
$N_s$	Axial force of strut
$\tilde{N}$	Nondimensional axial force
$J$	Second area moment of the section
$J_0$	Second area moment of reference section
$PSC$	Power saving coefficient
$P'_P$	Propulsive power (non-BLI)
$P_P$	Propulsive power (BLI)
$q(x)$	Load distribution
$\bar{q}$	Mean load distribution
$\tilde{q}$	Nondimensional load distribution
$q_0$	Load distribution coefficient
$q_1$	Load distribution coefficient
$r_g$	Radius of gyration of the section
$r_{g0}$	Radius of gyration of the reference section
$R_A$	Reaction force at point $A$
$R_B$	Reaction force at point $B$
$R_C$	Reaction force at point $C$
$S$	Wing surface
$t$	Thickness of airfoil
$t_s$	Strut thickness
$(t/c)$	Thickness-to-chord ratio
$(t/c)_s$	Thickness-to-chord ratio of strut
$T$	Shear force
$\tilde{T}$	Nondimensional shear force
$x$	Spanwise coordinate
$V_0$	Free stream velocity
$y_{\max}$	Maximum distance from the elastic axis of section
$W_{\min}$	Section modulus
$W_{\min 0}$	Section modulus of the reference section
$\alpha$	Angle between strut and wing
$\Delta$	Ratio between cantilever wing span and strut braced wing span on comparison
$\eta'_P$	Propulsive efficiency (non-BLI)
$\gamma_s$	Nondimensional vertical distance between wing and strut hinges on fuselage



Symbol	Description
$\gamma_{s,0}$	Nondimensional vertical distance between wing and strut hinges on fuselage (with respect to reference wing span)
$\kappa_{opt}$	Structural optimization level
$\lambda$	Aspect ratio
$\lambda_0$	Reference aspect ratio
$\ell$	Beam length (half of wing span)
$\ell_e$	Arm of the equivalent dump load
$\ell_s$	Strut length
$\rho$	Density
$\sigma$	Stress
$\sigma_{lim}$	Strength limit of material
$\sigma_{max}$	Maximum allowed stress
$\sigma_{s,cr}$	Critical stress for strut buckling
$\tilde{\sigma}$	Nondimensional stress
$\chi$	Nondimensional span coordinate
$\chi_{s,opt}$	Optimal nondimensional strut breakpoint (for minimum stress)
$\chi_s$	Nondimensional strut breakpoint
$\xi$	Spanwise coordinate (integration variable)
$\zeta$	Nondimensional span coordinate (integration variable)

This page has been intentionally left blank.

# Acronyms

Acronym	Definition
<b>AAW</b>	Active Aeroelastic Wing
<b>ACARE</b>	Advisory Council for Aeronautics Research in Europe
<b>ACTE</b>	Active Compliant Trailing Edge
<b>AHP</b>	Analytical Hierarchy Process
<b>ARGOS</b>	AiRcraft GeOmetric Sizing
<b>BEHA</b>	Bio Electric Hybrid Aircraft
<b>BLI</b>	Boundry Layer Ingestion
<b>BWA</b>	Box Wing Aircraft
<b>BWB</b>	Blended Wing Body
<b>CS</b>	Clean Sky Programme
<b>CS2</b>	Clean Sky 2 Programme
<b>CSJU</b>	Clean Sky Joint Undertaking
<b>DAER</b>	Department of AERospace science and technologies
<b>DEP</b>	Distributed Electric Propulsion
<b>DLR</b>	Deutsches Zentrum für Luft- und Raumfahrt, also known as German Aerospace Center
<b>FC</b>	Fuel Cells
<b>FEM</b>	Finite Element Method
<b>FMSlab</b>	Flight Mechanics & Flight Systems Laboratory
<b>GA</b>	General Aviation
<b>GH<sub>2</sub> or GH2</b>	Gaseous Hydrogen storage system
<b>HE</b>	Hybrid Electric
<b>HLFC</b>	Hybrid Laminar Flow Control
<b>HYPERION</b>	HYbrid PERformance SimulatIOn
<b>IATA</b>	International Air Transport Association
<b>ICE</b>	Internal Combustion Engine
<b>JWA</b>	Joined Wing Aircraft
<b>LEAPTech</b>	Leading Edge Asynchronous Propellers Technology
<b>LSA</b>	Light Sport Aircraft
<b>LH<sub>2</sub> or LH2</b>	Liquid Hydrogen storage system
<b>MAC</b>	Mean Aerodynamic Chord
<b>MAHEPA</b>	Modular Approach to Hybrid Electric Propulsion Architecture
<b>MAVERIC</b>	Model Aircraft for Validation and Experimentation of Robust Innovative Controls
<b>MDO</b>	Multidisciplinary Design Optimization
<b>MSE</b>	Mean Square Error

<b>Acronym</b>	<b>Definition</b>
<b>MTOM</b>	Maximum Take Off Mass
<b>NLF</b>	Natural Laminar Flow
<b>NZE</b>	Near-Zero Emission
<b>OASPL</b>	OverAll Sound Pressure Level
<b>PARSIFAL</b>	Prandtl ARchitecture for the Sustainable Improvement of Future AirpLanes
<b>PAX</b>	Passenger
<b>PCA</b>	Propulsion Controlled Aircraft
<b>PE</b>	Pure Electric
<b>PEM</b>	Proton Exchange Membrane
<b>POLIMI</b>	Politecnico di Milano
<b>PVS</b>	Pipistrel Vertical Solution
<b>SBW</b>	Strut Braced Wing
<b>SMP</b>	Sizing Matrix Plot
<b>SRA</b>	Strategic Research Agenda
<b>STARC-ABL</b>	Single-aisle Turboelectric Aircraft with Aft Boundary-Layer Propulsion
<b>SUGAR</b>	Subsonic Ultra Green Aircraft Research
<b>TBO</b>	Time Between Overhaul
<b>TBW</b>	Truss Braced Wing
<b>TCP</b>	Tail Cone Propeller
<b>TRL</b>	Technology Readiness Level
<b>TSA</b>	Three Surface Aircraft
<b>TUDELFT</b>	Delft University of Technology
<b>T&amp;W</b>	Tube and Wing (type of aircraft layout)
<b>WP</b>	Work Package
<b>WTP</b>	Wing Tip Propeller

# 1. Introduction

The modern world is facing the climate change problem and our society is demanding an ever-increasing dense air transportation network. As a result, in the near future the aeronautical industry will provide new types of aircraft capable of satisfying travellers' needs while taking care of Earth's environment. In this document, I present my contribution in designing one of these new aircraft in the framework of the Clean Sky UNIFIER19 project.

This chapter includes an outline of the UNIFIER19 project, an outline of its state and a description of what is carried out within this document.

## 1.1. Motivation

It is often argued that humans had a major impact on Earth's climate system and caused climate change on a global scale, with large-scale shifts in weather patterns resulting from global warming. The largest source of warming is the emission of greenhouse gases (mainly CO<sub>2</sub>). Fossil fuel burned for energy consumption is the main contribution to these emissions.

The environmental impact of aviation accounts for about 3% of global man-made CO<sub>2</sub> emissions and is going to increase even more in the next years (about 4 times before 2050), as modern society demands enhanced connection among people and places [1]. But aeronautics is known for its ability to innovate, in fact a strong research effort persists since many years and powerful solutions to minimize the environmental impact of aviation are close to be delivered.

Aerospace is one of Europe's excellences and the European aeronautical industry is a worldwide co-leader. Back in 2000, Europe recognized the importance of aviation and grouped key stakeholders to agree on how aviation could meet society demands. The result was a report named *"European Aeronautics: A vision for 2020"* published in 2001 [2], and the consequent establishment of ACARE (Advisory Council for Aeronautics Research in Europe) to develop and maintain a Strategic Research Agenda (SRA) that would help achieve the goals of Vision 2020.

Various changes collected over years induced ACARE to reconsider and extend Vision 2020 to a new horizon towards 2050. In 2011 ACARE published its new vision, *Flightpath 2050* [3].

The vision covers several aspects of the aviation world such as safety, traffic management, industry and leadership, research and education, goals for emission reductions, etc. Between them, two are of particular interest to understand the motivations that led to the UNIFIER19 project.

The first point is that environmental protection has been and remains a prime driver in the development of air vehicles. This means that aircraft will be more environmentally friendly, with significant lower noise and chemical emissions.

The second point is that the air transport is going to be highly integrated with ground infrastructure allowing 90 % of travellers within Europe to complete their journey, door-to-door within 4 hours. Major hubs, secondary airports, vertiports and heliports, will be seamlessly connected within a multimodal transport system. Airport will operate at high utilization levels with highly efficient operations even through night thanks to new much quieter aircraft.

The European Flightpath 2050 satisfies the demands of european citizen as also demonstrated by market studies made for UNIFIER19 [4]. Similar findings were highlighted also in the american aerial transportation network [5]. These studies indicates a potential market demand for a new kind of air trasport that could reduce travel time by enabling direct point-to-point aerial transfer from local community airports. This new air mobility network would allow for greater growth in commercial air travel by adding a lot of underused small airports to relieve the major hubs.

The Clean Sky Joint Undertaking (CSJU) is a partnership launched in 2008 between the European Commission and the European aviation industry, that coordinates and funds researches with the aim to provide environmental sustainable aircraft, with minimal acoustic and chemical emissions. The CSJU manages the Clean Sky Programme (CS) and the Clean Sky 2 Programme (CS2). Clean Sky 2 was launched in 2014 following the success of the initial CS, and it contributes to advance towards the european vision Flightpath 2050.

The UNIFIER19 project [6] is funded by CSJU and it deals with an innovative aircraft that will enable European Flightpath 2050 vision by offering a sustainable and cost-efficient air mobility solution. This is a 19-passenger Near-Zero-Emission (NZE) aircraft intended to provide a diffused service connecting smaller airports to each other (*miniliner*) and with hubs (*microfeeder*), for both scheduled and on-demand shuttle flights. This concept allows exploiting the sparse, underused European small airport network to offer a new mobility experience, "as easy as a bus".

## 1.2. Background

The UNIFIER19 project is implemented into four Work Packages (WP) and it includes three major partners, namely: Politecnico di Milano (POLIMI), Delft University of Technology (TUDELFT) and Pipistrel Vertical Solutions (PVS). The first two are universities while the latter is an aircraft manufacturer at the forefront of innovation, acting as the project coordinator.

The first WP, "*The Design Framework*", had the main tasks of identifying potential markets for the aircraft family, define its design requirements, define performance metrics to be applied during WP2 and identify the set of applicable airframe and propulsion architectures.

The second WP, "*Initial Concurrent Design Competition*" is ongoing at the time of writing. POLIMI and TUDELFT are performing design activities in a concurrent manner with the help of PVS (Pipistrel Vertical Solution). As an output from these conceptual loops, two candidate aircraft configurations have been proposed, one by POLIMI and one by TUDELFT. Further analysis and assessments will be performed on the two proposed configurations in order to choose a winner.

A detailed preliminary design on the selected configuration will be conducted later in the WP3, "*High-fidelity design and optimization*".

Project management is parallel to the entire design process and it is included in

WP4, "*Management and Dissemination*".

The present document focuses on WP2, and particularly on task 2.1, "*Concurrent Conceptual Design*" of the UNIFIER19 project.

WP2 relies on vast and solid basis set up during WP1 and reported in the deliverable D1.1 "*The design framework for an NZE 19-seater – Complete Report*". A version of this document is open to the general public namely D1.2 "*The design framework for an NZE 19-seater*" [4]. The activities carried out inside WP1 include: a review of the state of the art technologies applicable to the scope of UNIFIER19, market studies for miniliner and microfeeder services, acoustic and chemical emissions analysis, aircraft cost and infrastructural cost analysis, particularly on battery charging infrastructures and hydrogen supply infrastructures.

The existence of an other independent project named MAHEPA (Modular Approach to Hybrid Electric Propulsion Architecture) is worth mentioning. The two projects have common partners and share similar objectives, this may allow UNIFIER19 to benefit from milestones reached by MAHEPA.

The MAHEPA project has already developed and flown two variants of a serial hybrid-electric powertrains. The first uses an Internal Combustion Engine (ICE) coupled with a generator to charge batteries and power electric motors. While the variant relies on fuel cells to generate power enabling zero-emission, quieter and more efficient aircraft.

Previous research works inside DAER (Department of AERospace science and technologies), particularly at the FMSlab (Flight Mechanics & Flight Systems Laboratory), led to development of two sizing tools, namely *Hyperion* and *Titan*, that are then expanded and used within the design phase of UNIFIER19 [7], [8].

### 1.3. Aim

The aim of this work is to identify the optimal aircraft configuration with respect to the performance metrics derived from WP1, and compliant with the design requirements, also defined in WP1.

The performance metrics are defined through two indices that will be used to assess the optimality of a configuration, but also to justify investments in future phases of the project. The former is the *Emission Index*, which captures the combination of CO<sub>2</sub> emissions, NO<sub>x</sub> emissions and acoustic emissions. The latter is the *Success Index*, which aggregates estimations on development, certification and production costs, maintenance complexity, and operating costs to ensure future commercially successful operations.

The design requirements come from market studies performed in WP1. These studies highlighted two possible market scenarios, pointing out the need of a modular propulsion system for the same airframe.

The requirements of these target missions are fully reported later in Section 6.1.1. Here, the main high-level operational design requirements are presented, since they contribute to define the target aircraft to which this work is aimed at.

The aircraft should exploit a modular hybrid-electric propulsion architecture, allowing the development of a single airframe capable of accommodating various

combinations of propellers, batteries and range-extending technologies each tailored for a specific service, and easily upgradable to further extend the commercial life.

It should have a reconfigurable cabin that allows to rapid switching between a passenger-seating cabin and a cargo cabin, enabling work in a multimodal passenger and freight network. The same aircraft moves people with daylight and freight during night-time.

A reduction in ground infrastructure investments exponentially increases the number of communities served by this aircraft. This makes the ability to operate on unpaved runways of rural airport of paramount importance. Moreover, the integration in the airframe of equipments, such as a facial recognition system, enables the authentication of pre-registered and security-approved travellers, allowing also an embarking and disembarking experience *"as easy as a bus"*.

Furthermore, the aircraft should operate silently to avoid the *"not in my backyard"* syndrome, specially during night operations, and it should employ an advanced fly-by-wire control system to reduce pilot workload in the envision of single-pilot operations and to facilitate future upgrades to autonomous or remotely-piloted flight.

It should be able to perform commercially successful operations in the near future. Near-zero emission CS-25 airliners are still beyond the technological horizon of today, but the technology level that is maturing in this years allows the development and certification of a CS-23 hybrid-electric aircraft, that is, an aircraft able to carry up to 19 passengers with a Maximum Take Off Mass (MTOM) up to 8618 kg.

## 1.4. Method

The approach adopted to select the candidate aircraft design solution delivered by POLIMI can be divided into four major steps:

**1. Design Space Sweep.** An in-depth research is conducted to identify all the innovative technologies that are applicable for this aircraft family, proceeding from work done in WP1. The identified technologies are initially combined with a systematic approach to obtain all possible combinations. This leads to a large number of alternatives, of which many are not feasible or not practical.

**2. Qualitative Selection.** A set of selection criteria are chosen and used to perform a reduction of the initial list of candidates. The list is further reduced during a series of brain-storming in which the potential of each configuration is discussed. Some other configurations are added, as other secondary technologies are taken into account from discussions and from solutions of issues highlighted by conceptual hand-sketches. In the end, a subset of 15 candidate aircraft is used as input of an accurate selection based on the AHP (Analytical Hierarchy Process), obtaining the 5 most promising configurations.



**3. Quantitative Selection.** The five selected aircraft are sized by taking advantage of the sizing tools developed internally at DAER, i.e. *Hyperion* and *Titan*. This involves determining the necessary input data based on mission and certification requirements and updating the software to consider the new particular mission and the new technologies specific to these aircraft. The sizing results are iteratively assessed and discussed, bringing to the update of some design requirements. Finally, the ultimate sizing results for the various configurations are compared and the best one is identified and delivered for further assessment.

## 1.5. Structure of the Work

The following paragraphs contain a brief description of each chapter to help the reader moving through the document.

**1. Introduction.** The document starts describing what the world is demanding to air transportation in these years and how the aviation industry is going to answer in the near future, this is crucial to understand the role UNIFIER19 is going to play.

Then follows a summary of the work already performed by the team, and a description of what is taken ahead within this thesis.

**2. Design Space and Technology Review.** One of the key target to pursue in the early stages of conceptual design of an innovative aircraft is certainly to explore the widest range of design alternatives suitable for the intended aircraft. This starts with being aware of all technological opportunities with the allowed TRL (Technological Readiness Level).

In this chapter many of these technologies are presented and discussed with the available literature material.

**3. Candidate Configurations.** The entire design space is explored, considering every possible combination of aero-propulsion systems, hybrid-electric architectures and aircraft layouts. This process ends with a list of possible candidate configurations.

**4. Qualitative Selection.** In this chapter the list of candidate configurations is reduced applying qualitative selection criteria. Initially a raw selection is performed to reach a practical number of configurations but paying attention not to miss any precious solutions. Then, a final and accurate selection is performed on the shortened list using the AHP.

At the end of this chapter, five candidate configurations are ready to be sized, analyzed and further selected using quantitative selection criteria.

**5. Sizing Methodology.** This chapter starts with an overview of the sizing tools developed inside the *Department of Aerospace Science and Technology of Politecnico di Milano*, namely *HYPERION* (HYbrid PERFORMANCE simulatION) *ARGOS* (AiRcraft GeOmetric Sizing) and *TITAN*.

The candidate configurations that have been selected take advantage of many innovative technologies that were still not included in Titan. In order to obtain detailed solutions it has been necessary to model and include them in the sizing tools, this process is summarized as well.

Particularly, an analytical model of a strut braced wing is developed in order to catch the main effects on weight and drag. The strut braced wing takes the place of truss braced wing, because at this level of detail it is considered enough to predict major effects while allowing to neglect many design details that are still unknown at a conceptual level.

**6. Quantitative Selection.** Initially, an explanation of methods and criteria used to estimate the input parameters required to size the candidate configurations are shown.

Then, the sizing results are presented, compared and discussed to select the configuration that is delivered to the partners for assessment.

**7. Conclusion.** Here, the main results are summarized and conclusions and recommendations are drawn.

**A. Strut Braced Wing Analytical Modeling.** As mentioned above, the aircraft sizing tools needed to be updated with the capability to model the new technologies adopted by the candidate configurations.

One of such technologies, which required an original development is the strut braced wing presented in Chapter 5, which is thoroughly detailed in this Appendix.

## 2. Design Space and Technology Review

The chapter starts with a general overview on the present state of the art that can be of interest for the UNIFIER19 project. Subsequently, an extensive set of innovative technologies are presented with more details because they are actually applied to the candidate configurations.

### 2.1. Overview

In 2008 NASA has awarded 18-month research contracts to six industry teams [9] to study advanced concepts for subsonic and supersonic aircraft that could enter in service around 2035. The focus of these studies is on commercial transports that can overcome major performance and environmental challenges for the benefit of all the Earth's population. The research and development airplane generation is known as "N+3", denoting three generations beyond the one used for commercial transport fleet in 2008. These studies [10] led to predictions on noise and chemical emission reduction, to analysis of market demand for air mobility and to the exploration of various innovative aircraft configurations such as the Blended Wing Body (BWB) adopted in the NASA TeDP (Turbo-electric Distributed Propulsion, also known as N3-X) shown in Figure 2.1.

A concept aircraft explored by Boeing during N+3 researches is the SUGAR (Subsonic Ultra Green Aircraft Research) [12]. This project evolved in three variants: SUGAR *High* is the initial one, featuring a high aspect ratio Truss Braced Wing (TBW), SUGAR *Volt* is the hybrid-electric successor of High and, with the variant *Freeze*, they exploited BLI (Boundary Layer Ingestion) and switched to fuel cells fed with liquified natural gas.

A review of the propulsion technologies proposed for the N+3 subsonic vehicles is given in [13]. They computed the relative weights of each propulsion technology with respect to the N+3 goals (i.e. reduction of acoustic and chemical emissions), highlighting the importance of electric motors (1<sup>st</sup> place with a weight of 13.8), advanced combustors (2<sup>nd</sup> place with a weight of 11.2), alternative fuels (3<sup>rd</sup> place with a weight of 10.8), boundary layer ingestion (4<sup>th</sup> place with a weight of 10.2), composite materials (5<sup>th</sup> place with a weight of 10) and distributed electric propulsion (6<sup>th</sup> place with a weight of 9.8).

They also estimated the benefit each technology has in attaining the N+3 goals and the likeliness of them being ready for implementation in the 2035. Technologies such as Fuel Cells (FC), electric motors and batteries have high benefit on the goals, others such as composites and Boundary Layer Ingestion (BLI) have high probability of being ready on time. In particular, the Distributed Electric Propulsion (DEP) is considered both beneficial and likely.

In 2009 IATA (International Air Transport Association) published a report [14]



Figure 2.1: NASA N3-X, of interest the adoption of a BWB layout with DEP on the back to exploit also BLI [11].



Figure 2.2: Boeing SUGAR Freeze, evident the presence of BLI and TBW technologies [11].





Figure 2.3: Airbus ZEROe concept aircraft family (above) and the new "Pod" configuration (below) [15].

with the aim to show a possible timeline of future technological innovations, their effect in reducing emissions from the global aircraft fleet and the likelihood of their implementation. They predicted a 50 % reduction of aviation CO<sub>2</sub> emissions by the year 2050 relative to 2005. They found that fuel efficiency improvements of about 25-30 % can be reached by applying combinations of evolutionary technologies, however, further improvements with the conventional T&W (Tube and Wing) layout will become hardly attainable around 2035. Thus, radically new geometry of the aircraft, such as the BWB, combined with innovative propulsion systems will be required to further reduce emissions towards 2050.

Since the publication of these studies (around 2010), interest for fuel cells and hydrogen propulsion has sharply increased as it proved greater potential and faster technological advance. In addition to transport, hydrogen is expected to be a widespread clean energy carrier in many other industries, and aviation is taking the most from this trend.

Airbus, with the ZEROe concept aircraft shown in Figure 2.3, has the ambition to develop the first zero-emission commercial aircraft by 2035. All three ZEROe concepts use modified gas turbines able to operate with liquid hydrogen. Hydrogen fuel cells create electrical power that complements the gas turbine, resulting in a highly efficient hybrid-electric propulsion system. They also started considering a variant (Figure 2.3) with a distributed hydrogen fuel cell propulsion system arranged

inside 6 pods along the wing, each pod is a stand-alone propulsion unit consisting of propeller, electric motor, fuel cell, hydrogen tank and all the required equipment.

According to [16] the most promising innovations for aircraft designed to enter in service before 2035 are: more efficient engines (high bypass ratio, high pressure), composite structures, electric taxiing, winglets, riblets, variable camber, spiroidal wing tip, hybrid/natural laminar flow control and hybrid-electric propulsion.

Recently some concrete success in green aviation have been accomplished. For example in June 2020, Pipistrel certified the first electric aircraft, a LSA (Light Sport Aircraft) called *Velis Electro* that is able to fly for up to 50 minutes [17]. The biggest electric aircraft that has flown so far is the *eCaravan* from AeroTEC & magniX [18]. It flew for the first time in May 2020, it can host up to 9 passengers, and it is able to fly up to 160 km with 5 passengers on board.

## 2.2. Multi-Criteria Decision-Making

In conceptual design many important decisions have to be made, requirements must be fulfilled and choices must be balanced among multiple criteria. These decisions impact the outcome of the project but it is seldom possible to calculate a parameter that provides a mathematical net distinction among the alternatives. In fact, the available information at the early phase of every project are usually based on subjective perceptions and speculations. In addition, requirements and selection criteria may be conflicting with each other making impossible to identify a solution without a clear systematic approach.

A variety of Multi-Criteria Decision Making (MCDM) methods have been proposed in literature to make the selection process more formal, credible and transparent.

These methods embrace several different approaches and various mathematical models to assist deciding the best alternative(s). In [19] some of these methods are described and compared to identify possible differences in the methods, and to give recommendations for their use. The methods they compared showed parallel results but in certain cases the choice of a MCDM method can have significant effect on the result. They concluded with the following guidelines for the designer to obtain and interpret the comparison results:

1. Start concept comparison with simpler methods such as Pugh matrix.
2. Consider using another method to verify the results.
3. When the result is very clear with one method, it most likely will be same with other methods.
4. When the results show small differences among alternatives, one should try with another method, or further study the alternatives, or enhance the resolution of ratings, or change the comparison mode.
5. Look into the actual comparison data, and check the possible best alternative in detail before making the final decision.

Criteria	Weight	Alternatives			
		A	B	C	D
Criteria 1	2	S	+	+	-
Criteria 2	1	S	-	+	-
Criteria 3	3	S	+	-	+
Criteria 4	2	S	+	+	+
Criteria 5	4	S	-	-	-
Criteria 6	3	S	+	+	-
Criteria 7	5	S	+	+	+
Criteria 8	3	S	+	-	-
<b>Total +</b>		0	6	5	3
<b>Total -</b>		0	2	3	5
<b>Score</b>		0	4	2	-2
<b>Weighted +</b>		0	18	13	10
<b>Weighted -</b>		0	5	10	13
<b>Weighted Score</b>		0	13	3	-3

Table 2.1: A simple example of implementation of the Pugh's matrix.

One of the most popular examples of MCDM method is the Pugh's Method described in [20]. It is very simple to use because it relies on a series of pairwise comparisons between design candidates against a number of criteria. One of its key advantages is its ability to handle a large number of decision criteria and a large number of alternatives. An example of usage of Pugh's method is given in Table 2.1.

The process to construct the Pugh's matrix can be divided into five steps:

1. *Identify and clearly define the selection criteria.* The selection of proper criteria have a major impact on the robustness and reliability of the outcome. Weights can be assigned to criteria, but it is recommended to include them after a first neutral comparison.
2. *Select a baseline candidate design option.* Its performance with respect to all criteria are set to "S" (Same) by definition.
3. *Compare each candidate design option with the baseline.* The score is decided for each criterion with a pairwise comparison: "S" if the two options have the same performance with respect to that criterion, "+" if the candidate is better than the baseline, "-" if it is worse.
4. *Compute total scores and weighted scores.* The number of "+" and "-" are calculated, their difference is the score. In case of non-unitary weights, each vote has to be multiplied by the corresponding criterion weight.
5. *Make the decision.* Ideally, the highest ranked score is the winner, but the use of common sense is recommended.

Another widely-used MCDM method is the Analytical Hierarchy Process (AHP) presented in [21]. It is much more detailed and laborious with respect to Pugh's

method but it delivers more tangible and robust results. The method is extensively described in Chapter 4 as it is implemented in a spreadsheets tool to perform the accurate qualitative selection of the candidate configurations.

## 2.3. Aircraft Layout

The typical tube-and-wing (T&W) layout with aft-tail has been established itself since many years both in general aviation and on commercial airplanes. However, many other geometries are possible and it is good practice to consider all of them at early stages of the design. In fact an unusual configuration may unexpectedly bring together many desirable features for a certain mission with only some acceptable downside. In [22] many alternatives are discussed, including: asymmetric airplanes, tandem wing, oblique wing, C-wing, multi-fuselage, and others.

Other alternatives come out when considering atypical tail options such as, the canard, the Three Surface Aircraft (TSA) adopted on the Piaggio P180 Avanti or the tailless (also proposed as N+3 aircraft [23]).

In this section a brief overview is given for the most special aircraft layout taken into account for this project.

### 2.3.1. Blended Wing Body

The BWB is a hybrid shape that resembles a flying wing with some features from conventional commercial aircraft (see figures 2.1 and 2.3). Its shape allows unique interior designs through wide payload areas in the center of the vehicle. The main advantage of this layout is to reduce the wetted area, the airfoil-shaped body contributes to generate lift enabling a reduction in size and drag of the wings. It does not suffer from the drag penalty associated to wing-body junctions and it permits efficient structures with reduced weight thanks to the thickness of the wing root section. Other advantages are the ability to use the wingtips as vertical fins and the lower optimal wing loading.

In [24] a comparison with a conventional T&W layout has been done, highlighting a lower operating empty weight and lower fuel burn per passenger kilometer with values as high as 30% for a long-haul 250-PAX plane. Articles from NASA and Airbus mention a reduction in fuel consumption of about 20%. In [25] a new concept for the pressurized cabin of a BWB is described, that also has good customer acceptance due to the flexibility in cabin configuration.

The BWB aircraft is a configuration of particular interest since many years, as it promises outstanding efficiency improvements. In fact both NASA and Airbus built and flew a demonstrator, the *X-48* [26] and the *Maveric* [27] respectively. Furthermore, the N+3 proposal of NASA called N3-X adopted the BWB layout, and a BWB is included in the ZEROe concept family of Airbus.



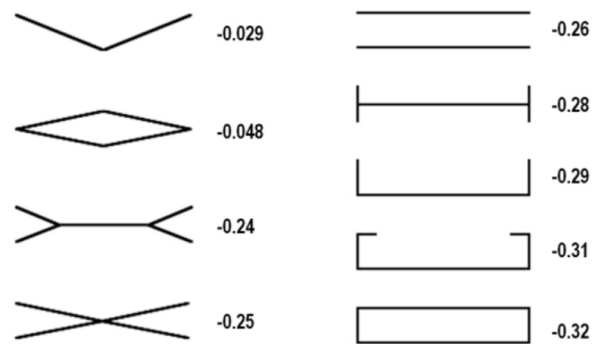


Figure 2.4: Induced flow factor for various wing configurations [29].

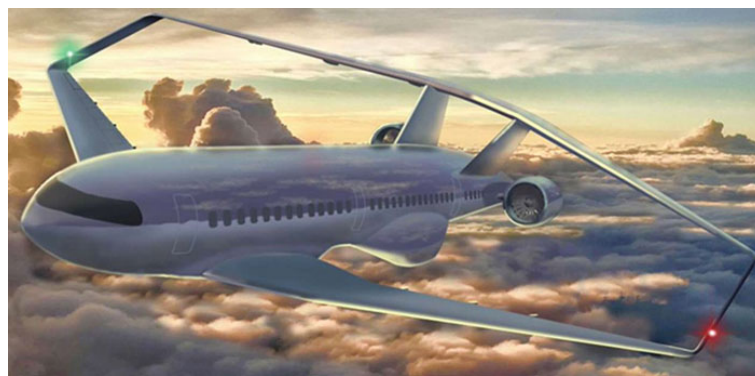


Figure 2.5: PARSIFAL project [30].

### 2.3.2. Box Wing Aircraft

The BWA (Box Wing Aircraft) is the implementation of the best wing system theorized by Prandtl [28]. The main advantage is the minimization of the induced drag provided by the box wing. An overview of the features related to this aeroplane layout is given in [29]. Equation 2.1 express the induced drag as function of the induced drag factor  $\delta$ , which is usually greater or equal to 0 for planar wings.

$$C_{Di} = \frac{C_L^2}{\pi AR} (1 + \delta) \quad (2.1)$$

Figure 2.4 shows how changes of the wing geometry in the vertical direction have an effect in reducing the induced drag factor. In fact, it becomes already negative by adding a small dihedral or by changing the shape of wing tips, but the biggest improvement is met with the box wing that leads to a drag reduction of more than 30%.

Some benefits other than fuel saving are: better pitch control, reduced vortex formation, ground-operation advantages, reduced noise and enhanced control strategies allowed by the distribution of control surfaces across both wings

The PARSIFAL project (Prandtl ARchitecture for the Sustainable Improvement of Future AirpLanes), shown in Figure 2.5, has been concluded in 2020 and had the objective to establish the scientific and engineering basis necessary for introducing this innovative aircraft into service [30].

A similar concept is the Joined Wing Aircraft (JWA), used by the Guizhou Soar Dragon, a Chinese HALE UAV (High Altitude Long Endurance Unmanned Aerial Ve-

hicle). The JWA is considered to have less structural complexity while preserving most of the aerodynamic advantages of the box wing.

Another resembling technology with great potential is the Spiroidal wing tip [31], in which the wing closes on itself at the tip, enhancing efficiency by reducing vortex intensity.

### 2.3.3. Truss Braced Wing

The TBW layout leverages the reduction of induced drag associated with a high-aspect ratio wing by means of support braces that enable a reduction of structural weight, and a further enhancement of aerodynamic efficiency through a reduction of the thickness-to-chord ratio of the wing. The main drawbacks are the increase in parasite drag and weight that come with the supporting structure.

This wing has been selected for the SUGAR High variant (Figure 2.2) proposed as N+3 airplane [12], they achieved a 39% reduction in fuel burn compared to the SUGAR Free baseline, and 22 db less noise. They identified opportunities for wing weight reduction and aerodynamic improvements able to take the fuel burn benefit to 58%. Their conventional configuration, Refined SUGAR, indicated a 44% reduction in fuel burn while noise decreased by 16 db.

In [32], a MDO framework for conceptual design of truss-braced wing configurations was developed. In addition, fuel saving potentials attained with different truss designs of gradually increased complexity (cantilever, strut braced, truss braced with 1 jury, and with 2 jury) were presented and compared. The results showed larger benefit for increased complexity in truss topology, in fact, compared with the cantilever wing, the 2 jury TBW provided up to 20% of fuel saving and 11% reduction in MTOM. However, parameters such as fuel mass, wing area, MTOM and lift-to-drag ratio present a clear knee on improvements at single jury TBW and the mass of the wing assembly even increases slightly passing to the 2 jury topology.

The conceptual design of a 72-PAX regional jet aircraft is the topic of [33]. They started from an existing 52-passenger conventional turboprop airplane, then they included high-bypass ratio turbofans and modified the fuselage to accommodate 20 more seats. Finally, they adopted a strut braced wing with an aspect ratio of 20. The strut led to a 20% reduction in wing weight with respect to an equivalent cantilever wing, but it caused a 36% increment in wing assembly weight with respect to the baseline. However, the fuel weight showed a considerable 9.7% reduction thanks to the increased lift-to-drag ratio.

## 2.4. Aircraft Propulsion

Electric propulsion is the most sustainable technology available today, in fact it has no local chemical emissions at all, and it is way more quiet and way more efficient than an Internal Combustion Engine (ICE). Moreover, motors and controllers are smaller, lighter, safer, more reliable, reversible (usable as generators), they have longer TBO (Time Between Overhaul), they have constant power with altitude and almost flat torque-speed curve that ease their use for flight control, and they enhance aircraft flexibility as many of them can be easily placed far away from one or more diverse power supplies. The downsides of electric propulsion come out

when considering energy storage systems: batteries are much heavier than fuel, and they're not burned off during flight, so the corresponding range benefit is lost.

Based on the current trends of development, the adoption of electric propulsion promises to unfold a good potential in terms of local environmental impact. It is therefore interesting to exploit all its advantages in order to overcome the downsides and design a commercially competitive airplane.

Many technologies leverage electric powertrains, this section presents the most relevant to this project.

Hybrid-electric architectures allow smoothly switching among different power sources, typically between batteries and a Power Generation System (PGS) such as ICE or Fuel Cells (FC). Multiple architectures exist, each of them enabling a variety of energy-management strategies, to make an example: taxiing, take off and climb can be silently performed draining power from batteries, thus postponing ICE ignition at altitude.

### 2.4.1. Hydrogen

Hydrogen is a highly attractive option for the future of aviation. A vast fact-based study of hydrogen technology for aviation is presented in [1].

Hydrogen does not contain carbon, so its reaction with air does not cause CO<sub>2</sub> emissions on flight and, with fuel cell, it does not give rise to NO<sub>x</sub> either. In addition, studies on hydrogen-combustion aircraft showed that emissions of NO<sub>x</sub> can be reduced by 50-80% without large losses of engine efficiency.

Hydrogen produces about 2.5 times more water vapor than kerosene, however the water molecules coming from hydrogen-combustion have a lower global warming effect, resulting in a 30-50% reduction in impacts from contrail and cirrus formation. In addition, the water vapor emitted by a fuel cell is cooler and it can be conditioned on-board to impact less on the local atmosphere.

For these reasons, airplanes based on fuel cell can reduce climate impact up to about 75-90%, while hydrogen-combustion is the next best alternative with 50-75% reduction.

It is important to underline that the study cited above forecasts these values based on preliminary evaluations.

The fuel cell technology is considered suitable for short and medium-haul aircraft, while for long-range airplanes, hydrogen-powered turbines will likely remain the only option in the foreseeable future.

There exist multiple types of fuel cells, the Proton Exchange Membrane (PEM) is considered the most mature and suitable for aviation to date.

The main drawback of hydrogen are its significantly low-temperature critical point (about -240 °C) and its very low density (71 kg/m<sup>3</sup> non-pressurized liquid cryogenic, versus 780 kg/m<sup>3</sup> of kerosene). On the other hand, hydrogen has three times the heating value of kerosene (120 MJ/kg against 43 MJ/kg).

Hydrogen can be stored as highly-pressurized gas (usually at 70 MPa) or in liquid cryogenic form (at about -255 °C). Gaseous hydrogen storage (GH2) is already commercially available but it is mostly suitable for short flight due the size and weight of pressurized cylinders.

Liquid hydrogen storage (LH2) tanks are significantly lighter than GH2 tanks and they require about half of their volume, however they are still about 4 times as big compared to kerosene tanks. LH2 tanks are integrated into the aircraft fuselage

as they are spherical or cylindrical to minimize heat transfer and thus, vaporization and losses.

The gravimetric index  $GI$  is commonly used to quantify the efficiency of a hydrogen storage system, it is defined as the ratio between the hydrogen mass  $m_{H_2}$  and the total mass of the completely filled tank  $m_{\text{tank}} + m_{H_2}$ :

$$GI = \frac{m_{H_2}}{m_{\text{tank}} + m_{H_2}} \quad (2.2)$$

The gravimetric index is estimated to be about 20% as today, but major improvements are expected in the near future bringing it over 35% (some studies estimates values as high as 70%, see [34]).

In parallel, significantly hard challenges also await for infrastructure and logistics, since ways and networks are necessary to properly feed airports with the required amount of hydrogen.

Research work has been already conducted on these topics at Politecnico di Milano to obtain a sizing procedure for fuel cells, GH2 and LH2 tanks [35], [7].

#### 2.4.2. High-lift Propellers

High-lift Propellers, or blown wing, or also Leading Edge Asynchronous Propellers Technology (LEAPTech) is a promising technology that exploits aero-propulsive interaction to enhance overall aircraft efficiency [36]. It features a number of tractor propellers spaced spanwise along the leading edge of the wing. These propellers are activated as needed during flight to increase the maximum lift coefficient by providing substantially increased dynamic pressure over the wing, thus enabling the design of air vehicles with lower stall speeds and/or lower wing area without the need for complex high-lift devices. This allows for a smaller wing, sized close to the theoretical area for maximum cruise range, instead of the usual sizing to meet take off and landing requirements, therefore attaining a substantial reduction in cruise drag and wing mass without decreasing take off and landing performance. In addition, this can go along with an increase of aspect ratio to comply with wing span constraint, bringing further aerodynamic benefits. Other remarkable advantages could be noise reduction and enhanced reliability.

NASA, with its X-57 shown in Figure 2.6, spent and is spending much research effort on this innovative aircraft [37]. They already tested the wing on-ground, now they modified a Tecnam P2006T with an electric propulsion system that is about to go through flight testing. Subsequently, they will include and flight test the new blown wing, with 14 tractor propellers distributed along its span.

Traditional propulsive units make it impractical or impossible to apply such a configuration, but electric motors turn it attractive with their smaller sizes, lower weight, and their ability to scale with minor losses of efficiency and specific power.

A previous work in Politecnico di Milano [38] focused on establishing and implementing a procedure for the performance-based conceptual sizing of an electric aircraft featuring this technology.



Figure 2.6: NASA X-57 featuring a blown wing and WTP [37].

### 2.4.3. Wing Tip Propellers

A wing tip propeller reduces wing induced drag by attenuating the wing tip vortex by means of the propeller slipstream. In addition, it can also improve propulsive efficiency of pusher propellers.

In [39] the propeller has been analyzed in a pusher configuration such that it is immersed in the wing tip vortex. They estimated a reduction of approximately 25% in power required to maintain cruise. In addition, this is followed by a 30% decrease in induced drag (at a lift coefficient of 0.35) due to the vortex dissipation resulting from aero-propulsive interaction, this is equivalent to about 10-12% reduction of total aircraft drag.

In [40] the propeller has been analyzed in a tractor configuration and compared with a conventional in-board configuration. They measured an increase in lift 1-4% smaller for the wing tip mounting with respect to the in-board mounting, but the dynamic pressure boost in the latter case acts on a double spanwise length, and on a region of the wing where the section lift is higher.

The drag is reduced by 5-15% compared to the conventional configuration, at a lift coefficient of 0.5 and thrust coefficient in range 0.09-0.13, and it further improves with increasing lift coefficient and thrust coefficient, reaching 25-50% reduction (at a lift coefficient of 0.7 and thrust coefficient in range 0.14-0.17). The difference mainly comes from a reduction of induced drag, and it is equivalent to an increase of span efficiency up to 40% compared to the conventional configuration.

This technology is indeed quite old, it was already adopted by the *Vought V-173 "Flying Pancake"* (shown in Figure 2.7) which made its maiden flight in 1942. It boasted high maneuverability, impressive low-speed capabilities and great structural strength. The main problem was the amount of vibration produced by the complicated gearbox required to convey power from the engines through the long propeller shafts.

The NASA X-57 and the Eviation Alice are two modern examples of electric aircraft concepts that take advantage of WTP.



Figure 2.7: Vought V-173 "Flying Pancake", a first application of the WTP.

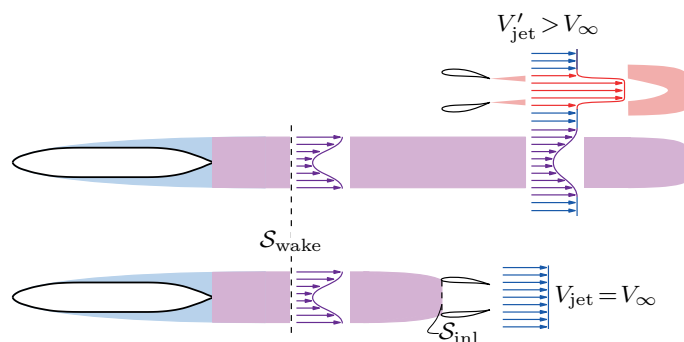


Figure 2.8: Comparison between simplified non-BLI (above) and ideal BLI (below) configuration [42].

#### 2.4.4. Boundary Layer Ingestion

This technology, known as wake ingestion or Boundary Layer Ingestion (BLI), is based upon the fact that the propulsive efficiency is enhanced when the propulsive unit is allowed to process part or all of the wake of the aircraft [41].

The most beneficial phenomena exploited are the reduction of jet mixing losses due to decreased jet kinetic energy enabled by the reduced inflow velocity at the propulsor, and the reduction of airframe mixing losses [42].

Figure 2.8 helps to understand the key concept behind BLI. In the non-BLI configuration (above), energy is dissipated both in the wake of the aircraft and in the jet of the propulsor because their speeds differ from the free stream value. In the ideal BLI configuration, all the wake of the aircraft is ingested by the propulsor which re-energizes it up to the free stream condition, thus maximizing propulsive efficiency.

In [41] the propulsion benefit of this technology is quantified with a formulation that can be directly used for propellers, however the conclusions also apply to ducted fans. The Author of the study defined a power saving coefficient  $PSC$  as:

$$PSC = \frac{P'_P - P_P}{V_0 D / \eta'_P} \quad (2.3)$$



where  $P'_p$  is the non-BLI propulsive power,  $P_p$  is BLI propulsive power,  $V_0$  is the free stream velocity,  $D$  is drag, and  $\eta'_p$  is the non-BLI propulsive efficiency.

Then it is shown how the  $PSC$  is greater for higher disk loading (smaller propeller), when the wake form factor is high (flow close to separation), and when the propeller is designed to flatten down the outflow wake profile (wake recovery). In addition, it is shown that the benefit can reach 20% in some cases.

In [42] they present a quantitative estimation of the BLI benefit through a control volume and one-dimensional analysis. This method is usually referred to as "Power Method". They applied the method to the D8 aircraft and showed a power reduction of 8.7% obtained with the ingestion of 40% of the fuselage wake (the upper part).

A complete review of many other BLI modelling approaches is performed in [43], where some results are also presented.

In [44] they analyzed a propulsor located at the upper rear centerbody of a BWB aircraft, using a parallel compressor model to take into account the effect of a non-uniform inflow, and retrieving the required boundary layer data from a common 2D subsonic airfoil analysis tool (XFOIL). They obtained a  $PSC$  of 2.44% at cruise, that raises to 5.4% when the drag reduction due to embedded engines is taken into account. They also indicated a variation of about 3% in fan efficiency between distorted and undistorted inflow sector.

Many modern aircraft concepts adopt this technology, some examples are the NASA N3-X, the Aurora D8 "Double Bubble", the STARC-ABL (Single-aisle Turbo-electric Aircraft with Aft Boundary-Layer Propulsion), the EADS VoltAir, the SUGAR Freeze or the Airbus ZEROe BWB.

### 2.4.5. Distributed Electric Propulsion

The main objective of the Distributed Electric Propulsion (DEP) technology is to exploit at best the benefits of the synergic coupling among structure, aerodynamics and propulsion enabled by the integration of multiple propulsive units throughout the airframe [45]. Thereby, aerodynamic, propulsive, structural, and/or other efficiencies are mutually maximized to enhance the overall vehicle performance.

Electric propulsion enhance potential of technologies such as the blown wing, and it permits to leverage multiple aero-propulsive interactions at a time. As an example, based on the technologies presented in this section, the following possible benefits may be simultaneously obtained:

- Increased lift by means of circulation control (LEAPTech),
- Reduced drag through separation control (HLFC),
- Reduction of viscous drag with reenergization of the wake (BLI),
- Reduction of drag thanks to vortex attenuation (WTP),
- Vehicle control without control surfaces via differential thrust and thrust vectoring, for both pitch, roll, and yaw (PCA),
- Reduction of noise through spectrum control or signature alteration, attainable thanks to the plurality of thrust/noise sources,
- Reduction of noise and installation weight given by the better integration of the propulsion system with the airframe,

- Increased safety, reliability and robustness because of redundancy,
- Lower production and maintenance costs thanks to higher production rates and easier replacement of propulsive units that are smaller and lighter.

## 2.5. Other Potentially Useful Technologies

This section mentions a few more relevant technologies, some others have been considered during the initial phase but they are included here because in the end they did not play a role.

### 2.5.1. Propulsion Control

In the past many aircraft experienced major flight control system failures, and the crew tried to use the propulsion for emergency flight control, unfortunately most of the time without success. The advent of flight control computer prompted NASA to develop a system, called Propulsion-Controlled Aircraft (PCA), that uses pilot inputs and sensors to provide proper engine thrust commands for emergency flight control [46], [47]. The concept was successfully tested on various aircraft such as the F-15, MD-11, B-747 and many others.

This proved the possibility to control an aircraft using only propulsion, despite the slow time response of typical aircraft engines. A hybrid-electric propulsion system, possibly with distributed propulsion, would exploit definitely better this technology giving the opportunity to get rid of vertical tail plane and control surfaces improving aerodynamics by means of a smaller wetted area and lower induced drag.

### 2.5.2. Laminar Flow

The reduction of parasite drag by attaining a great fraction of laminar boundary layer has been the dream of several generations of aircraft designers. The techniques for the design of airfoils capable of maintaining Natural Laminar Flow (NLF) over a large portion of the chord are established [48], as well as for the design of the fuselage [49]. The main obstacles are the high speeds, the sweep angle, and the accumulation of dirt on the surfaces. A practical limit on the maximum length of NLF runs is of about 50-70% of the total length of a surface, yielding a drag reduction of about 30-60%. The potential drag benefit for a high-performance business jet with NLF is up to about 24%.

Riblets are surface striations that are aligned with the airstream [50]. Their purpose is to thicken the near-wall viscous region providing a "slip layer" at surface that is able to reduce drag up to about 8% with a yaw angle up to 15 degrees (at 30 degrees the benefit is lost). They can be used in combination with NLF to reduce friction drag also in the turbulent part of the flow.



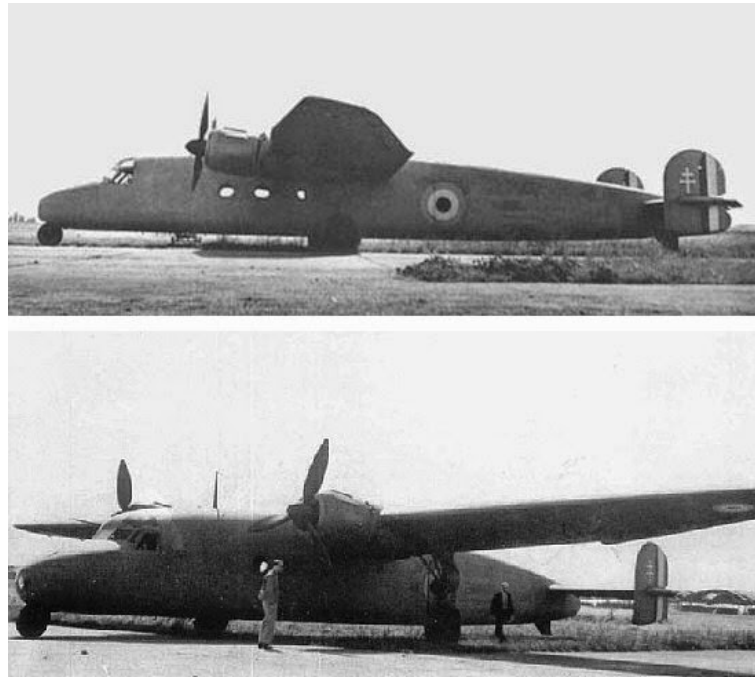


Figure 2.9: Blohm & Voss BV 144 that adopted the VIW, of interest the easy boarding thanks to the fuselage closer to ground, and the absence of tail up sweep angle.

### 2.5.3. Morphing

Today's aeroplanes are approaching peak levels of efficiency, making further improvements difficult, without new game-changing technologies. Wing design is a compromise between several constraints on various flight conditions, and its best efficiency is achieved rarely in the flight envelope. This is particularly true for short-haul aircraft, as they spend much of the flight climbing and descending, and only brief period flying at a constant level cruising altitude. A way of enhancing aircraft efficiency is to adapt the shape of the wing in-flight to maximize its performance under all operating conditions. Many researches have been done on this subject in the past (e.g. with the F-111 "*Mission Adapting Wing*") and many are still on-going (e.g. see Clean Sky website [51]).

**Variable Incidence Wing (VIW).** The VIW has been adopted on the Vought F-8 Crusader, a jet aircraft introduced in 1957 that served principally in the Vietnam war. The VIW made possible to change angle of attack without altering the fuselage pitch angle during deck landing, increasing forward visibility and allowing operations on shorter Essex class aircraft carrier of World War II, that were designed for old propeller aircraft.

Another application of VIW was on the Blohm & Voss BV 144 shown in Figure 2.9, a twin-engined commercial airliner developed in Germany during World War II but intended for post-war service. It had a crew of three and was able to carry 18 to 23 passengers. The VIW eases boarding operations by allowing the fuselage to sit low to the ground, and ensures the comfort of the passengers by reducing fuselage pitch during takeoff and landing.

In addition, the VIW avoids the upsweep angle enabling lower fuselage drag,

and it makes possible to further augment efficiency during all flight phases by optimizing fuselage pitch independently of the required angle of attack. This technology can be coupled profitably with high-lift propellers (blown wing) to potentially improve landing performance, and it can simplify the shape of a fuselage that minimizes drag by maintaining NLF on a vast portion of its surface.

**Active Aeroelastic Wing (AAW).** The AAW can be considered a return to an idea first pioneered by the Wright Brothers. It is a multidisciplinary technology as it integrates aerodynamics, active controls and structural aeroelastic behavior [52]. The shape of the wing is aeroelastically deformed through multiple leading and trailing edge control surfaces driven by a flight control system. The energy of the airstream is exploited to twist the wing with very small control surface deflections, so that the control forces are produced by the wing itself. This enables the use of thin, high aspect ratio wings with benefits in terms of reduced aerodynamic drag and reduced aircraft structural weight. The technology has already been proved in full scale using the X-53 aircraft.

**Adaptive Compliant Trailing Edge (ACTE).** The U.S Air Force and NASA performed a successful flight test campaign on a business jet retrofitted with ACTE control surfaces [53]. The high-lift devices of the test aircraft have been replaced with seamless variable-geometry control surfaces. A series of acoustic flight tests have also been carried out, reporting a reduction in aircraft noise up to 30% on takeoff and landing. Another benefit is an increase in lift-to-drag ratio, whereas the main drawback is the lower maximum lift coefficient due to the absence of slots to re-energize the boundary layer.

## 2.6. Similar Works

The demand for a greener aviation, together with the wide European funding effort resulted in the foundation of multiple projects aimed at delivering a near-zero emissions 19-seat commuter aircraft based on new propulsion technologies.

The **ELICA** (ELeCtric Innovative Commuter Aircraft) and the **HECARRUS** (Hybrid Electric smAll commutER aiRcraft conteptUal deSign), similarly to UNIFIER19, are two projects funded by CleanSky within the research and innovation programme Horizon 2020 [54], [55].

The project **CoCoRe** (Cooperation for Commuter Research) is a study from DLR (Deutsches Zentrum für Luft- und Raumfahrt, also known as German Aerospace Center) [56] in collaboration with MTU Aero Engines [57]. They are developing a hybrid-electric aircraft based on Dornier Do 228 and Jetstream 31, which will be able to fly for a range of 200 km using electric power alone with 2 tonnes of batteries. The range can be extended to over 1000 kilometers by using two gas turbines.

Heart Aerospace claims that it will deliver the first **ES-19** fully electric 19-seater airliner certified for commercial flight by 2026 [58]. It has an operating range of 400 km and it can operate on runways 750 meters long, with 75% cost savings in fuel and 50% in maintenance.



Figure 2.10: Faradair BEHA [61].

The **HyFlyer II** project involves a partnership between ZeroAvia [59] and EMEC [60]. They have already flown a modified 6-seat Piper Malibu M350 powered by a hydrogen fuel cell powertrain and they planned a 350 mile flight with a 19-seat hydrogen-electric aircraft in 2023.

Faradair **BEHA** (Bio Electric Hybrid Aircraft) [61] is a multi-role hybrid-electric regional aircraft featuring a *triple box wing* and a contra-rotating pusher propfan (see Figure 2.10). It has a range of 1150 miles, it accommodates up to three LD3 containers, or 5 tons of payloads, or 18 passengers, and it is able to switch cabin configuration from passengers to cargo in only 15 minutes. Faradair aims to deliver 300 of this aircraft between year 2026 and 2030.

This page has been intentionally left blank.

## 3. Candidate Configurations

In a very first design stage one can rely on very limited landmarks to start. Only the target markets and the main operative requirements have been outlined so far. With them a research has been conducted to identify the technologies that promise the greatest potentiality of success to the project (see Chapter 2).

This chapter aims to rationally assemble the identified technologies in several ways, creating a vast cloud of different airplane configurations that evenly sweep the entire project space.

### 3.1. Design Space

The main high-level goal of UNIFIER19 project is to provide, in the near future, an air mobility service with greater flexibility, and substantially reduced emissions.

This objective can be reached by leveraging on the propulsive innovations that are maturing in these years. When appropriate, these innovations can be integrated with other systems capable of enhancing them, to further improve the performance of the final configuration. The most traditional options are also incorporated beside the innovative ones, and as a byproduct, this always ensures a benchmark to make unbiased assessments and selections.

The design space, in this sense, includes: the hybrid-electric drivetrains, with both thermal power generation system (THE) or fuel cells with gaseous (GH<sub>2</sub>) or cryogenic (LH<sub>2</sub>) hydrogen storage, various special solutions of the overall aircraft layout such as BWA or BWB, multiple options for the wing and tail, and much more.

A systematic approach enables facing the matter in a simplified but comprehensive way, ensuring access to all possible combinations. At this point, it is appropriate to bundle the array of considered options into categories, as in Table 3.1.

All the options mentioned above have already been depicted in Chapter 2. Many other technologies are excluded at this stage as they've been judged as not applicable to the project, mainly due to their technological immaturity; a few examples of them are: structural batteries, chemical hydrogen storage system and supercapacitors.

A few other technologies are introduced in 4, where some appealing alternatives arise during the qualitative selection, as a consequence of the further detailing and discussion of candidate configurations.

Category	Elements	
<b>Layout</b>	<ul style="list-style-type: none"> <li>• canard</li> <li>• tailless</li> </ul>	<ul style="list-style-type: none"> <li>• three surface (TSA)</li> <li>• traditional aft tail</li> </ul>
<b>Wing</b>	<ul style="list-style-type: none"> <li>• high aspect ratio supported wing (TBW, SBW)</li> <li>• box wing</li> <li>• cantilever</li> </ul>	
<b>Propulsion</b>	<ul style="list-style-type: none"> <li>• blown-wing (DEP)</li> <li>• traditional nose or wing-mounted</li> </ul>	<ul style="list-style-type: none"> <li>• tail cone (TCP)</li> <li>• wing tip (WTP)</li> </ul>
<b>Propeller</b>	<ul style="list-style-type: none"> <li>• contra-rotating</li> </ul>	<ul style="list-style-type: none"> <li>• single</li> <li>• tubed fan</li> </ul>
<b>Architecture</b>	<ul style="list-style-type: none"> <li>• single source (fuel or electric energy)</li> <li>• hybrid-electric (series or parallel or complex)</li> </ul>	
<b>Energy Source</b>	<ul style="list-style-type: none"> <li>• batteries</li> <li>• hydrogen fuel cells with GH2 or LH2 storage system</li> </ul>	<ul style="list-style-type: none"> <li>• fossil-fuel</li> </ul>
<b>Special</b>	<ul style="list-style-type: none"> <li>• flying-V</li> <li>• box wing or joined wing aircraft (BWA, JWA)</li> </ul>	<ul style="list-style-type: none"> <li>• blended wing body (BWB)</li> </ul>

Table 3.1: Categorized list of technologies options considered in the assembling of candidates.

---

## 3.2. Approach to Generation of Candidates

At the beginning, a systematic permutation of elements taken from all the different categories presented in Table 3.1 was attempted, but it revealed itself as a monumental undertaking. Ideally, each of the 4 elements of the *layout* category can be combined with each of those 4 in the *wing* category, then with the 4 of *propulsion*, next with all the 3 of *propeller*, with the 2 of *architecture*, still with the 3 possibilities of *energy source*. Finally there are at least 3 more *special* configurations. Moreover, it may be possible to pick up multiple elements of the same category, for example: one may include in the same aircraft both a tubed fan for a tail cone propeller and a single propeller for the blown-wing.

The number of individual configurations resulting from such a systematic procedure, is grossly estimated applying the classical algebra of permutations and combinations: proceeding on this path would lead to more than 200.000 aircraft configuration. Lately, there are studies concerning methodologies to include different layout options within a MDO by means of genetic algorithms, thus automatizing to some extent this process.

The amount of configurations is reduced by ignoring a couple of categories, as they can be applied to any aircraft. This is the case of *propeller* type, *architecture*, and *energy source*, that will be reintroduced in a later stage of the design.

Ideally one may consider a hybrid-electric architecture that relies on multiple source of energy (e.g. to extremes: both batteries, fuel and fuel cells, with both GH2 and LH2). Again such an increase in complexity has not yet demonstrated any merit, thus only simple hybrid architectures are included (i.e. PE, THE and fuel cells with GH2 and LH2).

The systematic approach is then boosted with a contextual selection based on removal of only those configuration unfeasible or unable to provide any benefit. In fact, many aircraft configurations obtained with a mere combination of options are wrong from definition (e.g. DEP with fuel as a single source of energy), others clearly destroy benefit each other (e.g. DEP with parallel thermal hybrid-electric architecture), and so forth.

In practice, a number of qualitative assessments are carried out, in which every alternative is discussed, relying on the help of hand-drawings to better define some particulars of less-intuible solutions. The generation of candidates, as well as their qualitative selection outlined in Chapter 4, is an iterative process in which a refined vision of the alternatives is earned every time they face an assessment or a selection.

## 3.3. Initial List of Candidates

The final result of the methodology presented in the previous section is the list of likely configurations reported in Table 3.2 (continued in Table 3.2). Each candidate configuration is numbered and described very briefly within the table, later in Chapter 4 a deeper insight is given for the selected alternatives. This big list of configurations is further reviewed in the next chapter, where an initial selection is performed concurrently with the end of this production of candidates. Many alternatives will be discarded as likely unfeasible, whereas a few will be added.

N°	Definition		
	Layout	Wing	Propulsion
1			Twin wing-mounted propellers
2			DEP and WTP
3		Cantilever	DEP, WTP and BLI
4			WTP and BLI
5			BLI and VIW
6	Aft Tail		DEP and WTP
7		TBW	DEP, WTP and BLI
8			WTP and BLI
9			BLI and VIW
10			DEP
11		Box Wing	DEP and BLI
12			BLI and VIW
13			DEP and WTP
14			DEP, WTP and BLI
15		Cantilever	WTP and BLI
16			BLI and VIW
17			DEP and WTP
18	Canard		DEP, WTP and BLI
19		TBW	WTP and BLI
20			BLI and VIW
21			
22		Box Wing	DEP and BLI
23			BLI and VIW

Table 3.2: Initial list of candidate configurations.



N°	Definition		
	Layout	Wing	Propulsion
24			DEP and WTP
25			DEP, WTP and BLI
26		Cantilever	WTP and BLI
27			BLI and VIW
28			DEP and WTP
29	Tailless	TBW	DEP, WTP and BLI
30			WTP and BLI
31			BLI and VIW
32			DEP
33		Box Wing	DEP and BLI
34			BLI and VIW
35			DEP and WTP
36			DEP, WTP and BLI
37		Cantilever	WTP and BLI
38			BLI and VIW
39			DEP and WTP
40	TSA	TBW	DEP, WTP and BLI
41			WTP and BLI
42			BLI and VIW
43			DEP
44		Box Wing	DEP and BLI
45			BLI and VIW

Table 3.2: Initial list of candidate configurations (continued).

This page has been intentionally left blank.

## 4. Qualitative Selection

The entire design space has been explored in Chapter 3 providing a formation of possible configurations presented in Table 3.2 (and continued in 3.2), a few other special configurations were mentioned in Table 3.1.

Certain other options are added or further detailed concurrently with the initial selection of 15 candidates, finally 5 of them are meticulously selected and described.

### 4.1. Initial Selection

The great deal of alternatives makes it challenging to define and assess them all with the proper deserved regard. Therefore a first coarse selection is used to narrow the list down to 15 elements, in such a way to ensure a minimal loss of opportunities in attaining the overall goal described in Chapter 1.

#### 4.1.1. Method

This first step of the qualitative selection has been carried out partially overlapping with the generation of candidate configurations of Chapter 3. In fact, a couple of special alternatives were born while further detailing the definition of each alternative (these are presented in the next section).

The rough down-selection method is based on the following evaluation criteria:

- A. One critical innovation at a time.** The embedding of multiple criticalities and challenges in a design impacts on the uncertainty of the estimated performances, and on the risk that the latter cannot be achieved. Such considerations rule out some apparently less promising alternatives, which instead would win in an ideal future selection, as greater knowledge on a particular technology may reveal lower capabilities than predicted. For this reason, the candidate configurations should share an equivalent level of complexity, uncertainty and feasibility.
- B. Keep all the innovative solutions.** Each attractive technology should be present at least in one of the down-selected configurations. At this step it is essential to not take away any innovative technology detected before, unless clear exceptional conditions are encountered to judge it absolutely inapplicable. In fact, the subsequent detailed assessment may change the game and promote an option over the others.
- C. Remove all impractical configurations.** All the selected configuration must be feasible, so they are carefully analyzed to detect possible inconsistencies



Figure 4.1: Otto Celera 500 L [62].

and oddities. For instance, the configurations including a variable incidence box wing have been considered impractical, as the structural complexity of such a mechanism would likely trivialize any advantages.

- D. Keep only solutions with proven benefits.** The high level of abstraction that naturally characterizes this generation and selection process may easily lead to assumptions that are not observed in practice, or to deviations toward different design goals. This coarse selection should maintain only those candidate configurations that show benefits only relative to the objective of this project, ignoring all those benefits that are not pertinent or not substantiated.

In practice, many reduced lists of candidate configurations have been proposed, they have been discussed and combined together until reaching a single list considered compliant with the selection criteria presented above.

#### 4.1.2. Further Candidates

As anticipated, in the course of the selection stage a few special candidate airplanes emerged, as they exploit a combination of new technologies that are able to contribute synergistically in the pursuit of the desired result.

The first one is inspired by the Otto Celera 500L, that features a bullet-shape fuselage with a pusher propeller, and that already completed a series of test flights and aerodynamic validations.

The Celera 500L, shown in Figure 4.1, is a six seats aircraft intended for private air transportation, it has a comfortable 1.88 m high cabin and a huge range of 8334 km. The design goal of 500L is the reduction of operating costs per passenger so to compete with commercial airline ticket pricing. This translates in extremely low drag over the entire aircraft and a very efficient propulsion system. Its astonishing fuel efficiency of 18-25 miles per gallon (compared to 2-3 mpg of an equivalent jet aircraft) is the result of extensive use of laminar shapes for the wings, fuselage, and tail sections.

Label	Definition		
	Layout	Wing	Propulsion
C1	Aft Tail	TBW	DEP and WTP
C2	Special Layout: Canard PCA with DEP, WTP and BLI		
C3	Special Layout: Canard with " <i>laminar flow fuselage</i> ", VIW and BLI		
C4	Special Layout: BWB with asymmetric BLI-DEP		
C5	Special Layout: BWA with DEP		
C6	Aft Tail	Cantilever	DEP, WTP and BLI
C7	Aft Tail	TBW	DEP, WTP and BLI
C8	Aft Tail	Box Wing	DEP
C9	Aft Tail	Box Wing	DEP and BLI
C10	Canard	Cantilever	DEP, WTP and BLI
C11	Tailless	Cantilever	DEP, WTP and BLI
C12	Tailless	TBW	DEP, WTP and BLI
C13	Tailless	Cantilever	WTP and BLI
C14	TSA	Cantilever	DEP, WTP and BLI
C15	TSA	TBW	DEP, WTP and BLI

Table 4.1: List of candidates at intermediate qualitative selection stage.

As already mentioned in Chapter 2, the tail cone propeller enables an enhancement of propulsive efficiency thanks to BLI, and the peculiar shape of the fuselage simplifies the achievement of wide percentage of laminar flow, as well as the reduction of shape drag typical of the tail cone upsweep angle, that thickens the wake as a result of vein fluid detachment. For simplicity and only as an identification label, it has been used the term "*laminar flow fuselage*" to recognize this concept later on, despite it does not comply to the letter with a physical interpretation.

Another appealing configuration provides for distribution of the propulsive system in such a way to enable flight control (PCA) without control surfaces. The distributed propulsion over wing span provides control about the yaw (and roll) axis, while the combination of a low-wing and a high tail propeller offers control on pitch axis. Such a solution further exploits the advantages of hybrid-electric modular propulsion by removing control surfaces, thus delivering increased aerodynamical efficiency and reduced trim drag contribution.

### 4.1.3. Results

The results of the selection procedure described above are the 15 candidate airplanes listed in Table 4.1, each of them has been assigned a label name to identify it in next stages of design.

## 4.2. Accurate Selection

The final qualitative selection relies on the AHP method as already mentioned in Chapter 2. In this section the method is explained, then it is implemented in a spreadsheet tool in order to rank the alternatives.

### 4.2.1. Method

The AHP is a widespread MCDM method able to deliver robust results. It has been implemented in a spreadsheets tool because it involves a laborious procedure with a series of computations.

#### Theory

The process is presented in detail in [21]. The core of this process can be summarized into the following key steps:

1. *Define the problem.* The alternatives, the criteria, the goal and a scale of numbers to be used for judgements.
2. *Structure the decision hierarchy.* From the top (i.e. the goal of the decision), through the intermediate levels (e.g. criteria), to the lowest level (e.g. alternatives).
3. *Construct a set of pairwise comparison matrices.* Each element is used to compare the elements in the level below. For examples: goals are used to compare criteria and criteria are used to compare alternatives.
4. *Use priorities weight in the level below.* For each element in the level below add its weighed values and obtain its global priority. Repeat this process of weighing and adding down to the bottom most level to obtain the priorities of the alternatives. For example: use the priorities of the criteria with respect to the goal to weight the priorities of the alternatives with respect to the criteria, then obtain the overall priorities by summing these weighted values.

In a pairwise comparison matrix the elements on the left are one-by-one compared with each element listed on top, an example is given in Table 4.2. The scale of numbers described in Table 4.3 indicates how many times more important one element is with respect to another element. When a number is identified from comparison, the number is entered in its proper position and, automatically, its reciprocal is entered in the transpose position.

The priorities are obtained by raising the matrix to a large power (e.g.  $B = A^{100}$ ) then summing each row (e.g.  $C_i = \sum_j B_{ij}$ ) and dividing each by the total sum of all the rows (e.g.  $D_i = C_i / \sum_i C_i$ ).

The *synthesis* is the part of the process in which the global priorities are obtained by multiplying each ranking by the priority of its criterion and summing them for each alternative.

There are two ways of obtaining priorities for the alternatives: the relative model and the rating model [21]. In both models, the priorities of the criteria with respect to the goal are obtained through a pairwise comparison.

<b>Criteria 1</b>	Design A	Design B	Design C	Design D
Design A	1	2	6	3
Design B	1/2	1	1/8	4
Design C	1/6	8	1	1/7
Design D	1/3	1/4	7	1

Table 4.2: Example of a pairwise comparison matrix used in the AHP.

<b>Intensity</b>	<b>Definition</b>	<b>Explanation</b>
1	Equal	Two activities contribute equally to the objective.
2	Weak or slight	
3	Moderate	Experiences favour one activity over another moderately.
4	Moderate plus	
5	Strong	Experiences favour one activity over another strongly.
6	Strong plus	
7	Very strong	Dominance of one activity over another is demonstrated in practice.
8	Very, very strong	
9	Extreme	The evidence favouring one activity over another is of the highest possible order of affirmation.
1/9 - 1/1	Reciprocals	If activity $i$ received one of the above numbers when compared with activity $j$ , then $j$ receives the reciprocal when compared with $i$ .
1.1 - 1.9	Similar activities	When compared with the other contrasting activities the small numbers would not be too noticeable, yet they can still indicate the relative importance of the activities.

Table 4.3: The fundamental scale of absolute numbers (from [21]).

In the relative model a pairwise comparison between alternatives is performed for each criterion to obtain the priority of each alternative with respect to the criterion, then the global scoring are obtained with the synthesis.

In the rating model some rating categories are established (e.g. "High", "Same" and "Low") for each criterion and they're prioritized by pairwise comparison. Then, rating categories are assigned to alternatives for each criterion, and before proceeding with the sythesis, the rating categories are substituted with their corresponding *idealized priorities* (priorities normalized dividing by the largest of the priorities).

In group decision making it is possible to aggregate the final outcomes of each individual expert in a group into a single representative judgement for the entire group, by using the *geometry mean* of the final outcomes. If the opinions of the experts have different importance, their judgements are raised to the power of their priorities before calculation of the geometric mean.

## Application

The method has been implemented within a few spreadsheets in both its "Relative Model" and "Rating Model" variants. In addition, it has been combined with a routine to get the outcomes of multiple different ratings.

The tool requires all possible pairwise comparisons among a given number of items, each comparison yields a rating. Then, a set of calculations are automatically executed delivering the priority of each item with respect to the criterion of the assessment.

This is done by means of a square matrix (or table) with as many rows (and columns) as the number of items to be ranked, each row number (and column number) labels a specific item. For each cell  $\langle i, j \rangle$  of the table one wonders: "How much better is item  $i$  relatively to item  $j$  with respect to the evaluation criterion?". The answer is given on the basis of the scale of number already presented in Table 4.3.

In practice, one needs to fill only the upper triangle of the matrix because the diagonal elements are unit by definition (i.e. each element is equally important to itself), while the elements below the diagonal are automatically computed with the reciprocal rule (i.e. if element  $i$  is  $n$  times better than element  $j$ , then  $j$  is  $1/n$  better than  $i$ ), see Table 4.3.

## Criteria

Previously selected 15 aircraft (Table 4.1) are pairwise compared with respect to the following selection criteria, chosen in accordance with the goal of the project.

- 1. Airframe-Propulsion Interaction.** This criterion is used to judge how much a configuration is able to exploit the benefits of hybrid-electric architecture through innovative airframe-propulsion interactions. This has been selected because leveraging on propulsion is part of the fondation of UNIFIER19 vision.
- 2. Aerodynamic Efficiency.** The reduction of chemical emission is an important design goal that depends, at a first glance, on propulsion efficiency and aerodynamic efficiency. The former is somehow included in the previous criterion, the latter is assessed with this criterion.



	1	2	3	4	5	PRIORITIES
1	1,00	2,00	2,00	1,00	0,50	0,15773
2	0,50	1,00	1,00	0,50	0,33	0,29835
3	0,50	1,00	1,00	0,50	0,33	0,29835
4	1,00	2,00	2,00	1,00	0,50	0,15773
5	2,00	3,03	3,03	2,00	1,00	0,08785

Figure 4.2: Pairwise comparison matrix for criteria priorities.

3. **Structural Efficiency.** This has been selected because indirectly affects emissions through fuel consumption, in fact an aeroplane with lower structural efficiency has higher airframe weight, thus requires more lift, more power and more fuel.
4. **Noise Effect.** Reduction of acoustic emissions is another key target for the project. It is explicitly evaluated with this criterion despite all the previous have also effect on noise.
5. **Cost and Design Complexity.** Every complexity in the design should be taken into account here, each configuration has its own. This criterion is used as a mean to account for all those aspects specific of every individual design, and that ultimately impact on cost and design complexity.

As a first step, the criteria are pairwise compared to establish their priorities in achieving the design goal. The table of the spreadsheet tool that is employed to this purpose is shown in Figure 4.2. The row/column numbers refer to criteria according with the enumeration given above.

The numbers in the upper triangle have been assigned based on discussions in a group meeting, the spreadsheet automatically computes the numbers in the lower triangle and the priorities in the right column. It can be seen that criteria 2 and 3 (i.e. aerodynamic and structural efficiencies) turned out to be most important, followed by criteria 1 and 4 (i.e. propulsion and noise), and last cost and design complexity.

### Relative Model

Inside the 5-by-5 table depicted in Figure 4.2 the 5 selection criteria are pairwise compared with respect to the design goal. The "Relative Model" take advantage of the same procedure to compare the 15 candidate configurations with respect to each of the 5 selection criteria. This means that 5 tables have been filled out similarly to what is done in Figure 4.2, each of them has 15 rows and columns.

When all the tables have been compiled, the priority of each configuration with respect to each criterion is calculated automatically, in addition the algorithm combines these priorities together as described above to obtain the priority of each candidate with respect to the design goal.

	VERY HIGH	HIGH	NORMAL	LOW	VERY LOW	NORMAL.	IDEAL.
VERY HIGH	1,00	0,50	0,33	0,25	0,20	0,41594	1,00000
HIGH	2,00	1,00	0,50	0,33	0,25	0,26417	0,63511
NORMAL	3,00	2,00	1,00	0,50	0,33	0,16065	0,38623
LOW	4,00	3,00	2,00	1,00	0,50	0,09786	0,23529
VERY LOW	5,00	4,00	3,00	2,00	1,00	0,06138	0,14758

Figure 4.3: Ratings-to-priorities for criterion 3 "Aerodynamic Efficiency".

CRITERIA	1	2	3	4	5	RESULTS		
PRIORITY	0,15773	0,29835	0,29835	0,15773	0,08785	TOTAL	NORMAL.	IDEAL.
1	HIGH	HIGH	LOW	HIGH	NORMAL	0,49396	0,06800	0,10832
2	VERY HIGH	NORMAL	LOW	HIGH	LOW	0,46400	0,06388	0,10175
3	VERY LOW	HIGH	VERY HIGH	NORMAL	HIGH	0,62782	0,08643	0,13767
4	NORMAL	VERY HIGH	VERY LOW	HIGH	VERY LOW	0,51644	0,07110	0,11325
5	LOW	HIGH	VERY LOW	VERY HIGH	VERY LOW	0,44132	0,06076	0,09677
6	HIGH	HIGH	NORMAL	NORMAL	NORMAL	0,49974	0,06880	0,10958
7	HIGH	VERY HIGH	VERY LOW	HIGH	LOW	0,56340	0,07756	0,12354
8	NORMAL	NORMAL	LOW	HIGH	LOW	0,36719	0,05055	0,08052
9	HIGH	HIGH	LOW	NORMAL	LOW	0,44144	0,06077	0,09680
10	HIGH	HIGH	LOW	NORMAL	NORMAL	0,45470	0,06260	0,09971
11	HIGH	HIGH	LOW	NORMAL	LOW	0,44144	0,06077	0,09680
12	HIGH	VERY HIGH	VERY LOW	HIGH	VERY LOW	0,55569	0,07650	0,12185
13	NORMAL	HIGH	LOW	LOW	LOW	0,37838	0,05209	0,08297
14	HIGH	HIGH	LOW	NORMAL	NORMAL	0,45470	0,06260	0,09971
15	HIGH	VERY HIGH	VERY LOW	HIGH	LOW	0,56340	0,07756	0,12354

Figure 4.4: Ratings of candidate configurations.

### Rating Model

The "Rating Model" is slightly different from the "Relative Model": a *rating scale* is defined for each criterion (e.g. "High", "Medium" and "Low" with a proper definition of what each means). Then their priority are obtained with the same AHP methodology utilized before. This is shown in Figure 4.3, for instance with the criterion 2 "aerodynamic efficiency".

The same procedure is applied to all the selection criteria, then each configuration is judged with respect to each criterion using the relevant rating scale defined before (see Figure 4.4). The row numbers correspond to configurations according with enumeration given in Table 4.1, while column numbers refer to criteria following the enumeration given above in this section.

Automatically, each text rating is substituted with the correspondent priority, thus tracing back to the same situation of the "relative model". The algorithm also computes the priority of each candidate with respect to the design goal, as per the "relative model" (right columns).

---

## Results Aggregation

The spreadsheet tool can be utilized by many experts, or with various scale of numbers, or even with different criteria, besides the fact that it offers two diverse variants of the method.

In the end, multiple outcomes are combined together through a geometric mean as anticipated at the beginning of the section, so as to have the single vector of priorities that ranks the candidate airplanes in Table 4.4.

### 4.2.2. Remarks on Ratings

Many aspects are considered when a score is assigned, however the immense amount of pairwise comparison conducted makes it inconvenient to comment every rating. This part of the document attempts to provide an understanding of the overall thinking behind each rating.

#### Selection Criteria

High aerodynamic and structural efficiencies drive the selection criteria because they intrinsically play a key role in the reduction of both acoustic and chemical emissions. Chemical emissions are reduced as a consequence of the lesser power required and thus lower fuel consumption. In addition, a lighter and more efficient aircraft causes lower air displacement leading to reduced noise, beside the fact that it pulls down both production and operative costs. Therefore, these criteria act indirectly also on two other selection criteria. A substantial increase in aerodynamic and propulsive efficiency can be achieved by exploiting propulsive-airframe interactions, hence this deserves to be a selection criterion of great importance as it promotes lower emissions indirectly. A selection criterion is used to discern the noise effect specific of each individual configuration, but its importance is considered secondary to the achievement of reduced chemical emissions. Costs and design complexity are not of much interest because the abatement of the environmental impact of such a service is deemed imperative.

#### Airframe-Propulsion Interactions

The hybrid-electric architecture is likely the best option to attain the design goals thanks to its unique capability of controlling emissions and providing operational flexibility. However it brings also some drawbacks that should be balanced as much as possible. This criterion is used to judge how much advantage a configuration takes from the use of a hybrid-electric architecture. For instance, a configuration with just a nose propeller does not exploit much benefits of a hybrid-electric architecture, as the propeller can be directly driven by a traditional thermal engine. On the contrary, a configuration which uses both DEP and PCA is able to exploit much benefits of a hybrid-electric architecture because those technologies provide additional advantages that are not accessible with traditional thermal engines. The effect on propulsive efficiency is also accounted here.

### Aerodynamic Efficiency

The aerodynamic efficiency is improved in many ways among the pre-selected candidates. Some of them take advantage from the reduction of induced drag ensured by a box wing or a high aspect ratio TBW. Others rely on a reduced zero-lift drag thanks to a "laminar flow fuselage" or the minimized wetted area of a BWB. Tail configurations like the TSA or the canard may permit lower trim drag. Special aircraft layouts such as the BWA or the BWB give the opportunity to better integrate the vertical fin in the airframe causing an overall reduction of weight and drag. The effect on aerodynamic efficiency due to propulsion-airframe interaction is accounted with this criterion.

### Structural Efficiency

This criterion evaluates how much weight increase is expected with respect to a traditional aircraft. This may be due to the inherent structural requirements of a particular solution but also due to the lower knowledge and experience with the structural optimization of a very new shape. High aspect ratio comes with an inherent weight penalty, a BWA or a BWB may suffer a low structural efficiency caused by lack of previous design experience of flying real scale models.

### Noise Effect

An article from NASA [63] helped in weighting the contribution to noise of various parameters. They developed a theory-based empirical relationship which showed the important parameters for the prediction of the aerodynamic noise OASPL (Over-All Sound Pressure Level) to be: Mach number, wing area and aspect ratio in addition to the normal distance factor. The equation is given by the simple expression:

$$\left. \begin{array}{l} \text{Overall} \\ \text{Radiated} \\ \text{Noise (dB)} \end{array} \right\} = 10 \log_{10} \left[ \frac{(\text{Mach Number})^6 (\text{Wing Area})}{(\text{Distance})^2 (\text{Aspect Ratio})^4} \right] + \text{constant} \quad (4.1)$$

The equations highlight the positive effect on noise induced by high aspect ratio wing and lower wing area, thus higher wing loading.

Other considerations are based on findings discussed in articles, already summarized in Chapter 2. For example, it has been estimated a reduction of noise due to the use of DEP, and a possible increase of acoustic emissions caused by BLI.

### Cost and Design Complexity

All the configurations proposed are thought to operate as passengers and cargo aircraft as well, this makes difficult to predict how much effort is required to re-configure each alternative at this stage of the project. Costs are also still unpredictable, anyway we can judge how much work is required to complete the design and certification of a configuration, based on the amount of studies already present in literature and on the level of similarity to existing airplanes.
















Score	Label	Definition		
		Layout	Wing	Propulsion
	0.22759 C3	Canard with " <i>laminar flow fuselage</i> ", VIW and BLI		
	0.20612 C12	Tailless	TBW	DEP, WTP and BLI
	0.20415 C2	Canard PCA with DEP, WTP and BLI		
	0.20373 C7	Aft Tail	TBW	DEP, WTP and BLI
	0.19857 C15	TSA	TBW	DEP, WTP and BLI
	0.19850 C6	Aft Tail	Cantilever	DEP, WTP and BLI
	0.19420 C4	BWB with with asymmetric BLI-DEP		
	0.19419 C9	Aft Tail	Box Wing	DEP and BLI
	0.19399 C11	Tailless	Cantilever	DEP, WTP and BLI
	0.19380 C10	Canard	Cantilever	DEP, WTP and BLI
	0.19188 C5	BWA with DEP		
	0.19121 C1	Aft Tail	TBW	DEP and WTP
	0.18676 C14	TSA	Cantilever	DEP, WTP and BLI
	0.18284 C13	Tailless	Cantilever	WTP and BLI
	0.17913 C8	Aft Tail	Box Wing	DEP

Table 4.4: Ranked list of candidates with scores attained in the AHP.

### 4.2.3. Results

Table 4.4 presents the results obtained with the application of methods previously discussed in this chapter. The histogram on the left side depicts the ratings attained by each candidate at the end of the entire evaluation procedure. As anticipated, the rank is the result of geometric mean among multiple different application of the AHP. A good robustness of these results is highlighted by the presence of many similarities in the individual rankings. Moreover, there are any evident unexpected behaviours and just a few switch of positions in the chart. Colors show the natural clustering inspired by discrete jumps in scoring.

Configuration C3 stands out among all the others thanks to its relatively simple design that ensure great aerodynamic and structural potential while exploiting propulsion-airframe interaction.

At a first glance one may just take the first four or six top-rating candidates (i.e. C3, C12, C2, C7, C15 and C6), however it can be noted that configurations C12, C7 and C15 are quite similar. Moreover, there is little difference of score between C12 and C7, as well as between C15 and C6. These crucial properties drive the final selection of the candidate airplanes. In fact, little difference in performance is expected among C15, C7 and C12 but the available tools are able to perform the sizing only of the more traditional C7. For this reason configuration C12 and C15 have been temporarily excluded, leaving configuration C3, C2, C7 and C6 (see next section and Table 4.5).

Label	Score	Description
<b>C3</b>	0.22759	Tube-and-wing layout with control-type canard, cantilever wing, bullet-shape axis-symmetric "laminar flow fuselage", variable incidence wing and a coaxial tail cone propeller. The shape of the fuselage minimizes aerodynamic drag both by attaining laminar boundary layer on a vast area, and by removing the tail upsweep. The TCP yields increased propulsive efficiency through BLI. The VIW is used to avoid tail strike during take off maneuver.
<b>C2</b>	0.20415	Tube-and-wing layout with control-type canard, cantilever wing, blown low-wing (DEP, WTP) and a tail cone propeller placed higher. The vertical offset among thrust sources enables propulsion control over pitch axis, while the spanwise distributed wing propellers ensure yaw and roll controls. This minimizes the control surfaces both in number and sizes.
<b>C7</b>	0.20373	Tube-and-wing layout with aft tail, strut braced high aspect ratio wing and a tail cone propeller. The wing is blown with a number of propellers (DEP, WTP).
<b>C6</b>	0.19850	Tube-and-wing layout with aft tail, cantilever blown wing (DEP, WTP) and a tail cone propeller.
<b>C0</b>	-	Tube-and-wing aircraft with aft tail, cantilever wing, and twin wing mounted propellers. Hybrid-electric aircraft used as baseline to assess additional innovative technologies introduced by the candidates.
<b>REF</b>	-	Traditional aircraft with aft tail, cantilever wing, twin wing mounted turboprop. Clean "zero-innovation" 2025 aircraft used as reference in comparisons.

Table 4.5: List of aircraft for sizing and assessments.

### 4.3. Candidate Configurations

Table 4.5 lists the aeroplanes selected to be taken forward to the sizing stage, each of them is described at the available level of detail. Two more traditional configurations are added to those selected in previous section, namely C0 and REF, as a benchmark for future numerical comparisons.

## 5. Sizing Methodology

The parameters needed to perform a quantitative comparison and ranking of the candidates are determined through a sizing methodology developed by the FMSlab of DAER in Politecnico di Milano. Here a brief presentation is given about the tools that constitute this sizing procedure, namely *Hyperion*, *Argos* and *Titan*.

The candidate configurations incorporate many advanced features that have not been completed yet in the deployed tools, this chapter also treats the modelling of these technologies and the estimation of the relevant parameters.

### 5.1. Description of Sizing Tools

This section introduces the tools used to carry out the preliminary sizing of the candidate configurations.

The first one, Hyperion, has been used extensively within the very early design phases to discriminate the effect of various propulsion alternatives (i.e. THE, GH2, LH2) and to validate the results of the qualitative selection. It has also been used for the sizing of the reference aircraft (with conventional layout and propulsion).

Argos, has never been used as standalone but always as part of Titan. The latter, provides the final sizing results, that are compared for selection and delivery.

#### 5.1.1. Hyperion

Hyperion (HYbrid PERformance SimulatIOn) is a methodology developed at Politecnico di Milano. A complete description of this method is present in [7]. Here just a brief description of the methodology and its capability is given. In Figure 5.1 the main flow chart of Hyperion is shown.

Hyperion performs the preliminary sizing of pure-electric (PE) and hybrid-electric (HE), propeller-driven, fixed-wing air vehicles of arbitrary size and mission requirements, providing the design weights, the propulsive plant sizing, and the overall aircraft dimensions [7].

It includes energy management strategies that are peculiar to electrically-driven aircraft, such as PE operation on terminal maneuvers, and energy recuperation during descent via propeller wind-milling.

The procedure relies on a more detailed mass breakdown compared to the traditional formulation: the operational empty mass is expanded and its estimation is achieved term by term by means of a proper statistical regressions at subsystem level, or other applicable models.

Firstly, an appropriate design point is chosen on the Sizing Matrix Plot (SMP), this means that the design wing loading and the design power loading are selected within the feasibility region, ensuring compliance with all the performance

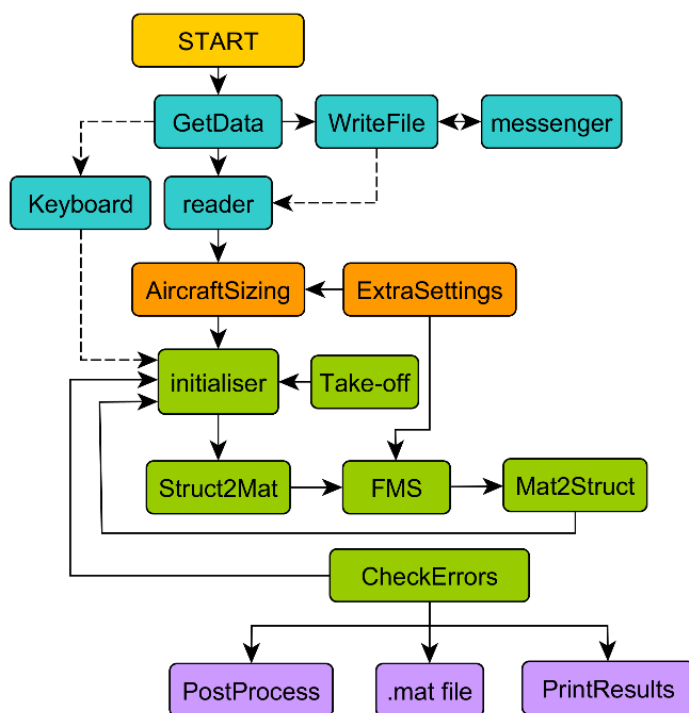


Figure 5.1: Flow chart of the outermost Hyperion loop [7].

constraints imposed by design requirements and/or regulation.

Then, the energy sources and power supply devices are sized and the mass of each component is estimated.

These two steps are repeated until the mass breakdown converges. Such an iterative procedure is required because the classical separation between design mass, power loading and wing loadings fails with PE and HE propulsion.

Finally, the full sizing mission is simulated by a time-marching algorithm, providing insights on the time evolution of the powertrain dynamics, and leading to small adjustments on the initial estimations that however, do not require an update of the masses of the components.

Hyperion functionalities have been repeatedly expanded and enhanced from its birth: the ability of sizing aircraft that features a blown-wing (DEP) has been included [38], and also a routine to size LH2 tanks of hydrogen-electric airplanes [35].

### 5.1.2. Argos

Argos (AiRcraft GeOmetric Sizing) is a methodology developed at Politecnico di Milano. It integrates and automates the sizing procedures of the main subsystems of an aeroplane, delivering a comprehensive and thorough preliminary aircraft sizing.

It requires a number of input parameters coming from an initial rough sizing of the vehicle (e.g. wing area, fuel mass, installed power). Then, it executes a series of consecutive and/or nested sizing loops as depicted through a flow chart in Figure 5.2, where each block may contain further sizing loops depending on the subsystem involved.

A brief overview of the methods and their outcomes is given below, details are exhaustively treated in [8].



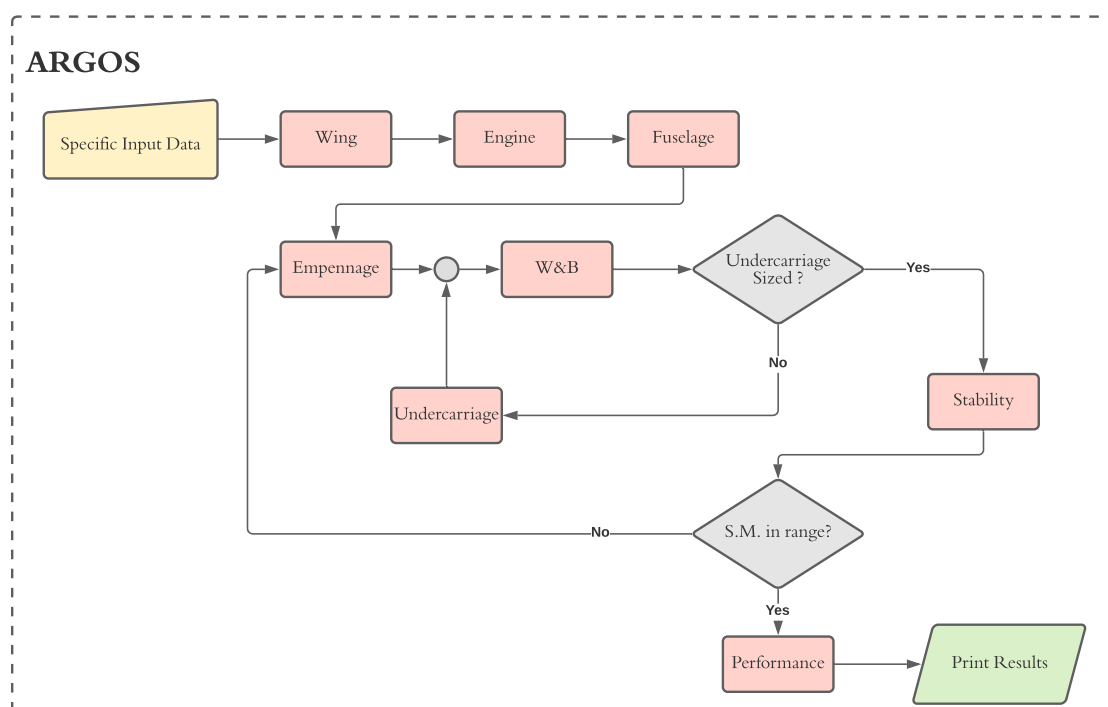


Figure 5.2: Flow chart of the outermost Argos loop [8].

**Wing.** The best airfoil is selected from a database, according to the required maximum lift coefficient and design lift coefficient.

The taper ratio and twist of the wing are calculated to obtain the minimum induced drag coefficient for the design lift coefficient, based on lifting line theory.

The sweep angle is calculated to minimize compressibility effects only for cruise Mach over 0.65.

The high-lift devices are sized based on their type (plain, split, slotted, Fowler) and spanwise start/end locations, providing as output their drag contribution and their geometrical dimensions such as area, chord, deflection.

**Engine.** Engines, motors, propellers, PGS, batteries and tanks dimensions are estimated based on their power using statistical models, some of them purposely derived for the software.

**Fuselage.** The fuselage is sized to comply with regulations and with a desired slenderness ratio (i.e. the ratio between the length of the fuselage and its external diameter).

Number of aisles, number of flight assistants, number of lavatories and cargo/-baggage volume are selected and used to estimate the dimensions of the cabin, including seats arrangement.

If present, batteries are placed in the wing box and/or below the cabin floor. Cargo/baggage is positioned below the cabin floor and/or in the tailcone. If necessary, further volume is added by means of a cargo bay located behind the cabin.

In case of hybrid-electric aircraft the PGS is placed in the tailcone, the cylindrical GH2 tanks are installed over the cabin roof, the (almost) spherical LH2 tank is arranged behind the cargo sector.

**Empennage.** The horizontal and vertical tail are sized together with the wing dihedral to meet stability requirement.

**Undercarriage.** The landing gear is sized to ensure vehicle stability on ground, and to ensure tail-strike clearance at take off and landing.

**Weight and Balance.** The mass is estimated for of each sub-system such as wing, fuselage, motors, electrical system, and others.

The center of gravity is estimated for all the components, and for the entire aircraft in multiple configurations (e.g. empty and loaded).

### 5.1.3. Titan

Titan is a tool that results from the integration of Hyperion and Argos, described in the previous lines.

The sizing procedure starts with Hyperion that provides an initial solution, then Argos employs the output of Hyperion to size the main subsystems of the airplane, thus producing a more detailed preliminary sizing. These steps are repeated in a loop in which the results from Argos are given as feedback to Hyperion until the error between their MTOM estimations falls within a small tolerance.

At the end of the routine, the results are reported to the designer in several formats as required: 3D conceptual representation of the vehicle, data files, graphs, textual reports, and so forth.

Figure 5.3 shows the flow chart of Titan as described above. Further details are presented by the authors of the tool in [8].

## 5.2. Modelling of New Technologies

The comprehensive review of the technologies, summarized in Chapter 2, included several promising innovations that were not considered in previous works concerning the development of the sizing tools. After a first qualitative selection of the candidates, the sizing stage has been delayed to permit the update of the sizing tools with specific provisions for the novel technologies included in the selected configurations.

As said in Section 5.1, the tools already have the ability to consider many advanced propulsive solutions such as THE, FC with GH<sub>2</sub> or LH<sub>2</sub> storage systems, and the DEP with blown wing.

The missing technologies have been listed and their relevance on the results has been assessed, below a quick recap of the taken decisions.

The benefits of **WTP** are partially accounted for in the sizing routine of the blown wing, which considers the contribution to lift and drag given by the increase of air speed across the wing. The second positive effect of enhancing wing span efficiency has been conservatively neglected, as a proper simplified model is not yet ready and it requires much time to develop. Additionally, a further propulsive advantage may be exploited whenever the propeller is mounted in pusher configuration, as already mentioned in Chapter 2.

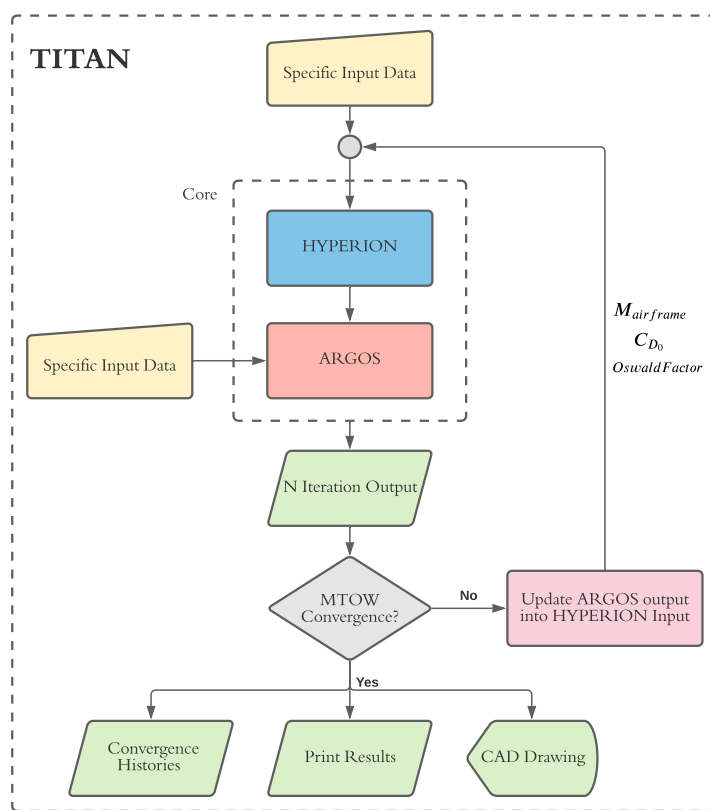


Figure 5.3: Flow chart of Titan [8].

The effect of **BLI** enabled by the Tail Cone Propeller (TCP) is estimated from values found in literature, as multiple studies predicted comparable increments of propulsive efficiency with similar conditions. For example, in [64] they estimated a +5% propulsive efficiency at cruise for the EADS VoltAir which employs a tail cone fan, slightly higher values are mentioned in Chapter 2. The TCP of the proposed candidate configurations boast a +6% propulsive efficiency with respect to the baseline.

Configuration C3 features a **laminar flow fuselage**, as pointed out in Chapter 4 this name should not be taken literally. The fuselage is shaped to promote a wider portion of laminar boundary layer, and a further drag reduction is provided by an axis-symmetric tail cone. These effects are accounted in a decrease by 0.004 of the value of zero-lift drag, corresponding to about -13% from baseline. The estimation is carried out with methods suggested in [65], and it stand on the same order of magnitude of the prediction found in [64] for the EADS VoltAir which exploits a fairly comparable bullet-shape fuselage (specifically, they calculated 15% smaller parasite drag coefficient due to laminar flow, and a further -5% thanks to fuselage shape, however they considered 60% of laminar flow over wings).

Configuration C3 also exploits a **VIW**, as a solution to prevent tail strike during take off roll. The main effect of VIW is a penalization of the empty mass, measured as +3% based on considerations discussed in [65] relatively to a variable sweep wing. Other potentialities of this feature have been highlighted during selection but not assessed or included in the preliminary sizing, because of the current poor level

of confidence due to lack of on-going studies.

This last thought applies also to **PCA**, in fact the aircraft empty mass may be positively affected by this technology thanks to the possibility to remove some control surfaces, however clear quantifications are not yet possible.

At first, the **TBW** effects were accounted through an increase of aspect ratio, followed by an increase in parasite drag of 0.002 due to the presence of the struts, and a +3% increase in empty mass due to higher wing span. These estimations were carried out with methods and considerations found in [65] concerning analogous topics. Then, much more effort has been invested with the *Analytical Modelling of a Strut Braced Wing* presented in Section 5.3 and deepened in Appendix A.

Finally, a number of tail configurations are required, such as the **Canard**, the Tailless aircraft, and the TSA. A prioritization of the tasks led to modelling of only the first one, in a parallel thesis activity. Very shortly, the procedure adopted for the geometric canard sizing is intended for control-type canard, and not for lifting-type canard. The wing is placed as far aft as possible, excluding the fuselage rear cone, next, the canard is sized to minimize its area, while attaining a given static margin, and paying attention to controllability constraints.

### 5.3. Strut Braced Wing

As anticipated, the introduction of novel technologies in the design raised the need for the study and implementation of novel sizing techniques. This section presents the core part of the study carried out as *Analytical Modelling of a Strut Braced Wing*, where many details have been moved to Appendix A to preserve the train of thought.

The aim of the work is to quantitatively catch the effects of a high aspect ratio wing coupled with a supporting frame able to reduce the stress in the structure. The increased aspect ratio is generally desirable for a couple of reasons such as the reduction of induced drag, however the correspondent increase in wing span would seriously increase the mass of a traditional cantilever wing. The deployment of a proper structure in support of the wing may not only permit a reduction of mass of the wing assembly with respect to an equivalent cantilever wing (i.e. with same span), but also a reduction in wave drag and profile drag thanks to the less stringent requirements on the wing box structure, and the related possibility to select a thinner airfoil. The main cons are clearly the drag contribution of the additional structural elements, and the possible mass increase with respect to a normal cantilever arrangement (i.e. with normal span).

There exist a lot of articles and studies on this innovative technology, some examples were already mentioned in Chapter 2. However, most of the approaches adopted in literature to model this technology include a Multidisciplinary Design Optimization (MDO) with some advanced modelling of the wing assembly based on a Finite Element Method (FEM). Such an approach delivers high-fidelity results, and configurations that are already overall optimized, but it requires computational-expensive tools and a wide knowledge of the baseline aircraft and its design variables, making it inadequate for a very initial conceptual analysis. For the same reason, the results present in literature are very specific for those aircraft and cannot be adjusted to our candidate configuration. Finally, the MDO acts on many design

parameters inside its sizing loops making it difficult to isolate the pure effect of the TBW.

Thus, it has been decided to put resources on developing a simple analytical model.

### 5.3.1. Method

The root intention was to obtain a set of equations that could be used to estimate wing-assembly mass and drag involving only variables that are available with a minimal knowledge of the aircraft (e.g. wing area, aspect ratio, MTOM). The analytical nature of this model also enable simply assessment of the effects on the results of each design variable.

The structural model is based on the well known Euler's beam, which is extensively treated in literature and classes, for example in [66]. Despite its simplicity, it turned out to be quite suitable to understand the problem and to formulate rational predictions. The supporting structure is conceptualized as a simple strut that links to the fuselage from a location along the wing. The equations are derived in a nondimensional fashion aiming at maximum generality, with all the case-specific parameters grouped apart. The width of the fuselage is ignored, this means that the semi-wing is considered as clamped to the longitudinal symmetry plane. This simplification is needed to avoid the presence of fuselage width inside equations, but it is a rather conservative assumption resulting in longer beams, and so higher bending moments. The wing taper, sweep angle, twist, dihedral angle, and the possible presence of multiple airfoils are neglected, or in other words, the wing is considered rectangular, planar, untwisted and with a constant airfoil along the span.

The same modelling approach has been also applied to a cantilever wing, for the purpose of providing a fair comparison and an exhaustive validation.

The estimation of the aerodynamic drag term due to the strut relies on a common method available in literature [65], for sake of completeness this is shown in Appendix A.

### Load Distribution

A comprehensive structural sizing cannot prescind from a verification of a vast number of scenarios, where each of them exhibits a static or dynamic aero-elastic behaviour characterized by a peculiar load and stress distribution that may dictate the sizing. Such a complicated procedure does not lend itself to an analytical formulation, but at this early design stage a gross and simpler sizing procedure can be adequate. Therefore, only one single static sizing load condition that represent the theoretical spanwise elliptical lift distribution at the ultimate load factor has been considered.

The elliptical lift distribution is usually desired and pursued throughout the aerodynamic wing design as it minimizes the induced drag, but in the end the distribution can be different due to many reasons, such as the presence of control surfaces or swirl from propellers. A parabolic and a linear load distributions are utilized as forerunners to get elucidating or simplified equations (specially when multiple subsequent integrations are needed to obtain wing displacements), but also to qualitatively judge the effect of deviations from the ideal case, as a sort of rudimental uncertainty analysis.

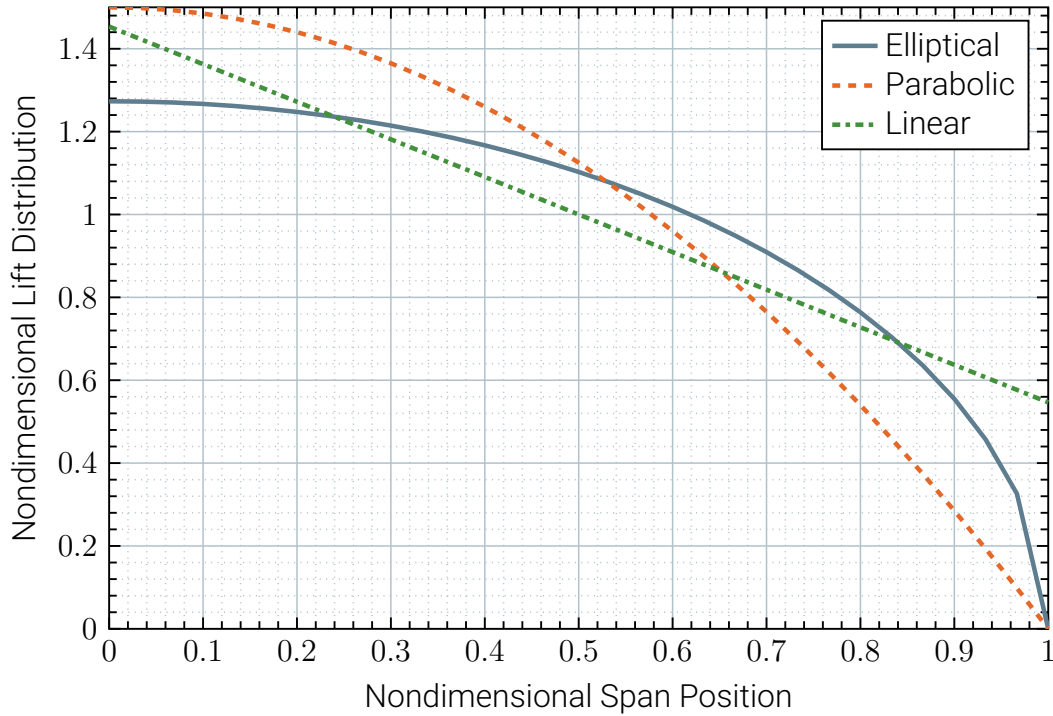


Figure 5.4: Nondimensional lift distribution comparison.

In Figure 5.4 the three load distributions are compared, their expressions and other relevant details can be found in Appendix A.

### Section Properties

The outcome of a structural sizing depends on the load as discussed above, on the performance of the selected resisting material, and also on the geometrical properties of the resisting section, namely: the section area and its spread over the section plane.

Figure 5.5 shows respectively a double plate and a semi-monocoque idealization of the wing section. From these idealization it seems reasonable to assume that the radius of gyration  $r_g$  is roughly equal to half of the airfoil thickness  $t$ , and that this is also more or less equal to the maximum distance to the elastic axis  $y_{\max}$ . In fact, the resisting fibres are usually located on the contour of the wing box, which has approximately a constant height and it is almost symmetric with respect to chord line. This can be written as:

$$r_g \approx y_{\max} \approx \frac{1}{2}t = \frac{1}{2}(t/c)c = \frac{1}{2}(t/c)\frac{b}{\lambda} \quad (5.1)$$

This assumption allows to write specific geometrical section properties such as  $r_g$  and  $y_{\max}$  in terms of quantities easily available at a conceptual stage, i.e. thickness-to-chord ratio  $(t/c)$ , wing span  $b$  and aspect ratio  $\lambda$ .

The definitions of the required section properties are given in Appendix A, where some useful relations are also derived and exploited to simplify subsequent equations.

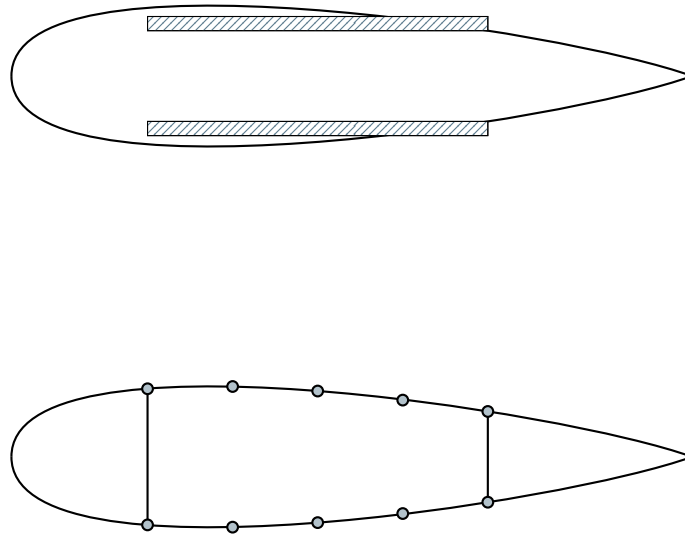


Figure 5.5: Double plate (above) and semi-monocoque (below) structural idealizations of a wing section.

### Structural Sizing

The structural sizing of the wing box is carried out as a classical exercise of beam analysis. The constraint reactions are calculated starting from the loads through a set of equilibrium equations, then the internal forces and moments are obtained as functions of the spanwise coordinate, and with them, also the maximum stress peaked at each spanwise position. The contribution of shear and torsion to the stress are neglected, in virtue of the ordinary values of aspect ratio and aerodynamic moment coefficient. Axial force is included.

The optimal structural sizing in terms of mass is achieved when each section along the span of the wing is sized to withstand exactly the local maximum stress. In other words, when the resisting area changes continually along the span, in such a manner that the maximum stress section-wise remains constant and equal to the maximum tolerable stress for the specific material utilized.

On the contrary, the worst (rational) structural sizing in terms of mass takes place when the resisting section is kept constant all along the span, and therefore it is sized to withstand a maximum stress that is potentially experienced only in a single spanwise location.

The bare-structure wing mass is evaluated both in the optimal  $m_{w,\text{variable}}$  and in the worst  $m_{w,\text{constant}}$  case, and a coefficient  $\kappa_{opt}$  is defined to quantify the *level of structural optimization* by means of a linear interpolation between these two limit sizing (see eq. 5.2). Rationally, the mass of the resisting material  $m_w$  is calculated as:

$$m_w = m_{w,\text{constant}} + \kappa_{opt}(m_{w,\text{variable}} - m_{w,\text{constant}}) \quad (5.2)$$



Aeronautical airframes are designed to be extremely efficient with most of the material contributing to the structural strength (e.g. skin, tank), specially when composite materials are used (e.g. epoxy replaces rivets and sealant). Moreover, the mass of the various systems and of the control surfaces are frequently accounted separately. On this basis, the mass of the wing is confused with the bare-structure wing mass, and the error is hidden in the uncertainty of the attainable level of structural optimization.

At first, the knowledge of wing stiffness and wing displacements appeared of major importance for a fair sizing and comparison of the two alternatives, nevertheless, after further analysis, it has been concluded that a sizing based only on stress was appropriate. Hence, the displacement equations were derived (only with parabolic load distribution to attain manageable expressions) and they can be found in Appendix A, together with other quantities that played a minor role in the study.

This whole process has been summarized in few lines, still, it involves many equations that can be reused in other works, and that may be useful to better appreciate the logic; refer to Appendix A for a deeper insight.

### 5.3.2. Results

Shear and axial forces, bending moment, stress and wing assembly mass of cantilever and strut braced wings are presented and compared through graphs in Appendix A (respectively in figures A.8, A.9, A.10, A.11 and A.12). It stems that stress is generally much smaller for a strut braced wing with respect to an equivalent cantilever wing, and this may lead to a great mass reduction depending on geometrical arrangement (particularly on the strut breakpoint location). The difference among the three considered load distributions has a minor impact on results.

The normalized strut breakpoint location  $\chi_s$  is defined as the ratio between the spanwise coordinate of the strut breakpoint over half the wing span, thus  $\chi_s = 0$  represent a strut linked with the root of the wing, while  $\chi_s = 1$  indicates a strut linked to the tip of the wing.

The optimal location for the strut breakpoint  $\chi_{s,opt}$  has been established, the value is specific for the three different load distributions considered but with little variation (i.e. between 55 and 65 % of semi-span from wing root).

The main contribution to the stress along the wing is given by the bending moment, showed in Figure 5.6 for different strut breakpoint  $\chi_s$  (parabolic lift distribution).

The location of the most stressed section depends on the strut breakpoint position, specifically, it is at the strut breakpoint for  $\chi_s$  lower than  $\chi_{s,opt}$  and it moves in-between fuselage and strut breakpoint when  $\chi_s$  is greater than the optimal value.

A practical analytical expression for the maximum stress can be obtained only for  $\chi_s \leq \chi_{s,opt}$ , as well as the equation for the mass of a strut braced wing with constant section. The mass of the variable section strut braced wing requires the numerical solution of an integral that depends on  $\chi_s$ , the integral has been evaluated for a vast number of  $\chi_s$  and the results of a polynomial interpolation have been provided to allow manual calculations. In case of cantilever wing all the derived formulas are entirely analytical. Much more details are given in Appendix A.

Finally, the strut has been verified for buckling, which revealed to bear a key-role in the selection of the wing geometry parameters such as the strut breakpoint



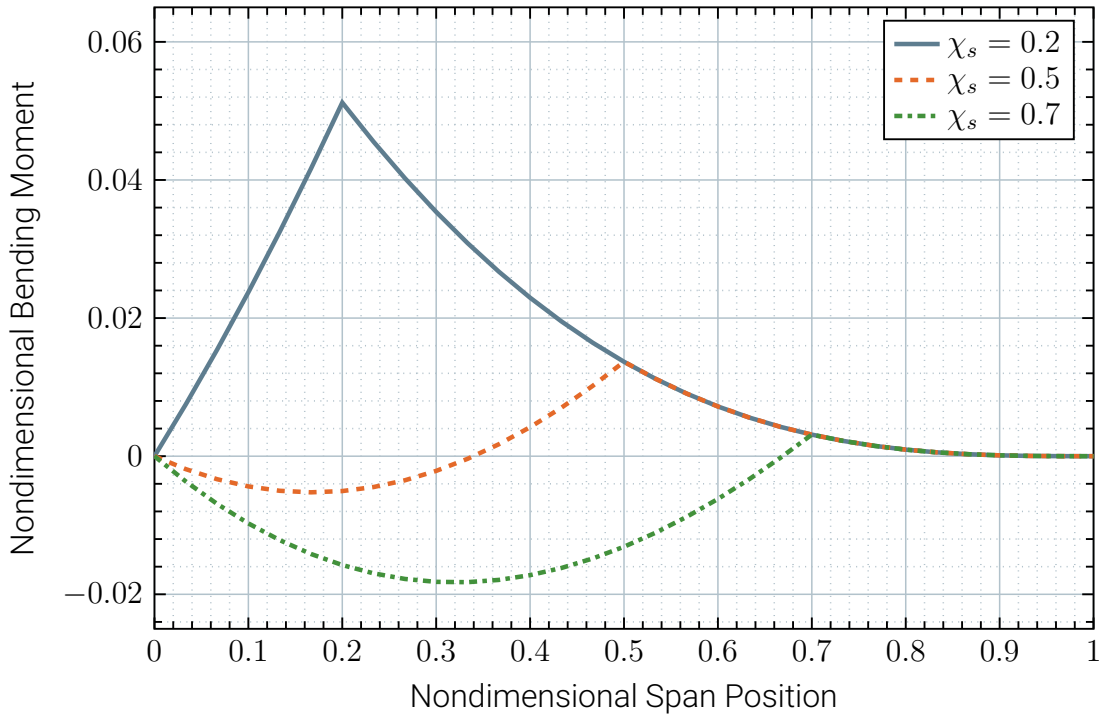


Figure 5.6: Bending moment comparison for different  $\chi_s$ .

location or the minimum thickness of the strut cross-section (see Appendix A).

### 5.3.3. Validation

The mass of the cantilever and strut braced wing are predicted with the methodology presented in this section, here they are compared with data gathered from literature. As anticipated, the considered lift distribution is elliptical.

The equation for the mass of a wing depends on the sizing load, defined as:

$$L = n_{ult} m_{TO} g \quad (5.3)$$

where  $m_{TO}$  is maximum take off mass of the aircraft,  $g$  is gravity acceleration, and  $n_{ult}$  is the ultimate load factor that is computed from the maximum operative load factor  $n_{max}$  through a safety coefficient of 1.5:

$$n_{ult} = 1.5 n_{max} \quad (5.4)$$

The safety factor of 1.5 is also used to calculate the maximum allowed stress  $\sigma_{max}$  for the limit stress of a given the material  $\sigma_{lim}$ :

$$\sigma_{max} = \sigma_{lim}/1.5 \quad (5.5)$$

Equation 5.6 represent a prototype equation obtained from this estimation approach, specifically it is the mass of a constant section cantilever wing (find more in Appendix A). As a first crude means of validation, the expression involves the same parameters required by the majority of historical-statistical wing mass estimation

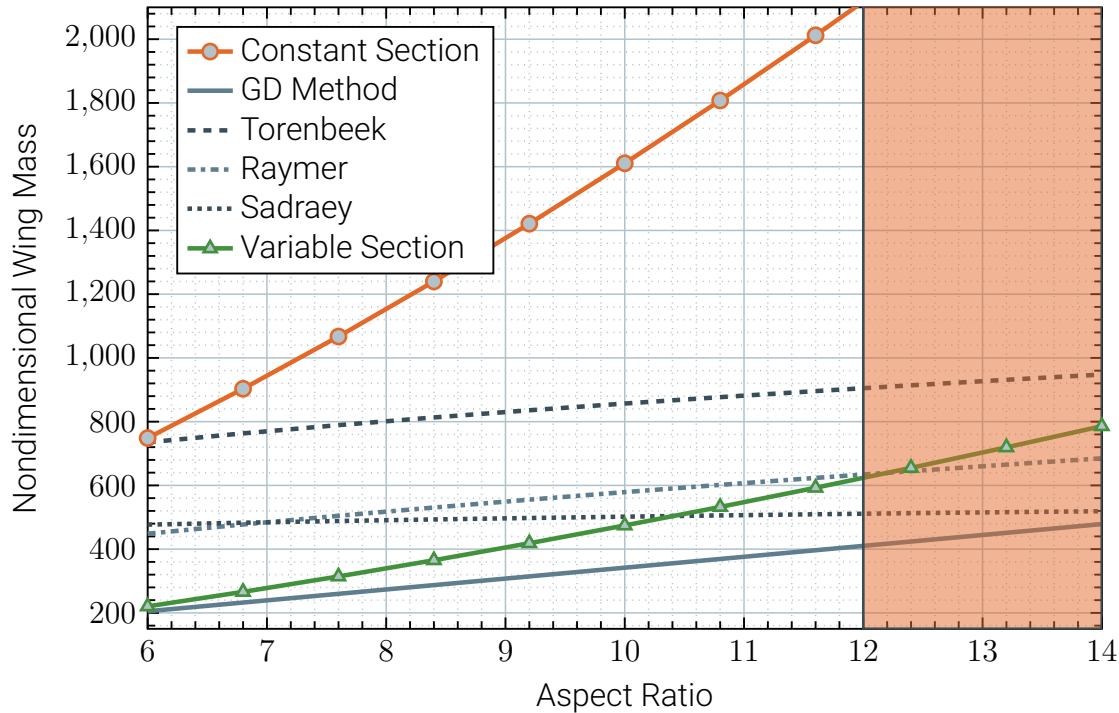


Figure 5.7: Wing mass comparison among various statistical equations valid for commercial aircraft and the proposed analytical model.

formulas (also reported in A).

$$m_0 = \frac{2}{3\pi} (n_{\text{ult}} m_{\text{T0}} g) \frac{\rho}{\sigma_{\text{max}}} \frac{\sqrt{\lambda_0^3}}{(t/c)} \sqrt{S} \quad (5.6)$$

### Commercial Aircraft

Figure 5.7 shows comparison between cantilever wing weight calculated with the analytical model and some statistical equations taken from [22], [65] and [67]. Details concerning the involved statistical equations are provided in Appendix A.

These statistical equations are limited to aspect ratios of commercial aircraft, here considered below 12. The parameters used for the graphs in Figure 5.7 are: ultimate load factor  $n_{\text{ult}} = 1.5$ ,  $n_{\text{max}} = 3.75$ , maximum take off mass  $W_{\text{T0}} = 8500$  kg, thickness-to-chord ratio  $(t/c) = 0.12$ , wing area  $S = 32 \text{ m}^2$ , rectangular wing (unswept, untapered), aluminium alloy ( $\rho = 2768 \text{ kg/m}^3$ ,  $\sigma_{\text{max}} = \sigma_{\text{lim}}/1.5 = 170 \text{ MPa}$ ), maximum level flight Mach  $M_H = 0.30$  ( $V_H = 200 \text{ kts, msl}$ ),  $\chi_s = 0.5$ ,  $\gamma_{s,0} = 0.15$ ,  $\lambda_0 = 9$ .

The mean square error between the calculated mass of the variable section wing and the statistical estimations is about 12 % ( $6 \leq \lambda_0 \leq 16$ ).

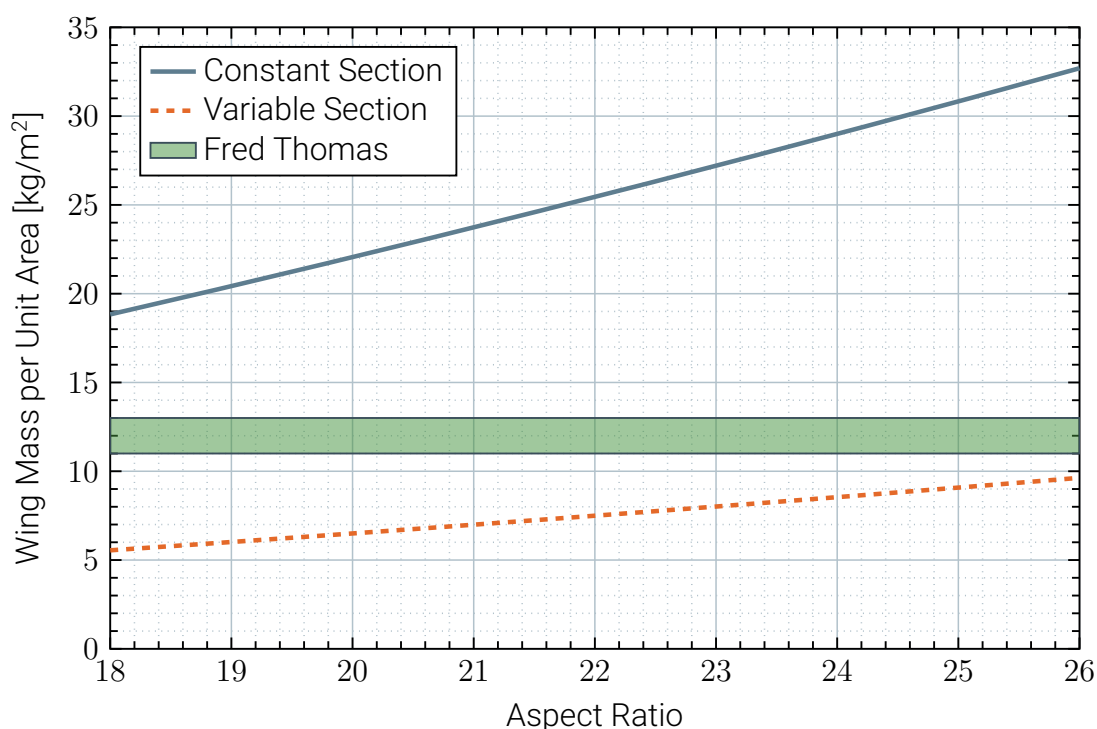


Figure 5.8: Wing mass comparison between the typical region occupied by sailplanes (i.e. high aspect ratio wings) and the proposed analytical model.

### Sailplanes

The results of this novel approach are compared with statistical estimation of wing masses of sailplanes, in order to validate the methodology also for high aspect ratio wings. Accordingly to [68], a reasonable estimation of the wing weight of a sailplane depends only on the wing area (this is better explained in the book), so in Figure 5.8 the comparison is made on wing mass per unit area of the wing.

The parameters involved in graphs of Figure 5.8 are: ultimate load factor  $n_{ult} = 1.5$ ,  $n_{max} = 6$ , maximum take off mass  $m_{TO} = 600$  kg, thickness-to-chord ratio  $(t/c) = 0.12$ , wing area  $S = 17$  m<sup>2</sup>, aluminium alloy ( $\rho = 2768$  kg/m<sup>3</sup>,  $\sigma_{max} = \sigma_{lim}/1.5 = 170$  MPa).

It can be seen that the analytical model produces results fitting well within statistical data. The mean square error between the wing mass per unit area (case with variable section) and the center of the region is about 7 % ( $18 \leq \lambda_0 \leq 26$ ).

### Cessna Method

Unfortunately, there are not many wing mass statistical equations specific for strut braced wings and it has not been possible to find reliable and complete data for some aeroplanes. Roskam [22] presents a statistical equation from Torenbeek for cantilever wings and he suggests to remove 30 % in case of strut braced wing. Articles concerning the TBW (cited and discussed in Chapter 2) indicate a reduction of about 20 % of the wing weight compared to an equivalent cantilever wing.

Again Roskam [22] presents two equations under the name "Cessna Method" valid for small, relatively low performance General Aviation (GA) airplanes with maximum speeds below 200 kts. One is for cantilever wing and the other is for strut

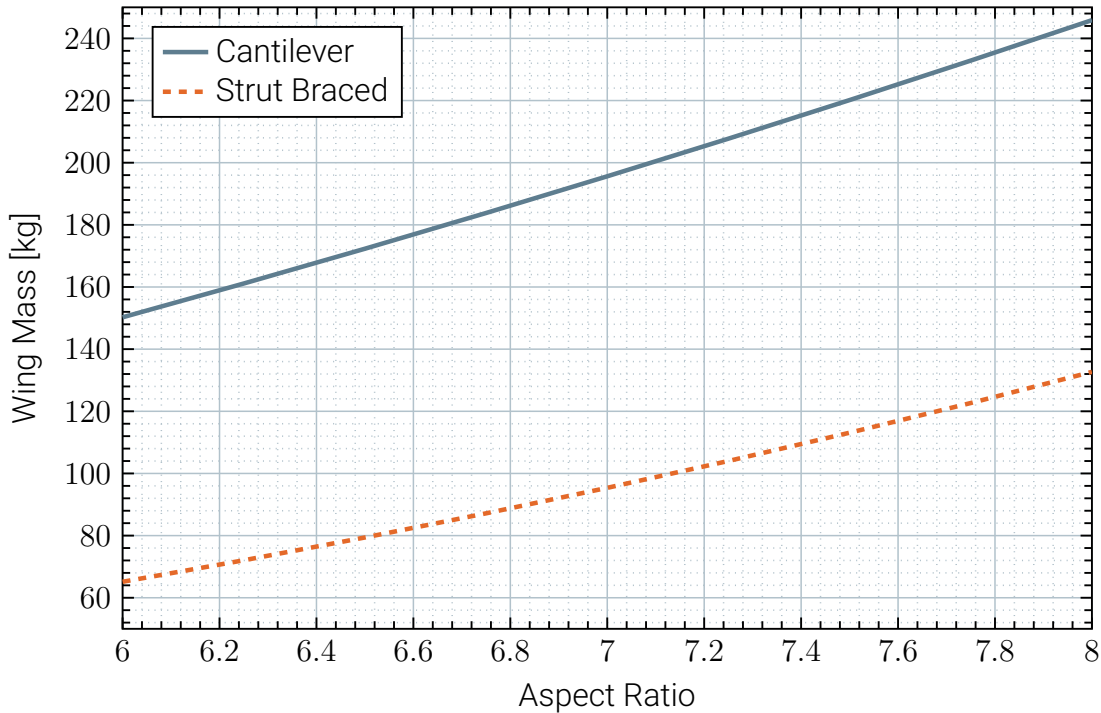


Figure 5.9: Mass of cantilever wing and strut braced wing calculated with statistical equations from Cessna Method.

braced wing. He warns that this last equation must be used with caution because it does not take into account aircraft weight. However, he does not specify any limits for the variables involved. Limit values have been determined consistently with some of the most famous Cessna aircraft, namely the Cessna 120/140, 172 Skyhawk, 185 Skywagon and 208 Caravan. For sake of completeness, these equations are printed in Appendix A.

In Figure 5.9 these two formulas have been compared for a range of aspect ratios. The parameters involved are: ultimate load factor  $n_{ult} = 1.5$   $n_{max} = 6$ , maximum take off mass  $W_{TO} = 1520$  kg, wing area  $S = 16.5$  m<sup>2</sup>.

It can be seen that the strut braced wing is estimated to be about 50 % lighter than the correspondent cantilever wing, which is consistent with the results coming from the method developed.

The results of the strut braced formula from Cessna Method have been compared with the equation from the analytical model. The strut breakpoint location has been set to  $\chi_s = 0.3$  after some tests and looking at some Cessna aircraft. Figure 5.10 shows this comparison, the parameters involved are: ultimate load factor  $n_{ult} = 1.5$   $n_{max} = 6$ , maximum take off mass  $W_{TO} = 1520$  kg, wing area  $S = 16.5$  m<sup>2</sup>, thickness-to-chord ratio  $(t/c) = 0.12$ , aluminium alloy ( $\rho = 2768$  kg/m<sup>3</sup>,  $\sigma_{max} = \sigma_{lim}/1.5 = 170$  MPa),  $\chi_s = 0.3$ ,  $\gamma_{s,0} = 0.15$ ,  $\lambda_0 = 9$ .

It can be seen that statistical estimation agrees quite well with the results for a constant section wing, which seems reasonable considering that this type of aircraft probably does not justify a significant structural optimization. The mean square error between the wing mass (constant section) and the statistical equation is about 6.5 % ( $6 \leq \lambda_0 \leq 8$ ).

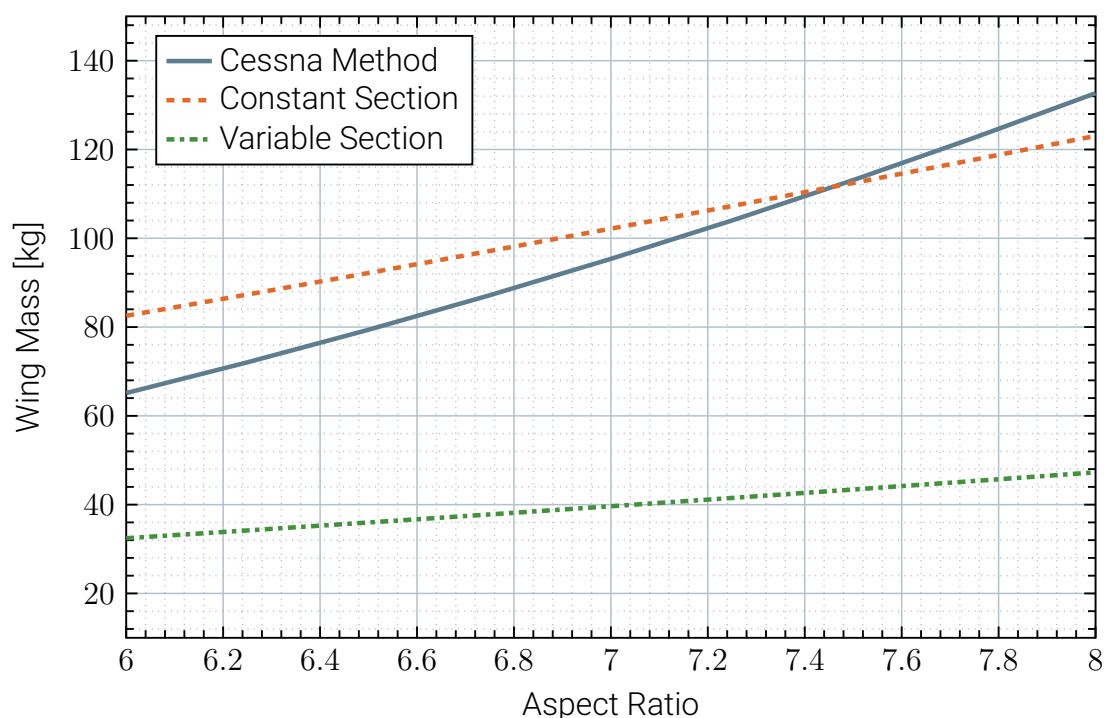


Figure 5.10: Strut braced wing mass comparison between Cessna Method and the analytical model.

### Literature about TBW

In previous validations, it has been noted that the statistical mass of a wing is usually somewhere in-between the estimated mass of a variable section wing and that of a constant section wing. Ideally, if the structure of a wing has been highly optimized then it would have a mass closer to that of a variable section wing, in which each section is sized to reach the maximum allowed stress. On the contrary, the most simple wing structure would have a constant section sized to reach the maximum allowed stress at the most loaded section.

This thinking inspired the definition of a coefficient  $\kappa_{opt}$  (already presented with equation 5.2) with values spanning range 0 to 1, expressing the *level of structural optimization* that the wing has been subjected to.

The data presented in [33], [32] and [69] are used to estimate strut braced wing masses and the results have been compared with those found in the correspondent articles. This is shown in Table 5.1.

It is interesting to look at the structural optimization level  $\kappa_{opt}$  computed for those cases, it does exceed 82 % and it reaches higher values in heavier aircraft. In most of the analyzed cases it exhibits a predictable behaviour, for example: considering the wings of sailplanes as shown in Figure 5.8, they feature a generally high structural optimization level, where designs characterized by an extreme aspect ratio demand the highest optimization effort.

<b>Name</b>	<b>Unit</b>	From [32]	From [33]	From [69]	From [12]
$m_{MTO}$	kg	239000	28740	228990	74322
$S$	m <sup>2</sup>	500	69.3	393.7	164.2
$(t/c)$	-	0.09*	0.09*	0.0914	0.1075
$\lambda$	-	15.5	20	11.1	23.087
$\lambda_0$	-	9*	10.8	11.1	11.017
$n_{\max}$	-	2.5	2.5	2.5	2.5*
$\chi_s$	-	0.43	0.6	0.6872	0.4603
$\gamma_{s,0}$	-	0.15*	0.15*	0.15*	0.15*
$\sigma_{\max}$	MPa	383	250*	250*	250*
$\rho$	kg/m <sup>3</sup>	2883	2700*	2700*	2700*
$m_{art}$	kg	48000	3610	28576	17961
$m_{\min}$	kg	36360	2458	28376	12100
$m_{\max}$	kg	98572	4666	29470	33767
$\kappa_{opt}$	-	0.8129	0.4783	0.8168	0.7295

Table 5.1: Data and results from various articles compared to those found applying the analytical method developed in this report. Data with \* have been assumed.

## 6. Quantitative Selection

So far, various innovative technologies have been analyzed, retrieving all the knowledge required to smartly combine them in a set of appealing configurations. These alternatives then faced a first quantitative selection. In this chapter, the shortlisted are sized employing the methodology already discussed in Chapter 5, and aiming to establish which one is the most suitable configuration that fulfill the UNIFIER19 design requirements.

### 6.1. Input Data

In this section the main input parameters required by the sizing tools are discussed. Some secondary settings are not presented as they are not specific to this project, one of these additional settings that played a role in the mission definition is the *energy management strategy*.

The HE architecture gives increased design flexibility by means of an additional degree of freedom, that is the ability to push and draw energy to and from the batteries during different flight phases according to a prescribed energy management strategy, thus leading to different sizing of powerplant components. The strategy chosen for the UNIFIER19 mission stands on the main concept of using batteries to deliver the excess power with respect to the cruise level. Consequently the PGS is sized to provide cruise power. As such, the battery charge is consumed during the take off and the climb stages of flight, and smartly recharged during descent or other flight phases, as needed to ensure safety while enhancing fuel efficiency and reducing noise propagation to the nearby communities. Peculiarly to this project, safety is guaranteed by approaching with enough battery charge to allow an emergency climb in case of balked landing; noise is reduced by working only on battery below a threshold altitude (in case of THE propulsion); and efficiency is enhanced by maximizing battery recharging during turnaround times in case of LH2 system, so that hydrogen boil-off is exploited and tank venting is minimized (more in Section 6.2).

Quantity	Units	Mission Review		
		A	B	C
Crew Personnel	-		1*	
Passengers/Cargo	kg		2280**	
Runway Length	m		800	
Cruise Speed	kn		150	
Diversion	km		100	
Loiter	min		45	
Turnaround	min		30	
Hop Range	km	600	250	350
Number of Hops	-	1	4	6

\*. Ready for autonomous or remotely-aided flight.

\*\* . 19 PAX, each one considered as 100 kg plus other 20 kg of checked luggage.

Table 6.1: Mission requirements during various phases of the design.

### 6.1.1. Mission Requirements

The design requirements, particularly mission requirements, stem out from market studies conducted in an earlier stage of the project and presented in [4]. The commuter aircraft of UNIFIER19 project should be able to operate also on secondary airfields with short and possibly snowy or frozen grass runways, and without relying on ground services such as tank refuelling or battery recharging. This last is enabled by the multihops mission capability, that consist in performing a number of small routes among rural aerodromes, starting and ending on a serviced airport.

In the market studies [4], they analyzed the current ground transportation network and predicted the population that would appreciate a time benefit from the new miniliner service over the usual means of transportation, so to extract the optimal mission characteristics that realize such service. They spotted a key dependency with the hop range, cruise speed and minimum runway length. In particular, shorter runways, higher cruise speeds and longer route distances help catching a wider number of citizens. Based on these results, a convenient trade-off between the aircraft performance and the caught passenger traffic has been defined with a 800 m long runway, a hop distance of about 250-350 km and a cruise speed of about 150 kn. The aircraft should be able to perform a diversion to a nearby airfield, to ensure a safety and conservative mission profile that could be actually applied in practice. It stems from the market study that the majority of airfields offer an alternate landing site within 100 km.

These requirements remained unchanged in the course of the conceptual sizing phase, except for the number of hops and their ranges, that have been subjected to optimization through multiple iterations, where each alternative was exploited at best, leading to further mission adjustments. This highlights the inherent coupling between mission and vehicle performance, the importance of attaining successful commercial operations drives both the selection of proper aircraft technologies and the enhancement of mission requirements. Table 6.1 collects the main mission parameters throughout the various steps of the process.

The aircraft should be CS-23 compliant [70], the most relevant requirements



from this regulation have been considered and imposed in the sizing process, despite they're not explicitly mentioned here. The same apply to other minor requirements, such as the rate of climb and rate of descent that are selected with consideration related to the passenger comfort, or the cruise altitude that has been selected to allow a practical duration of the cruise phase.

Initially the THE solutions were explored, they resulted particularly heavy and it has been necessary to set a range of 600 km for a single hop mission to comply with CS-23 mass limit of 8618 kg (see 6.2).

The exploration of GH2 fuel cell power train enabled a first range increase to 1000 km, or about four hops of 250 km each.

In the end, the maximum benefit has been found for LH2 fuel cell propulsion, that proved the feasibility of reaching up to 3000 km range on a single hop mission. Considering the hydrogen venting on turnaround and some safety design margin, the final mission consist of six hops of 350 km each.

### 6.1.2. Baseline Aircraft

An existing aeroplane, the Dornier 228NG, has been used as a reference to maximize the reliability of the results. This aircraft represents an excellent starting point in terms of performance and design for an advanced commuter like UNIFIER19, in fact it has been chosen for a retrofit within a similar work supervised by DLR (see Section 2.6). The 228NG has been used for the validation of the sizing tools employed for this project, therefore the relevant input parameter to Hyperion and Titan represent a robust basis, capable of facilitating the achievement of a commercially feasible design.

It is a twin turboprop high wing aircraft with retractable landing gear, it hosts 19 passengers reaching a MTOM of 6575 kg. Its range is limited to about 344 km when loaded with 1960 kg of payload but it has STOL capability as proved by the 792 m take off run. Still, the cabin features a two seats per row layout resulting in 1,35m x 1,55m x 14.7m cabin dimensions [71], which means that LD3 shipping containers cannot be loaded. The LD3 container is the smallest intended for standard aviation with its dimensions of 1,534m x 1,626m x 2,007m, and the UNIFIER19 airplane should be able to accommodate three of them in freighter configuration as per cargo requirement.

The cabin layout that permit to satisfy such a condition on the cargo bay is that adopted by the Cessna 408 SkyCourier, where the seats are arranged three per row (see Figure 6.1). The SkyCourier is a vehicle still in the development stage (firstly flown in May 2020), which shares many attributes with the 228NG, and many mission requirements of UNIFIER19: it is intended to be a completely new 19-PAX aircraft with twin turboprop mounted on its high wing, purposely designed to operate at high utilization rate with maximum efficiency. In fact, it minimizes turnaround time through fast refuelling, easy boarding, and easy loading enabled by a built-in roller system and a wide passenger/cargo door.

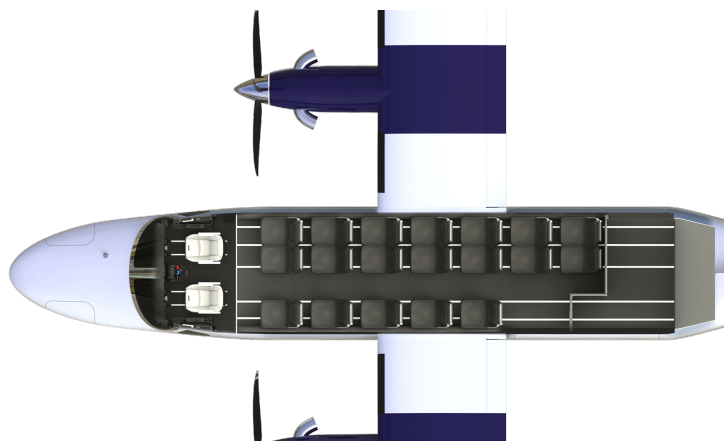


Figure 6.1: Cabin layout of the Cessna 408 SkyCourier [72].

Parameter	Units	Technological Years			
		2020	2025	2030	2035
Battery Specific Energy	Wh/kg	210	260	304	350
Battery Specific Power	W/kg	1365	1670	1970	2275
Battery Volumetric Density	Wh/l	490	600	710	817
Fuel Cell Specific Power	W/kg	800	2130	3460	4800
Electric Motor Specific Power	W/kg	5750	7533	9317	11100
Gravimetric Index (GH <sub>2</sub> )	%	20	25	30	35

Table 6.2: Parameters defining the technological level expected for 2025 (interpolation between 2020 and 2035 of data from [35]).

### 6.1.3. Technology Level

The time scale of an aeronautical project is usually quite large, the entry into service of an aircraft comes many years after the beginning of the conceptual design, and during those years the technical progress proceeds relentless. This is specially likely for an innovative project such as the UNIFIER19, thus it is of paramount importance to carefully estimate the expected performance growth of the technologies involved in the project, exploiting at best their future benefit.

The market inclusion of UNIFIER19 should happen as soon as possible, considering the time frame of the detailed design it has been decided that a technological level for this aircraft will be that of year 2025. Table 6.2 lists the main performance parameters that depends on the technological evolution, determined by interpolation of the current ones (2020) and those estimated in literature for the year 2035 [35].

---

## 6.2. Results

This stage of the UNIFIER19 project is still in progress. However, various configurations have been sized and compared. The design mission is still being optimized and the update of the sizing tools is still ongoing. Despite all this, a set of milestones have been already achieved, particularly:

- the concurrent design loop is at its last iterations and the candidate airplanes are converging to stable solutions.
- thermal hybrid electric architecture has been excluded in favour of a fuel cells based architecture.
- storage of gaseous hydrogen has been excluded in favour of a liquid hydrogen storage system.
- strut braced wing configuration (C7) may be excluded as it presents minimal or even negative improvements with respect to the baseline (C0).
- the most ready alternative (C6) has been already delivered to PVS for assessment.
- configurations C2 and C3 look very promising and they are close to be deliverable too.

At the beginning of the sizing stage only the first five candidates of Table 4.5 have been considered, namely C3, C12, C2, C7 and C15. Comparing the results the similarity among configurations C7, C15 and C12 showed the greatest potential, prompting a review of the candidate configurations as already discussed in Chapter 4. This comes from the inherent iterative nature of the design process, where the presence of nested loops may require some steps to partially overlap (similarly to what happened between Chapter 3 and 4 with the addition of two special configurations during the initial selection process).

In the rest of this section an overview of the intermediate numerical results is given.

### Thermal Hybrid Electric

The quantitative selection started with the analysis of the most ready hybrid-electric architecture, that is the thermal hybrid electric. This architecture provides benefits both in terms of acoustic and chemical emissions, however its high weight dramatically penalizes performance (see Table 6.3). In fact, despite a sizing cruise range of only 600 km, the MTOMs of all the candidates exceed the CS-23 limit of 8618 kg. Such a low cruise range limits the potential for commercial successful operations.

<b>Label</b>	<b>MTOM</b> kg	<b>Empty</b> kg	<b>Battery</b> kg	<b>Fuel</b> kg	<b>Power*</b> kW	<b>Wing Area</b> m <sup>2</sup>
C2	9998	5456	1231	832	1958	49
C3	10188	5820	1211	779	1904	50
C7	10184	5664	1371	670	2177	50

\*. Maximum continuous at propeller(s) shaft.

Table 6.3: Main sizing results with THE architecture.

<b>Label</b>	<b>MTOM</b> kg	<b>Empty</b> kg	<b>Battery</b> kg	<b>Fuel</b> kg	<b>Power*</b> kW	<b>Wing Area</b> m <sup>2</sup>
C2	8223	4981	684	113	1607	40.3
C3	8423	5184	654	105	1574	41.3
C7	8633	5222	836	94	1845	42.3

\*. Maximum continuous at propeller(s) shaft.

Table 6.4: Main sizing results with fuel cells based HE architecture and GH2.

## Gaseous Hydrogen

The GH2 fuel cells architecture offers much better results with respect to the THE one, see Table 6.4. The sizing cruise range is still set to 600 km for these solutions but now, the new powertrain option pulls the MTOM down below the CS-23 limit. A little margin of improvement has been identified after some analysis and refinements of design settings, however it seems impossible to attain more than two hops without refuelling.

## Liquid Hydrogen

Liquid hydrogen storage enables full operational potential to the UNIFIER19 service. In fact, right from the firsts sizings it appeared possible to increase the number of hops considerably. Initially only four hops of 250 km each were considered, then the number of hops has been increased to six and the range of each hop has been increased to 350 km (Table 6.5). This rather long mission lasts more than 11 hours, allowing service at full load throughout the entire daylight without refuelling (see Figure 6.3). Such great operational capabilities are ensured with a reasonable margin from the CS-23 mass limit (Table 6.5).

In multi-hops sizing the diversion and loiter have been placed only at the first hop because it is the most penalizing as the aircraft flies with the greatest mass. However, it must be pointed out that this is a *design mission* and so, it is intended only to provide sizing constraints. In a *realistic operative* scenario the mission would be degraded or aborted as the aircraft must be able to perform a diversion and/or a loiter always until the last landing for safety reasons.

Liquid hydrogen needs to be maintained at a cryogenic temperature, otherwise it would boil off causing tank pressure to increase. The LH2 tank is not sized to

<b>Label</b>	<b>MTOM</b> kg	<b>Empty</b> kg	<b>Battery</b> kg	<b>Fuel</b> kg	<b>Power*</b> kW	<b>Wing Area</b> m <sup>2</sup>
<b>C6</b>	7954	4615	586	376	1188	39
<b>C2</b>	7843	4356	743	369	1378	39.9
<b>C3</b>	7392	4148	521	350	1082	37
<b>C7</b>	8223	4863	547	433	1228	40.3
<b>C0</b>	8212	4715	719	405	1397	41.2
<b>REF**</b>	8733	4904	0	1501	1866	44

\*. Maximum continuous at propeller(s) shaft.

\*\*.. Sized for a range of 1600 km to comply with MTOM limit of CS-23.

Table 6.5: Main sizing results with fuel cells based HE architecture and LH2.

withstand much high pressure, thus the hydrogen must be vented in such an eventuality. During normal flight the evaporated hydrogen is consumed by fuel cells, indeed fuel demand is usually such that additional heat is required other than that naturally received from tank walls in order to enforce hydrogen boil off.

During turnaround time the fuel demand drops substantially and venting is likely required, causing inefficiencies and undesirable emissions. A cooling system to keep hydrogen in liquid form would be too big and heavy to be included onboard favourably, but when ground infrastructure is available tank venting may be prevented relying on a ground fuel cooling system. Nevertheless, this should not be a big deal for UNIFIER19 as its operating philosophy is to be "as easy as a bus", thus embarking and disembarking procedures would be especially fast yielding to short turnaround.

Figure 6.2 indicates the travelled distance and the true airspeed during the sizing mission. In particular, these comes from the sizing results of configuration C6. The loiter and diversion are clearly visible at the end of the first hop, the turnaround phases are also distinguishable by looking at airspeed that drops to zero.

Figure 6.3 depicts the altitude during the sizing mission, together with the level of throttle, battery charge and remaining fuel. It can be noticed that fuel level decreases also during turnaround time, when the fuel cells throttle is set to zero. This is the consequence of venting the hydrogen tank, and it is more significant in the lasts hops than in the firsts.

Similar graphs have been obtained for the other configurations, with differences that are difficult to appreciate as MTOM changes in the order of a few hundreds of kg among alternatives (less than 7%).

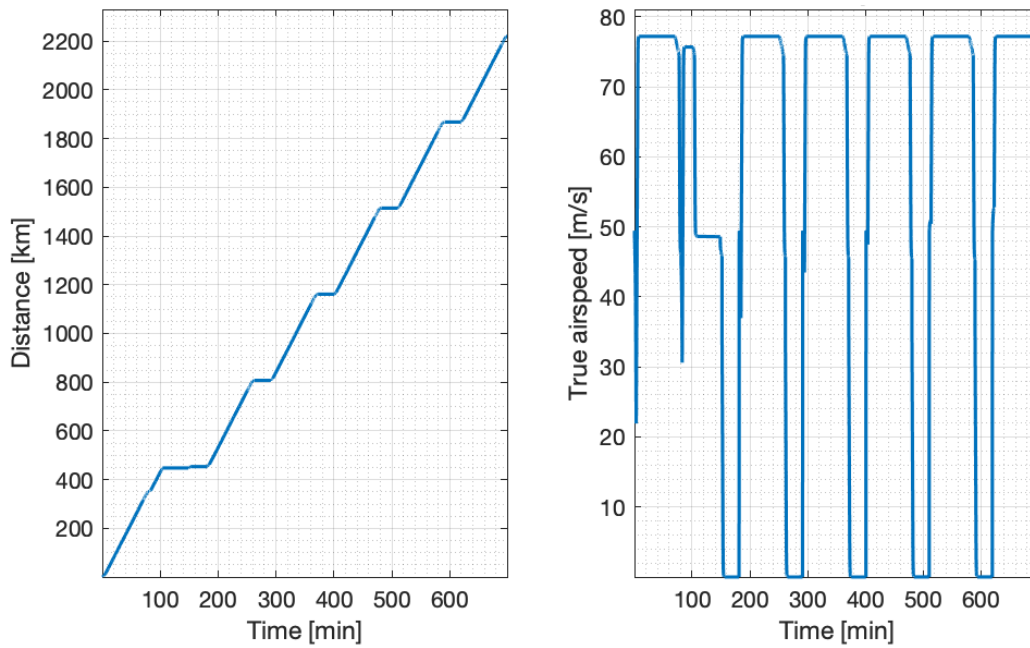


Figure 6.2: Distance and true airspeed over the mission (C6).

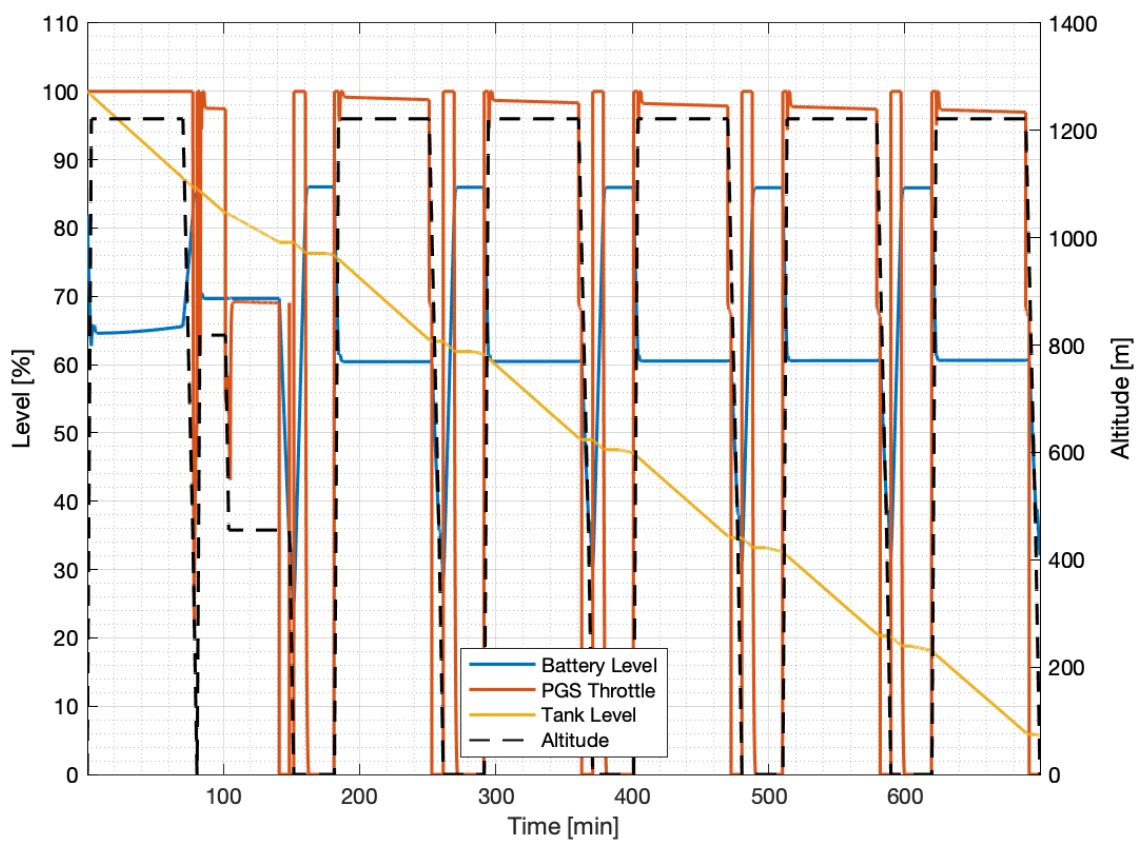


Figure 6.3: Altitude, throttle, fuel and battery levels along the mission (C6).

---

## 6.3. Final Assessment

As anticipated, the assessment of the proposed configurations is still ongoing at the moment of writing this report.

The configuration selection is a very complex problem that cannot ignore an in-depth cost analysis and feasibility assessment, which are outside of the scope of the present thesis work. In fact, such a delicate task is assigned to a well experienced partner, the airplane manufacturer Pipistrel Vertical Solution (PVS). The role of Politecnico di Milano in this process is focused on the identification of alternatives and the subsequent estimation of their environmental impact. Throughout this work, a great amount of possibilities have been explored with the purpose of detecting the best combinations of technologies that ensure a great potential for the commercial future of the UNIFIER19 project.

The quantitative selection carried out in this work is based on the amount of energy consumed per passenger and per kilometer. In fact, the European Union decision makers are paying much attention to the overall efficiency of aviation, independently from the source of energy employed, be it hydrogen or batteries or kerosene. Such a decision criterion may look like an over-simplification of the decision process, but it relies on a long-term thinking approach that focuses on the achievement of the European vision "*Flightpath 2050*". In practice, a number of regulations are expected for the near future aiming at enforcing efficiency and sustainability, especially in transportation and even more in aviation. Therefore, it is extremely likely that this will be the main driving requirement also in a comprehensive and structured selection process.

Based on the sizings presented in the previous section, configuration C3 attains the best performance in this regard. In fact, it stands out for the low values of both fuel mass and battery mass. However, it must be noted that configuration C3 is currently the most immature among the presented alternatives, as the prediction concerning the amount of laminar boundary layer attainable over the fuselage has not yet been validated. On the contrary, configuration C6 represents the most reliable solution at this stage, as it already underwent a thorough assessment.

A conceptual representation of configuration C6 is given in Figure 6.4, where its main systems are highlighted with different colours: electric motors are colored in light green and they are placed close to correspondent propeller; passenger seats are shown in yellow; battery pack is placed in the central part of the wing and it is highlighted in green; the pink box in the tail cone symbolizes the PGS; the cylindrical blue shape behind the cabin is the LH2 tank; the cargo is barely visible in dark green at the end of the passenger cabin.

The same subsystem placement is applied to the other configurations.

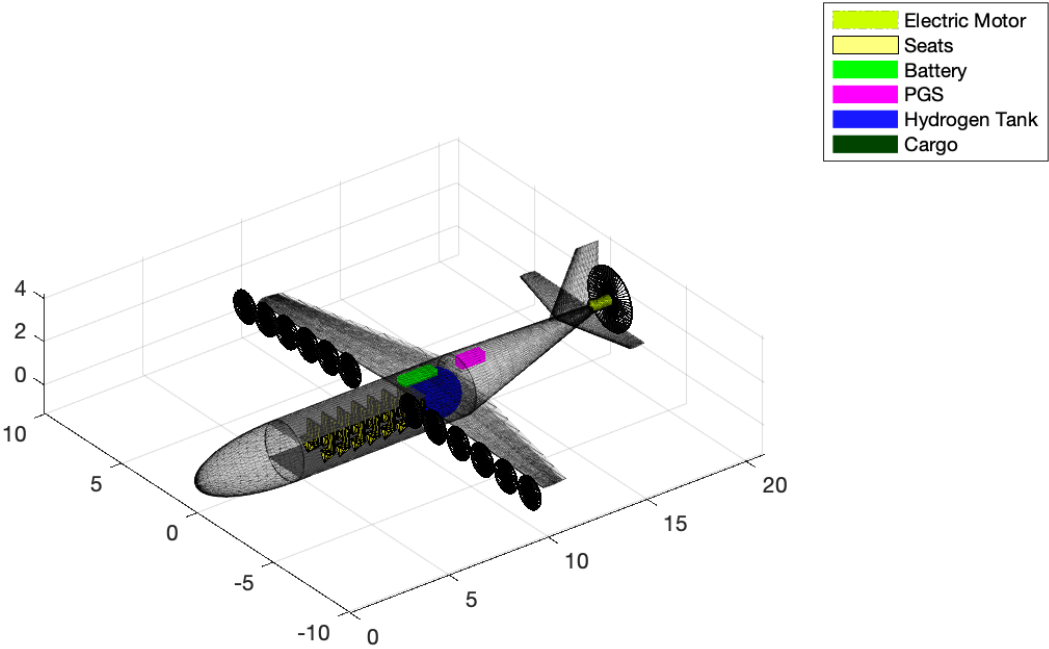


Figure 6.4: Schematic representation of the candidate configuration (C6).



## 7. Conclusion

In the present work, the design space for the candidate configurations of a near-zero emission commuter aircraft, targeted in the UNIFIER19 project, has been thoroughly explored. This led to the creation of a set of candidate airplanes suited for the intended mission, including more than 45 possibilities that have been later assessed and down-selected.

An initial selection has been carried out to reduce the list of candidates to a practical number that permits their refinement and accurate assessment. This selection has been based on a few criteria that grant minimal loss of opportunities in reaching the design goals. Also, a specific selection tool has been implemented through spreadsheets based on the AHP method. This allowed to perform and aggregate different evaluations of the configurations with respect to a set of selection criteria. These criteria has been carefully chosen to facilitate judgement of the key aspects that drive the project.

New design options have been investigated, modelled and implemented in the design tools. Particularly, this document includes the work carried out on the analytical modelling of a strut braced wing suited for aircraft preliminary sizing purposes. The equations have been derived and extensively tested for various aircraft categories (commercial airplanes, general aviation and even sailplanes).

The most promising alternatives have been sized with tools developed within the FMSlab research group during previous activities and further refined during the present work. The results obtained allowed the selection of a powertrain architecture, as well as a quantitative ranking based on emissions considerations. The configurations have been sized with either a thermal hybrid-electric architecture or a fuel-cell-based hybrid-electric architecture, with either gaseous or liquid hydrogen on-board storage systems. The best solution in term of emissions is found in the liquid hydrogen fuel-cell-based option.

A traditional turboprop aircraft has been considered and it has been demonstrated that it is not able to achieve the same mission capability within the CS-23 category limits.

An aircraft with classical layout (i.e. aft tail and twin wing-mounted propellers) and liquid hydrogen drivetrain has been considered as a baseline. The proposed configurations generally show better performance with respect to such baseline, except for configuration C7, which shows slightly worse performance. The reason for that may be due to the short cruise phases that prevent exploiting the benefit on induced drag at best. C7 may have some margin of improvement by adjusting mission definition in terms of cruise altitude and speed, but it is unlikely that it would overcome the other competitors.

Configuration C6 is currently undergoing a thorough review in the final phase

of the WP2 activities of the UNIFIER19 project to assess its general feasibility and cost efficiency.

### **Critical Analysis and Recommendations**

Based on my experience in this project, would like to offer some considerations for the improvement of the design space exploration process applicable to possible future activities.

I recommend to rely more on hand-drawing and brainstorming to generate a list of alternatives. Indeed, the systematic approach initially adopted in this work led to a great amount of unfeasible configurations that have been later removed, while the recommended approach resulted in strong configurations, such as C2 and C3 that are currently considered viable options for UNIFIER19.

I recommend to adopt a simpler method such as the Pugh's Matrix to further reduce the number of configurations before applying the AHP method (10 elements would be enough in my opinion, 15 elements proved to be too many). Moreover, it is important not to hurry towards the final qualitative selection, but to take time to analyze the scoring and the effect of different opinions and/or thinking of multiple experts. Finally, it is advisable to cross-check the results with other selection approaches, such as the Pugh's method. In this process, it may be useful to combine also different selection criteria, and to have preliminary numerical results to better judge a solution over the others.

For the sake of the effectiveness of the final assessment process in the UNIFIER19 project, I recommend to establish a shared repository among project partners to permit real-time access to the latest version of software tools, documents and notifications of issues.

### **Future Works**

The spreadsheet tool developed in Chapter 4 will be enhanced with a greater level of automatization that will fasten its application to other problems. Tables will be automatically generated and initialized according to the given set of criteria and alternatives.

The strut braced wing model developed in Chapter 5 will be further analyzed and better implemented to deliver more accurate and reliable results.

The energy management strategy will be improved to ensure higher safety while limiting inefficiencies that occur during turnaround, as discussed in Chapter 6.

The possible benefits of the VIW mentioned in Chapter 2 will be investigated. For instance, the operating strategies that this technology enables such as adapting the incidence to flight conditions to reduce trim and fuselage drag. Particularly interesting effects may raise when coupled with DEP thanks to thrust vectoring that may further enhance landing capability.

The sizings of configurations C2, C3 and C7 will be refined and possibly delivered to partner for further assessments. The effect of exploiting propulsion controls on configuration C2 will be investigated. The drag advantages promised by configuration C3 will be better analyzed and validated. Finally, the mission profile for configuration C7 will be modified searching for its best commercial role.

## Bibliography

- [1] Hydrogen-powered aviation, A Fact-Based Study of Hydrogen Technology Economics, and Climate Impact by 2050, Clean Sky 2 JU and FCH2 JU, ISBN 978-92-9246-342-7, doi:10.2843/471510, EG-04-20-214-EN-N, 2020.
- [2] P. Argüelles, J. Lumsden, M. Bischoff, D. Ranque, P. Busquin, S. Rasmussen, B. A. C. Droste, P. Reutlinger, R. Evans, R. Robins, W. Kröll, H. Terho, J. L. Lagardère, A. Wittlöv, A. Lina, European Aeronautics: a Vision for 2020, Meeting Society's Needs and Winning Global Leadership, European Commission, ISBN 92-894-0559-7, 2001.
- [3] European Commission, Flightpath 2050, Europe's Vision for Aviation, Maintaining Global Leadership & Serving Society's Needs, Report of the High Level Group on Aviation Research, Directorate-General for Research and Innovation, Directorate-General for Mobility and Transport, ISBN 978-92-79-19724-6, DOI 10.27777/50266, 2011.
- [4] L. Trainelli, C. E. D. Riboldi, A. Rolando, F. Salucci, F. Oliviero, J. Pirnar, T. Koopman, A. Znidar, D1.2.: The Design Framework for an NZE 19-Seater, UNIFIER19, 2020.
- [5] M. M. D'Angelo, J. Gallman, V. Johnson, E. Garcia, J. Tai and R. Young, N+3 Small Commercial Efficient and Quiet Transportation for Year 2030-2035, NASA, CR-2010-216691, 2010.
- [6] Website of the UNIFIER19 project, <https://www.unifier19.eu>, Last check: March 2, 2021.
- [7] L. Trainelli, C. E. D. Riboldi, F. Salucci, A. Rolando, A General Preliminary Sizing Procedure for Pure-Electric and Hybrid-Electric Airplanes, Department of Aerospace Science and Technology, Politecnico di Milano, Aerospace Europe Conference 2020, 2020.
- [8] A. E. Briz and I. Raimo, A Framework for Hybrid-Electric Aircraft Preliminary Sizing, Master Thesis, Politecnico di Milano, Academic Year 2019-2020.
- [9] Website page of NASA, release C08-060 "NASA Awards Future Vehicle Aircraft Research Contracts" of October 6, 2008, [http://www.nasa.gov/home/hqnews/2008/oct/HQ\\_C08-060\\_ARMD\\_contracts.html](http://www.nasa.gov/home/hqnews/2008/oct/HQ_C08-060_ARMD_contracts.html), Last check: March 7, 2021.
- [10] E. M. Greitzer, P. A. Bonnefoy, E. De la Rosa Blanco, C. S. Dorbian, M. Drela, D. K. Hall, R. J. Hansman, J. I. Hileman, R. H. Liebeck, J. Lovegren, P. Mody, J. A. Pertuze, S. Sato, Z. S. Spakovszky, C. S. Tan, J. S. Hollman, J. E. Duda, N.

Fitzgerald, J. Houghton, J. L. Kerrebrock, G. F. Kiwada, D. Kordonowy, J. C. Parish, J. Tylko, E. A. Wen and W. K. Lord, N+3 Aircraft Concept Designs and Trade Studies, Final Report, Volume 1, NASA/CR-2010-216794/VOL1, 2010.

- [11] Website of NASA *Airplane Concepts*, <https://www1.grc.nasa.gov/aeronautics/hep/airplane-concepts/>, Last check: March 6, 2021.
- [12] M. K. Bradley and C. K. Droney, Subsonic Ultra Green Aircraft Research: Phase I Final Report, NASA/CR-2011-216847, 2011.
- [13] S. W. Ashcraft, A. S. Padron, K. A. Pascioni, G. W. Stout Jr. and Dennis L. Huff, Review of Propulsion Technologies for N+3 Subsonic Vehicle Concepts, NASA/TM-2011-217239, 2011.
- [14] IATA (International Air Transport Association), Aircraft Technology Roadmap to 2050, 2009.
- [15] Website of Airbus ZEROe Project, <https://www.airbus.com/innovation/zero-emission/hydrogen/zeroe.html>, Last check: March 6, 2021.
- [16] IATA (International Air Transport Association), Technology Roadmap for Environmental Improvement, Fact Sheet, 2020.
- [17] Website of Pipistrel Velis Electro, <https://www.pipistrel-aircraft.com/aircraft/electric-flight/velis-electro-easa-tc/>, Last check: March 6, 2021.
- [18] Website of the eCaravan Project on AeroTEC, <https://www.aerotec.com/magnix-and-aerotec-announce-successful-first-flight-of-the-worlds-largest-all-electric-aircraft/>, Last check: March 6, 2021.
- [19] S. Honkala, M. Hamalainen, M. Salonen, Comparison Of Four Existing Concept Selection Methods, Helsinki University of Technology, Interational Conference on Engineering Design, 2007.
- [20] S. Burge, The Systems Engineering Tool Box, 2009.
- [21] T. L. Saaty, Decision Making with the Analytic Hierarchy Process, Katz Graduate School of Business, University of Pittsburgh, Int. J. Services Sciences, Vol. 1, No. 1, 2008.
- [22] J. Roskam, Airplane Design. Part V: Component Weight Estimation. Roskam Aviation and Engineering Corporation, 1985.
- [23] D. P. Raymer, J. Wilson, H. D. Perkins, A. Rizzi, M. Zhang, A. R. Puentes, Advanced Technology Subsonic Transport Study, N+3 Technologies and Design Concepts, National Aeronautics and Space Administration, NASA/TM-2011-217130, 2011.
- [24] B. Malcom and V. Roelof, Conceptual Design and Evaluation of Blended-Wing-Body Aircraft, AIAA Aerospace Sciences Meeting (210059 ed.), AIAA 2018-0522, <https://doi.org/10.2514/6.2018-0522>, 2018.

- [25] R. Vos, F. J. J. M. M. Geuskens, M. F. M. Hoogreef, A New Structural Design Concept for Blended Wing Body Cabins, AIAA 2012-1998, 53rd AIAA/ASME/ASCE/AHS/ASC Structures, Structural Dynamics and Materials Conference, DOI: 10.2514/6.2012-1998, 23-26 April 2012.
- [26] Website of NASA X-48, [https://www.nasa.gov/topics/aeronautics/features/bwb\\_main.html](https://www.nasa.gov/topics/aeronautics/features/bwb_main.html), Last check: March 7, 2021.
- [27] Website of Airbus MAVERIC, <https://www.airbus.com/newsroom/press-releases/en/2020/02/airbus-reveals-its-blended-wing-aircraft-demonstrator.html>, Last check: March 7, 2021.
- [28] L. Prandtl, Induced Drag of Multiplanes, National Advisory Committee for Aeronautics, Technical Note No. 182, Technische Berichte, Volume III, No.7, pp. 309-315, Reproduced Copy of NACA-TN-182, Reproduced for NASA by NASA Scientific and Technical Information Facility, FFNo 672 Aug 65.
- [29] A. Somerville, M. Marino, G. Baxter, G. Wild, Understanding Box Wing Aircraft: Essential Technology to Improve Sustainability in the Aviation Industry, Aviation, Volume 20(3), 129-136, ISSN 1648-7788, eISSN 1822-4180, doi:10.3846/16487788.2016.1195076, 2016.
- [30] Website of the PARSIFAL Project, <https://parsifalproject.eu>, Last check: March 16, 2021.
- [31] J. E. Guerrero, D. Maestro and A. Bottaro, Biomimetic Spiroid Winglets for Lift and Drag Control, C. R. Mecanique 340, 67-80, 2012.
- [32] O. Gur, M. Bhatia, W. H. Mason, J. A. Schetz, R. K. Kapania, T. Nam, Development of a Framework for Truss-Braced Wing Conceptual MDO, AIAA Paper 2010-2754, 6th AIAA Multidisciplinary Design Optimization Specialist Conference, April 12-15, 2010.
- [33] S. Hosseini, M. A. Vaziri-Zanjani and H. R. Ovesy, Conceptual Design and Analysis of an Affordable Truss-Braced Wing Regional Jet Aircraft, Journal of Aerospace Engineering, DOI: 10.1177/0954410020923060, 2020.
- [34] D. Verstraete, P. Hendrick, P. Pilidis and K. Ramsden, Hydrogen Fuel Tanks for Subsonic Transport Aircraft, International Journal of Hydrogen Energy 35, 2010.
- [35] L. M. C. Guevara, Liquid Hydrogen Aircraft Propulsion, Master Thesis, Politecnico di Milano, Academic Year 2019-2020.
- [36] A. M. Stoll, J. B. Bevirt, M. D. Moore, W. J. Fredericks and N. K. Borer, Drag Reduction Through Distributed Electric Propulsion, American Institute of Aeronautics and Astronautics, Aviation Technology Integration, and Operations Conference, June 16-20, 2014.
- [37] Website of NASA X-57 Project, <https://www.nasa.gov/specials/X57>, Last check March 7, 2021.
- [38] A. Matrone, Performance-Based Preliminary Sizing of Aircraft with Distributed Propulsion, Master of Science Thesis, Politecnico di Milano, Academic Year 2019/2020.

- [39] J. C. Patterson Jr. and G. R. Bartlett, Effect of a Wing-Tip Mounted Pusher Turboprop on the Aerodynamic Characteristics of a Semi-Span Wing, AIAA Paper 85-1286 (A85-39700), AIAA/SAE/ASME/ASEE 21st Joint Propulsion Conference, July 8-10, 1985.
- [40] T. Sinnige, N. van Arnhem, T. C. A. Stokkermans, G. Eitelberg and L. L. M. Veldhuis, Wingtip-Mounted Propellers: Aerodynamic Analysis of Interaction Effects and Comparison with Conventional Layout, *Journal of Aircraft*, DOI: 10.2514/1.C034978, 2018.
- [41] L. H. Smith Jr., Wake Ingestion Propulsion Benefit, Paper 91-2007, AIAA/ASME/SAE 27th Joint Propulsion Conference, June 24-27, 1991.
- [42] D. K. Hall, A. C. Huang, A. Uranga, E. M. Greitzer, M. Drela, S. Sato, Boundary Layer Ingestion Propulsion Benefit for Transport Aircraft, *Journal of Propulsion and Power*, 2017.
- [43] E. S. Hendricks, A Review of Boundary Layer Ingestion Modeling Approaches for use in Conceptual Design, NASA/TM-2018-219926, 2018.
- [44] N. Budziszewski and J. Friedrichs, Modelling of a Boundary Layer Ingesting Propulsor, *Energies* 2018, 11, 708, doi:10.3390/en11040708, 2018.
- [45] H. D. Kim, A. T. Perry and P. J. Ansell., A Review of Distributed Electric Propulsion Concepts for Air Vehicle Technology, AIAA 2018-4998, AIAA/IEEE Electric Aircraft Technologies Symposium, 2018.
- [46] F. W. Burcham Jr., J. Burken and T. A. Maine, Flight Testing a Propulsion-Controlled Aircraft Emergency Flight Control System on an F-15 Airplane, NASA Technical Memorandum 4590, 1994.
- [47] F. W. Burcham Jr., T. A. Maine, J. J. Burken and J. Bull, Using Engine Thrust for Emergency Flight Control: MD-11 and B-747 Results, NASA/TM-1998-206552, 1998.
- [48] B. J. Holmes, Flight Experiences with Laminar Flow, NASA Langley Research Center, N88-23744.
- [49] S. S. Dodbele, C. P. van Dam, P. M. H. W. Vijgen and B.J. Holmes, Shaping of Airplane Fuselages for Minimum Drag, AIAA 24th Aerospace Sciences Meeting, AIAA-86-0316, January 6-9, 1986.
- [50] M. J. Walsh, Riblets for Aircraft Skin-Friction Reduction, NASA Langley Research Center, N88-14955.
- [51] Website of the Clean Sky's Morphing Wing Project, <https://www.cleansky.eu/clean-skys-morphing-wing-project-brings-shape-shifting-capabilities-to-european-regional-aircraft>, Last check: March 15, 2021.
- [52] R. Clarke, M. J. Allen, R. P. Dibley, J. Gera and J. Hodgkinson, Flight Test of the F/A-18 Active Aeroelastic Wing Airplane, NASA/TM-2005-213664, 2005.

- [53] S. Kota and J. R. R. A. Martins, FlexFoil Shape Adaptive Control Surfaces - Flight Test and Numerical Results, 31st Congress of the International Council of the Aeronautical Sciences, September 9-14, 2018.
- [54] Website of ELICA Project on CORDIS Europa, <https://cordis.europa.eu/project/id/864551>, Last check: March 7, 2021.
- [55] Website of HECARRUS Project, <https://www.hecarrus.eu>, Last check: March 7, 2021.
- [56] Website of DLR CoCoRe Project, [https://www.dlr.de/content/en/articles/news/2020/01/20200217\\_electric-flight-from-mannheim-to-berlin-in-19-seater-aircraft.html](https://www.dlr.de/content/en/articles/news/2020/01/20200217_electric-flight-from-mannheim-to-berlin-in-19-seater-aircraft.html), Last check: March 7, 2021.
- [57] Website of MTU Aero Engine, <https://www.mtu.de/newsroom/press/latest-press-releases/press-release-detail/mtu-aero-engines-hydrogen-puts-the-future-at-our-fingertips/>, Last check: March 7, 2021.
- [58] Website of Heart Aerospace, <https://heartaerospace.com>, Last check: March 7, 2021.
- [59] Website of HyFlyer II on ZeroAvia, <https://www.zeroavia.com/press-release-hyflyer-2-grant>, Last check: March 7, 2021.
- [60] Website of HyFlyer II on EMEC, <http://www.emec.org.uk/projects/hydrogen-projects/hyflyer/>, Last check: March 7, 2021.
- [61] Website of Faradair BEHA Project, <https://www.faradair.com>, Last check: March 18, 2021.
- [62] Website of Otto Celera 500 L, <https://www.ottoaviation.com/celera-500l>, Last check: March 27, 2021.
- [63] G. J. Healy, Measurement and Analysis of Aircraft Far-Field Aerodynamic Noise, National Aeronautics and Space Administration, NASA CR-2377, 1974.
- [64] S. Stückl, J. van Toor and H. Lobentanzer, VoltAir - The All Electric Propulsion Concept Platform - A Vision for Atmospheric Friendly Flight, 28th International Congress of the Aeronautical Sciences, 2012.
- [65] D. P. Raymer, Aircraft Design: a Conceptual Approach, Sixth Edition, AIAA Education Series, ISBN 9781624104909, 2018.
- [66] V. Giavotto, Strutture Aeronautiche, CittàStudiEdizioni, Terza Edizione, 1995.
- [67] M. H. Sadraey, Aircraft Design. A Systems Engineering Approach, John Wiley & Sons, Ltd, ISBN 978-1-119-95340-1, 2013.
- [68] F. Thomas, Fundamentals of Sailplane Design. "*Grundlagen für den Entwurf von Segelflugzeugen*", Translated by Judah Milgram, College Park Pr, ISBN-10 0966955307, 1999.

- [69] F. H. Gern, A. H. Naghshineh-Pour, E. Sulaeman, and R. K. Kapania, R. T. Haftka, Flexible Wing Model for Structural Sizing and Multidisciplinary Design Optimization of a Strut-Braced Wing, AIAA-2000-1327, 41st AIAA/ASME/ASCE/AHS/ASC Structures, Structural Dynamics and Materials Meeting & Exhibit, 3-6 April 2000.
- [70] EASA (European Union Aviation Safety Agency), Certification Specifications for Normal-Category Aeroplanes (CS-23) and Acceptable Means of Compliance and Guidance Material to the Certification Specification for Normal-Category Aeroplanes (AMC & GM to CS-23), CS-23 Amendment 5/ AMC & GM to CS-23 Issue 3, 24 June 2020.
- [71] Dornier 228, Advanced Commuter (AC), Fact & Figures, RUAG Aerospace Services GmbH, Website: <https://ruag-international.picturepark.com/v/SQmZwhjP/>, Last check: March 21, 2021.
- [72] Website of Cessna 408 SkyCourier, <https://cessna.txtav.com/en/turboprop/skycourier>, Last check: March 21, 2021.
- [73] V. Pajno, Sailplanes Design. A guide for students and designers. From drafting to flight test, IBN Editore, ISBN 9788875650926, 2010.



## A. Strut Braced Wing Analytical Modeling

The candidate configuration "C7" includes the high aspect ratio TBW technology. In order to be able to quantitatively catch the effects of this technology it has become necessary to model it and integrate it inside our sizing tools. In other words, it has been necessary to estimate its impact on mass and drag of the airplane.

The approach followed for these estimations has been already discussed in Section 5.3, together with its validation and its results. This appendix contains many details excluded in that section to preserve the flux of the main topic of this document, that is the conceptual design of UNIFIER19 aircraft.

In Section A.1 the load distributions and the section properties are discussed, then the cantilever wing and the strut braced wing models are developed, respectively in Section A.2 and A.3. It follows a brief comparison between the results from the two models (Section A.4) and a comparison with data gathered from literature aimed to validate the approach followed (Section A.5).

Finally, in Section A.6, other secondary but useful information are presented.

### A.1. Problem Setup

This section treats various topic that are common to both wing layouts, or that are useful for comparing them.

#### A.1.1. Load Distributions

The ideal lift distribution on a wing is elliptical, this minimize induced drag and it is usually desirable. Initially, the linear and the parabolic lift distributions were also considered to obtain simpler equations, as many subsequent integrations were required to obtain wing displacements. On a next stage, it has been found that sizing only for stress was enough to obtain good results, so displacements have be ignored. However all the three load distributions are included in this work, because the comparison among them allows one to qualitatively judge the effect of small variations from the ideal distribution, as a sort of rudimental uncertainty analysis. The resultant of the load distribution along the beam is defined as:

$$F = \int_0^{\ell} q(x)dx \quad (\text{A.1})$$

The mean load distribution is defined as the constant load distribution that have the same resultant:

$$\bar{q} = \frac{F}{\ell} \quad (\text{A.2})$$

The moment induced by the load with respect to the origin is:

$$M_F = \int_0^\ell q(x)x dx \quad (\text{A.3})$$

The arm length of a dump load equivalent to the load distribution is given by:

$$\ell_e = \frac{M_F}{F} \quad (\text{A.4})$$

### Nondimensionalization

The nondimensionalization is useful to obtain rather general equations and to collect all case-specific parameters.

Nondimensional spanwise coordinate, it goes from 0 to 1:

$$\zeta = \frac{x}{\ell} \quad (\text{A.5})$$

Nondimensional load distribution, depicted in Figure 5.4:

$$\tilde{q} = \frac{q}{\bar{q}} \quad (\text{A.6})$$

### Parabolic

The expression of the parabolic load distribution can be written as ( $q_0$  is the magnitude coefficient of the load):

$$q(x) = q_0 \left( 1 - \frac{x^2}{\ell^2} \right) = q_0(1 - \zeta^2) \quad (\text{A.7})$$

The magnitude coefficient  $q_0$  can be calculated for a given resultant  $F$ :

$$F = \int_0^\ell q(x) dx = \int_0^\ell q_0 \left( 1 - \frac{x^2}{\ell^2} \right) dx = \frac{2}{3} \ell q_0 \quad \rightarrow \quad q_0 = \frac{3}{2} \frac{F}{\ell} = \frac{3}{2} \bar{q} \quad (\text{A.8})$$

The location  $\ell_e$  of a dump force equivalent to the load is derived from the expression for the moment of the load:

$$\begin{aligned} M_F &= \int_0^\ell q(x)x dx = \int_0^\ell q_0 \left( 1 - \frac{x^2}{\ell^2} \right) x dx \\ &= \frac{1}{4} q_0 \ell^2 = \frac{3}{8} F \ell \quad \rightarrow \quad \ell_e = \frac{M_F}{F} = \frac{3}{8} \ell \end{aligned} \quad (\text{A.9})$$

### Elliptical

For the elliptical load distribution the equations are:

$$q(x) = q_0 \sqrt{1 - \frac{x^2}{\ell^2}} = q_0 \sqrt{1 - \zeta^2} \quad (\text{A.10})$$

$$F = \int_0^\ell q(x) dx = \int_0^\ell q_0 \sqrt{1 - \frac{x^2}{\ell^2}} dx = \frac{1}{4} \pi \ell q_0 \quad \rightarrow \quad q_0 = \frac{4}{\pi} \frac{F}{\ell} = \frac{4}{\pi} \bar{q} \quad (\text{A.11})$$

$$\begin{aligned} M_F &= \int_0^\ell q(x) x dx = \int_0^\ell q_0 \sqrt{1 - \frac{x^2}{\ell^2}} x dx \\ &= \frac{1}{3} q_0 \ell^2 = \frac{4}{3\pi} F \ell \quad \rightarrow \quad \ell_e = \frac{M_F}{F} = \frac{4}{3\pi} \ell \end{aligned} \quad (\text{A.12})$$

### Linear

The case with linear load distribution is slightly different because it involves two coefficients to control the shape of the load. The second equation required to solve the system has been retrieved by minimizing the Mean Square Error (MSE) between linear and elliptical load distributions, with the load resultant enforced as a constraint.

The expression of a linear load distribution can be written as ( $q_0$  and  $q_1$  are the coefficients that control the shape of the load distribution):

$$q(x) = q_0 + q_1 \frac{x}{\ell} = q_0 + q_1 \zeta \quad (\text{A.13})$$

The constraint equation is obtained by fixing the value of resultant  $F$ :

$$F = \int_0^\ell q(x) dx = \int_0^\ell q_0 + q_1 \frac{x}{\ell} dx = \left( q_0 + \frac{1}{2} q_1 \right) \ell \quad \rightarrow \quad q_0 = \frac{F}{\ell} - \frac{1}{2} q_1 \quad (\text{A.14})$$

The error between the elliptical and the (constrained) linear load distributions is given by:

$$\text{err}(x) = \left[ \frac{4F}{\pi \ell} \sqrt{1 - \frac{x^2}{\ell^2}} \right] - \left[ \frac{F}{\ell} + q_1 \left( \frac{x}{\ell} - \frac{1}{2} \right) \right] \quad (\text{A.15})$$

The problem is solved by calculating the mean square error over the entire beam (integral), and then searching its minimum with respect to the coefficients (null derivative with respect to  $q_1$ ):

$$q_1 : \min_{q_1} \int_0^\ell [\text{err}(x)]^2 dx \quad \rightarrow \quad q_1 = \left( \frac{16}{\pi} - 6 \right) \bar{q}, \quad q_0 = \left( 4 - \frac{8}{\pi} \right) \bar{q} \quad (\text{A.16})$$

This linear load distribution has the same equivalent dump load location  $\ell_e$  of the elliptical case:

$$\begin{aligned} M_F &= \int_0^\ell q(x) x dx = \int_0^\ell \left( q_0 + q_1 \frac{x}{\ell} \right) x dx \\ &= \frac{1}{2} q_0 \ell^2 + \frac{1}{3} q_1 \ell^2 = \frac{4}{3\pi} F \ell \quad \rightarrow \quad \ell_e = \frac{M_F}{F} = \frac{4}{3\pi} \ell \end{aligned} \quad (\text{A.17})$$

### A.1.2. Section Properties

This section contains definitions of some section and geometrical properties, and a couple of useful relations based on the assumption discussed in 5.3 and that are used later on in the document.

The second area moment  $J$  can be defined in terms of the gyration radius  $r_g$  and section resisting area  $A$ :

$$J = r_g^2 A \quad (\text{A.18})$$

The minimum section modulus  $W_{\min}$  is defined through  $y_{\max}$ , that is the distance from elastic axis to the farthest fibre of the resisting section:

$$W_{\min} = \frac{J}{y_{\max}} = \frac{r_g^2}{y_{\max}} A \quad (\text{A.19})$$

The aspect ratio is:

$$\lambda = \frac{b^2}{S} = \frac{b}{c} \quad (\text{A.20})$$

The ratio between cantilever wingspan and strut-braced wingspan is defined:

$$\Delta = \frac{b}{b_0} \quad (\text{A.21})$$

Cantilever and strut-braced wing are compared maintaining the same wing area and the same thickness-to-chord ratio (the subscript "0" identifies the reference cantilever wing):

$$S = bc = b_0 c_0 \quad (\text{A.22})$$

this leads to the following relations that will be used later:

$$\frac{r_{g0}}{r_g} \approx \frac{\frac{1}{2}(t/c)c_0}{\frac{1}{2}(t/c)c} = \frac{c_0}{c} = \frac{S}{b_0 S} = \frac{b}{b_0} = \Delta \quad (\text{A.23})$$

$$\frac{b}{r_g} \approx \frac{b}{\frac{1}{2}(t/c)c} = \frac{2b^2}{(t/c)c_0 b_0} = \frac{2b}{c_0} \frac{\Delta}{(t/c)} = \frac{2b_0}{c_0} \frac{\Delta^2}{(t/c)} = \frac{2\lambda_0 \Delta^2}{(t/c)} \quad (\text{A.24})$$

$$\frac{b_0}{r_{g0}} \approx \frac{b_0}{\frac{1}{2}(t/c)c_0} = \frac{2\lambda_0}{(t/c)} \quad (\text{A.25})$$

## A.2. Cantilever Wing

In this section the equations for the cantilever wing case are derived. Figure A.1 represents a cantilever wing with a generic load distribution.

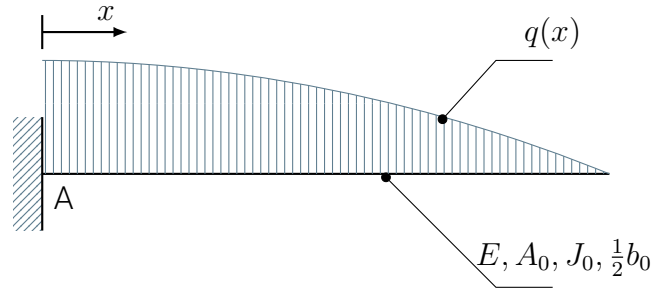


Figure A.1: Cantilever wing scheme and nomenclature.

### A.2.1. Nondimensionalization

As already pointed up in Section A.1.1 for the load distributions, the nondimensionalization has been considered useful to generalize the results and group the case-specific terms.

The nondimensional span-wise coordinate is defined with respect to half of the wing span, or the span of the semi-wing (it goes from 0 at root to 1 at tip):

$$\chi = \frac{x}{\frac{1}{2}b_0} \quad (\text{A.26})$$

The nondimensional internal axial force, shear force and bending moment respectively that are shown in graphs:

$$\tilde{N} = \frac{N}{L} \quad (\text{A.27})$$

$$\tilde{T} = \frac{T}{L} \quad (\text{A.28})$$

$$\tilde{M} = \frac{M}{Lb_0} \quad (\text{A.29})$$

The nondimensional stress and mass, again used to show generalized graphs:

$$\tilde{\sigma} = \frac{\sigma}{\frac{L}{A}} \quad (\text{A.30})$$

$$\tilde{m} = m \left( \frac{\rho}{\sigma_{\max}} \sqrt{S} |L| \right)^{-1} \quad (\text{A.31})$$

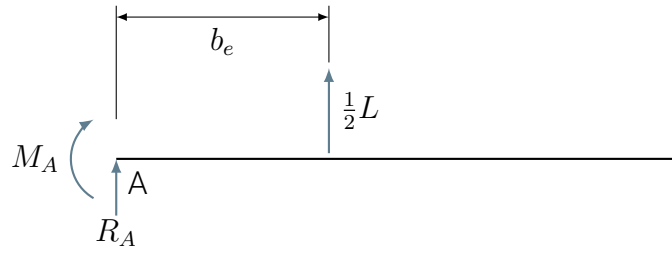


Figure A.2: Cantilever wing reaction forces.

### A.2.2. Reactions

Figure A.2 indicates forces and moments acting on the wing.

#### General

The reactions are obtained enforcing statical equilibrium, these equations are valid for all the load distributions:

$$N_A = 0 \quad (\text{A.32})$$

$$R_A = \int_0^{\frac{1}{2}b_0} q(x) dx = \frac{1}{2}L \quad (\text{A.33})$$

$$M_A = \int_0^{\frac{1}{2}b_0} q(x)x dx = b_e \frac{1}{2}L \quad (\text{A.34})$$

#### Parabolic

In case of parabolic lift distribution the reactions are:

$$R_A = \frac{2}{6}q_0b_0 \quad (\text{A.35})$$

$$M_A = \frac{1}{16}q_0b_0^2 \quad (\text{A.36})$$

$$q_0 = \frac{3}{2} \frac{L}{b_0} \quad (\text{A.37})$$

$$b_e = \frac{3}{16}b_0 \quad (\text{A.38})$$

The parabolic lift distribution is equivalent to a dump force at  $\frac{3}{8}$  of wing semi-span from the root.

### Elliptical

In case of elliptical lift distribution the reactions are:

$$R_A = \frac{1}{8}\pi q_0 b_0 \quad (\text{A.39})$$

$$M_A = \frac{1}{12}q_0 b_0^2 \quad (\text{A.40})$$

$$q_0 = \frac{4}{\pi} \frac{L}{b_0} \quad (\text{A.41})$$

$$b_e = \frac{2}{3\pi} b_0 \quad (\text{A.42})$$

The elliptical lift distribution is equivalent to a dump force at  $\frac{4}{3\pi}$  of wing semi-span from the root.

### Linear

In case of linear lift distribution the reactions are:

$$R_A = \frac{1}{2} \left( q_0 + \frac{1}{2}q_1 \right) b_0 \quad (\text{A.43})$$

$$M_A = \frac{1}{8}q_0 b_0^2 + \frac{1}{12}q_1 b_0^2 \quad (\text{A.44})$$

$$q_0 = \left( 4 - \frac{8}{\pi} \right) \frac{L}{b_0} \quad (\text{A.45})$$

$$q_1 = \left( \frac{16}{\pi} - 6 \right) \frac{L}{b_0} \quad (\text{A.46})$$

$$b_e = \frac{2}{3\pi} b_0 \quad (\text{A.47})$$

The linear lift distribution is equivalent to a dump force at  $\frac{4}{3\pi}$  of wing semi-span from the root (the same of the elliptical distribution).

## A.2.3. Internal Forces

### General

The internal forces are computed through the following equations, valid for a general load distribution:

$$N(x) = 0 \quad (\text{A.48})$$

$$T(x) = T(0) - \int_0^x q(\xi) d\xi \quad (\text{A.49})$$

$$M(x) = M(0) - \int_0^x T(\xi) d\xi \quad (\text{A.50})$$

$$T(0) = R_A \quad (\text{A.51})$$

$$M(0) = M_A \quad (\text{A.52})$$

### Parabolic

In case of parabolic lift distribution the internal forces and moments became:

$$\begin{aligned} T(x) &= T(0) - \int_0^x q(\xi) d\xi = R_A - \int_0^x \frac{1}{2} b_0 q_0 (1 - \zeta^2) d\zeta \\ &= \left( \frac{1}{2} - \frac{3}{4} \chi + \frac{1}{4} \chi^3 \right) L \end{aligned} \quad (\text{A.53})$$

$$\begin{aligned} M(x) &= M(0) - \int_0^x T(\xi) d\xi = M_A - \int_0^x \frac{1}{2} b_0 L \left( \frac{1}{2} - \frac{3}{4} \zeta + \frac{1}{4} \zeta^3 \right) d\zeta \\ &= \left( \frac{3}{32} - \frac{1}{4} \chi + \frac{3}{16} \chi^2 - \frac{1}{32} \chi^4 \right) L b_0 \end{aligned} \quad (\text{A.54})$$

### Elliptical

In case of elliptical lift distribution the internal forces and moments became:

$$T(x) = \dots = \left( \frac{1}{2} - \frac{1}{\pi} \arcsin \chi - \frac{1}{\pi} \chi \sqrt{1 - \chi^2} \right) L \quad (\text{A.55})$$

$$\begin{aligned} M(x) = \dots &= \left[ \frac{1}{2\pi} \left( \chi \arcsin \chi + \sqrt{1 - \chi^2} \right) \right. \\ &\quad \left. + \frac{1}{6\pi} (\chi^2 - 1) \sqrt{1 - \chi^2} - \frac{1}{4} \chi \right] L b_0 \end{aligned} \quad (\text{A.56})$$

### Linear

In case of linear lift distribution the internal forces and moments became:

$$T(x) = \dots = \left[ \frac{1}{2} - \left( 2 - \frac{4}{\pi} \right) \chi - \left( \frac{4}{\pi} - \frac{3}{2} \right) \chi^2 \right] L \quad (\text{A.57})$$

$$M(x) = \dots = \left[ \frac{1}{3\pi} - \frac{1}{4} \chi + \left( \frac{1}{2} - \frac{1}{\pi} \right) \chi^2 + \left( \frac{2}{3\pi} - \frac{1}{4} \right) \chi^3 \right] L b_0 \quad (\text{A.58})$$



### A.2.4. Stress

The maximum stress over the section is computed considering only the bending moment, shear and torsion are not included. The approximations on the section properties are introduced here, this is highlighted in equations by using the symbol " $\approx$ " in place of the equal.

#### Parabolic

The maximum stress over the section varies along the span of the wing, so it is a function of  $\chi$ .

$$\begin{aligned}\sigma(\chi) &= \frac{|M(\chi)|}{W_{\min 0}} = \left( \frac{3}{32} - \frac{1}{4}\chi + \frac{3}{16}\chi^2 - \frac{1}{32}\chi^4 \right) \frac{|L|}{A_0} \frac{b_0}{r_{g0}^2} y_{\max 0} \\ &\approx \left( \frac{3}{32} - \frac{1}{4}\chi + \frac{3}{16}\chi^2 - \frac{1}{32}\chi^4 \right) \frac{|L|}{A_0} \frac{b_0}{r_{g0}} \\ &\approx \left( \frac{3}{16} - \frac{1}{2}\chi + \frac{3}{8}\chi^2 - \frac{1}{16}\chi^4 \right) \frac{|L|}{A_0} \frac{\lambda_0}{(t/c)}\end{aligned}\quad (\text{A.59})$$

The maximum stress over the entire beam is at root, this can be proven but it has been omitted as it is rather intuitive for the cantilever wing, however it can be understood looking at Figure A.11.

$$\sigma_{\max 0} = \frac{|M(0)|}{W_{\min 0}} \approx \frac{3}{16} \frac{|L|}{A_0} \frac{\lambda_0}{(t/c)} \quad (\text{A.60})$$

#### Elliptical

$$\begin{aligned}\sigma(\chi) &= \frac{|M(\chi)|}{W_{\min 0}} = \left[ \frac{1}{2\pi} \left( \chi \arcsin \chi + \sqrt{1 - \chi^2} \right) \right. \\ &\quad \left. + \frac{1}{6\pi} \left( \chi^2 - 1 \right) \sqrt{1 - \chi^2} - \frac{1}{4}\chi \right] \frac{|L|b_0}{A_0 r_{g0}^2} y_{\max 0} \\ &\approx \left[ \frac{1}{\pi} \left( \chi \arcsin \chi + \sqrt{1 - \chi^2} \right) \right. \\ &\quad \left. + \frac{1}{3\pi} \left( \chi^2 - 1 \right) \sqrt{1 - \chi^2} - \frac{1}{2}\chi \right] \frac{|L|\lambda_0}{A_0(t/c)}\end{aligned}\quad (\text{A.61})$$

$$\sigma_{\max 0} = \frac{|M(0)|}{W_{\min 0}} \approx \frac{2}{3\pi} \frac{|L|\lambda_0}{A_0(t/c)} \quad (\text{A.62})$$

#### Linear

$$\sigma(\chi) = \frac{|M(\chi)|}{W_{\min 0}} = \left[ \frac{2}{3\pi} - \frac{1}{2}\chi + \left( 1 - \frac{2}{\pi} \right) \chi^2 + \left( \frac{4}{3\pi} - \frac{1}{2} \right) \chi^3 \right] \frac{|L|\lambda_0}{A_0(t/c)} \quad (\text{A.63})$$

$$\sigma_{\max 0} = \frac{|M(0)|}{W_{\min 0}} \approx \frac{2}{3\pi} \frac{|L|\lambda_0}{A_0(t/c)} \quad (\text{A.64})$$

Note: this linear lift distribution has the same maximum stress of the elliptical one.

### A.2.5. Mass

The mass of the wing ( $m_w$ ) refers to the full wing (both sides). It is estimated considering the *only* contribution given by the resisting structural material.

#### Constant Section - Parabolic

In this case the resisting area is sized at the section with the highest stress and it is kept constant all along the span.

$$A_0 \approx \frac{3}{16} \frac{|L|}{\sigma_{\max}} \frac{\lambda_0}{(t/c)} \quad (\text{A.65})$$

$$m_0 = \rho A_0 b_0 \approx \rho \frac{3}{16} \frac{|L|}{\sigma_{\max}} \frac{\lambda_0}{(t/c)} b_0 \approx \frac{3}{16} |L| \frac{\rho}{\sigma_{\max}} \frac{\sqrt{\lambda_0^3}}{(t/c)} \sqrt{S} \quad (\text{A.66})$$

#### Constant Section - Elliptical

$$A_0 \approx \frac{2}{3\pi} \frac{|L|}{\sigma_{\max}} \frac{\lambda_0}{(t/c)} \quad (\text{A.67})$$

$$m_0 = \rho A_0 b_0 \approx \rho \frac{2}{3\pi} \frac{|L|}{\sigma_{\max}} \frac{\lambda_0}{(t/c)} b_0 \approx \frac{2}{3\pi} |L| \frac{\rho}{\sigma_{\max}} \frac{\sqrt{\lambda_0^3}}{(t/c)} \sqrt{S} \quad (\text{A.68})$$

#### Constant Section - Linear

$$A_0 \approx \frac{2}{3\pi} \frac{|L|}{\sigma_{\max}} \frac{\lambda_0}{(t/c)} \quad (\text{A.69})$$

$$m_0 = \rho A_0 b_0 \approx \frac{2}{3\pi} |L| \frac{\rho}{\sigma_{\max}} \frac{\sqrt{\lambda_0^3}}{(t/c)} \sqrt{S} \quad (\text{A.70})$$

Note: it gives the same result of the elliptical distribution because maximum stress is the same.

#### Variable Section - Parabolic

In this case the resisting area is sized at each section, so the stress is kept constant all along the span and equal to  $\sigma_{\max}$ .

$$A_0(\chi) \approx \left( \frac{3}{16} - \frac{1}{2}\chi + \frac{3}{8}\chi^2 - \frac{1}{16}\chi^4 \right) \frac{|L|}{\sigma_{\max}} \frac{\lambda_0}{(t/c)} \quad (\text{A.71})$$

$$\begin{aligned} m_0 &= \int_0^1 \rho A_0(\chi) b_0 d\chi \approx \rho \frac{|L|}{\sigma_{\max}} \frac{\lambda_0}{(t/c)} b_0 \int_0^1 \left( \frac{3}{16} - \frac{1}{2}\chi + \frac{3}{8}\chi^2 - \frac{1}{16}\chi^4 \right) d\chi \\ &\approx \frac{1}{20} |L| \frac{\rho}{\sigma_{\max}} \frac{\sqrt{\lambda_0^3}}{(t/c)} \sqrt{S} \end{aligned} \quad (\text{A.72})$$

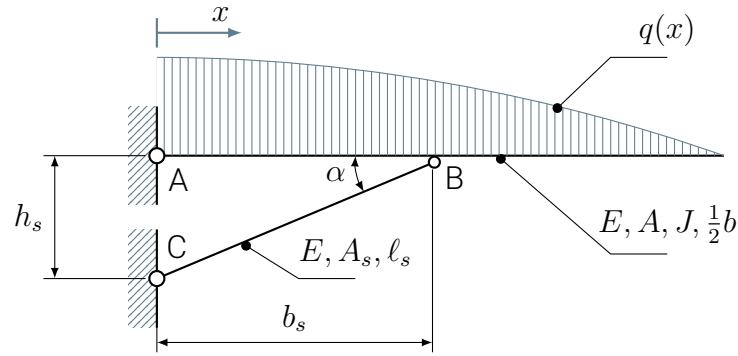


Figure A.3: Strut-braced wing scheme and nomenclature, with a generic load distribution.

### Variable Section - Elliptical

$$A_0(\chi) \approx \left[ \frac{1}{\pi} \left( \chi \arcsin \chi - \sqrt{1 - \chi^2} \right) + \frac{1}{3\pi} \left( \chi^2 - 1 \right) \sqrt{1 - \chi^2} - \frac{1}{2} \chi \right] \frac{|L|}{\sigma_{\max}} \frac{\lambda_0}{(t/c)} \quad (\text{A.73})$$

$$m_0 = \int_0^1 \rho A_0(\chi) b_0 d\chi \approx \rho \frac{|L|}{\sigma_{\max}} \frac{\lambda_0}{(t/c)} b_0 \int_0^1 \left[ \frac{1}{\pi} \left( \chi \arcsin \chi - \sqrt{1 - \chi^2} \right) + \frac{1}{3\pi} \left( \chi^2 - 1 \right) \sqrt{1 - \chi^2} - \frac{1}{2} \chi \right] d\chi \approx \frac{1}{16} |L| \frac{\rho}{\sigma_{\max}} \frac{\sqrt{\lambda_0^3}}{(t/c)} \sqrt{S} \quad (\text{A.74})$$

### Variable Section - Linear

$$A_0(\chi) \approx \left[ \frac{2}{3\pi} - \frac{1}{2} \chi + \left( 1 - \frac{2}{\pi} \right) \chi^2 + \left( \frac{4}{3\pi} - \frac{1}{2} \right) \chi^3 \right] \frac{|L| \lambda_0}{\sigma_{\max} (t/c)} \quad (\text{A.75})$$

$$m_0 = \int_0^1 \rho A_0(\chi) b_0 d\chi = \dots \approx \left( \frac{1}{3\pi} - \frac{1}{24} \right) |L| \frac{\rho}{\sigma_{\max}} \frac{\sqrt{\lambda_0^3}}{(t/c)} \sqrt{S} \quad (\text{A.76})$$

## A.3. Strut Braced Wing

In this section the equations for the strut braced wing are derived. Comments are usually avoided in this section because it has been followed exactly the same procedure already described for the cantilever wing case.

Figure A.3 represents a strut braced wing with a generic load distribution. The following geometrical relations can be verified from the drawing.

$$\tan \alpha = \frac{h_s}{b_s} \quad (\text{A.77})$$

$$\ell_s = \sqrt{h_s^2 + b_s^2} \quad (\text{A.78})$$

$$\sin \alpha = \frac{h_s}{\ell_s} \quad (\text{A.79})$$

$$\cos \alpha = \frac{b_s}{\ell_s} \quad (\text{A.80})$$

### A.3.1. Nondimensionalization

The nondimensional span-wise coordinate is:

$$\chi = \frac{x}{\frac{1}{2}b} \quad (\text{A.81})$$

The nondimensional span-wise location of the strut connection to the wing (strut breakpoint):

$$\chi_s = \frac{b_s}{\frac{1}{2}b} \quad (\text{A.82})$$

The nondimensional vertical location of the strut connection to the fuselage:

$$\gamma_s = \frac{h_s}{\frac{1}{2}b} \quad (\text{A.83})$$

The vertical location can be also nondimensionalized with respect to the reference wing span  $b_0$ .

$$\gamma_{s,0} = \frac{h_s}{\frac{1}{2}b_0} = \gamma_s \Delta \quad (\text{A.84})$$

This is especially practical because the vertical location of the strut connection on the fuselage depends on the fuselage height, that should not change while considering different wing spans. A given  $\gamma_s$  would give a different  $h_s$  with a different wing span  $b$ , on the contrary a given  $\gamma_{s,0}$  fixes  $h_s$  independently of  $b$ .

Below the definitions of, respectively, the nondimensional axial force, shear force, bending moment, stress and mass:

$$\tilde{N} = \frac{N}{L} \quad (\text{A.85})$$

$$\tilde{T} = \frac{T}{L} \quad (\text{A.86})$$

$$\tilde{M} = \frac{M}{Lb} \quad (\text{A.87})$$

$$\tilde{\sigma} = \sigma \frac{A}{L} \quad (\text{A.88})$$

$$\tilde{m} = m \left( \frac{\rho}{\sigma_{\max}} \sqrt{S} |L| \right)^{-1} \quad (\text{A.89})$$

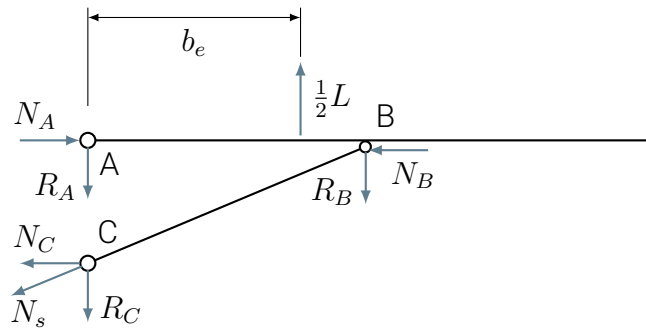


Figure A.4: Strut-braced wing reaction forces.

One last useful relation that will be used later:

$$\ell_s = \frac{1}{2}b\sqrt{\chi_s^2 + \gamma_s^2} = \frac{1}{2}b_0\sqrt{\chi_s^2\Delta^2 + \gamma_{s,0}^2} \quad (\text{A.90})$$

### A.3.2. Reactions

Figure A.4 indicates forces and moments acting on the wing.

#### General

The static equilibrium equations are:

$$R_A + R_B = \frac{1}{2}L \quad (\text{A.91})$$

$$\frac{1}{2}Lb_e - R_Bb_s = 0 \quad (\text{A.92})$$

The reactions forces obtained from static equilibrium:

$$R_A = \frac{1}{2} \left( 1 - \frac{b_e}{b_s} \right) L \quad (\text{A.93})$$

$$R_B = \frac{1}{2} \frac{b_e}{b_s} L \quad (\text{A.94})$$

$$R_C = R_B \quad (\text{A.95})$$

$$N_A = \frac{R_B}{\tan \alpha} = \frac{1}{2} \frac{b_e}{b_s} \frac{b_s}{h_s} L \quad (\text{A.96})$$

$$N_C = N_B = N_A \quad (\text{A.97})$$

$$N_s = \frac{R_B}{\sin \alpha} = \frac{1}{2} \frac{b_e}{b_s} \frac{\ell_s}{h_s} L \quad (\text{A.98})$$

Notes: With positive lift, the strut is pulled and the inner part of the wing is compressed. The strut is subjected only to axial load.

**Parabolic**

$$R_A = \left( \frac{1}{2} - \frac{3}{32} \frac{b}{b_s} \right) L \quad (\text{A.99})$$

$$R_B = \frac{3}{32} \frac{b}{b_s} L \quad (\text{A.100})$$

$$N_A = \frac{3}{32} \frac{b}{b_s} \frac{b_s}{h_s} L \quad (\text{A.101})$$

$$N_s = \frac{3}{32} \frac{b}{b_s} \frac{\ell_s}{h_s} L \quad (\text{A.102})$$

**Elliptical**

$$R_A = \left( \frac{1}{2} - \frac{1}{3\pi} \frac{b}{b_s} \right) L \quad (\text{A.103})$$

$$R_B = \frac{1}{3\pi} \frac{b}{b_s} L \quad (\text{A.104})$$

$$N_A = \frac{1}{3\pi} \frac{b}{b_s} \frac{b_s}{h_s} L \quad (\text{A.105})$$

$$N_s = \frac{1}{3\pi} \frac{b}{b_s} \frac{\ell_s}{h_s} L \quad (\text{A.106})$$

**Linear**

Note: same reactions of the elliptical distribution.

$$R_A = \left( \frac{1}{2} - \frac{1}{3\pi} \frac{b}{b_s} \right) L \quad (\text{A.107})$$

$$R_B = \frac{1}{3\pi} \frac{b}{b_s} L = \frac{2}{3\pi} \frac{1}{\chi_s} L \quad (\text{A.108})$$

$$N_A = \frac{1}{3\pi} \frac{b}{b_s} \frac{b_s}{h_s} L = \frac{2}{3\pi} \frac{1}{\gamma_s} L = \frac{2}{3\pi} \frac{\Delta}{\gamma_{s,0}} L \quad (\text{A.109})$$

$$N_s = \frac{1}{3\pi} \frac{b}{b_s} \frac{\ell_s}{h_s} L = \frac{2}{3\pi} \frac{\sqrt{\gamma_{s,0}^2 + \Delta^2 \chi_s^2}}{\chi_s \gamma_{s,0}} L \quad (\text{A.110})$$

**A.3.3. Internal Forces - First Chunk**

Internal forces and moments calculated for the first chunk of the beam, that means from the wing root to strut breakpoint.

$$x \leq b_s \quad (\text{A.111})$$

**Parabolic**

$$N(x) = N(0) = -N_A = -\frac{3}{32} \frac{b}{h_s} L \quad (\text{A.112})$$

$$\begin{aligned} T(x) &= T(0) - \int_0^x q(\xi) d\xi = R_A - \int_0^x \frac{1}{2} b q_0 (1 - \zeta^2) d\zeta \\ &= \left( \frac{1}{2} - \frac{3}{4} \chi + \frac{1}{4} \chi^3 - \frac{3}{16} \frac{1}{\chi_s} \right) L \end{aligned} \quad (\text{A.113})$$

$$\begin{aligned} M(x) &= M(0) - \int_0^x T(\xi) d\xi = - \int_0^x \left( \frac{1}{2} - \frac{3}{4} \zeta + \frac{1}{4} \zeta^3 - \frac{3}{16} \frac{1}{\chi_s} \right) L \frac{1}{2} b d\zeta \\ &= \left( -\frac{1}{4} \chi + \frac{3}{16} \chi^2 - \frac{1}{32} \chi^4 + \frac{3}{32} \frac{1}{\chi_s} \chi \right) L b \end{aligned} \quad (\text{A.114})$$

**Elliptical**

$$N(x) = -\frac{1}{3\pi} \frac{b}{b_s} \frac{b_s}{h_s} L \quad (\text{A.115})$$

$$T(x) = \dots = \left( \frac{1}{2} - \frac{2}{3\pi} \frac{1}{\chi_s} - \frac{1}{\pi} \arcsin \chi - \frac{1}{\pi} \chi \sqrt{1 - \chi^2} \right) L \quad (\text{A.116})$$

$$\begin{aligned} M(x) &= \dots = \left[ \frac{1}{2\pi} \left( \chi \arcsin \chi + \sqrt{1 - \chi^2} \right) + \frac{1}{6\pi} (\chi^2 - 1) \sqrt{1 - \chi^2} \right. \\ &\quad \left. - \frac{1}{4} \chi + \frac{1}{3\pi} \left( \frac{\chi}{\chi_s} - 1 \right) \right] L b \end{aligned} \quad (\text{A.117})$$

**Linear**

$$N(x) = -\frac{1}{3\pi} \frac{\Delta}{\gamma_{s,0}} L \quad (\text{A.118})$$

$$T(x) = \dots = \left[ \frac{1}{2} - \frac{2}{3\pi} \frac{1}{\chi_s} - \left( 2 - \frac{4}{\pi} \right) \chi - \left( \frac{4}{\pi} - \frac{3}{2} \right) \chi^2 \right] L \quad (\text{A.119})$$

$$M(x) = \dots = \left[ -\frac{1}{4} \chi + \frac{1}{3\pi} \frac{\chi}{\chi_s} + \left( \frac{1}{2} - \frac{1}{\pi} \right) \chi^2 + \left( \frac{2}{3\pi} - \frac{1}{4} \right) \chi^3 \right] L b \quad (\text{A.120})$$

**A.3.4. Internal Forces - Second Chunk**

Internal forces and moments calculated for the second chunk of the beam, that is from the strut breakpoint to the wing tip.

$$x > b_s \quad (\text{A.121})$$

Note: all equation for the second chunk are the same of the cantilever wing (the second chunk can be seen as a cantilever beam constrained to the first chunk).

$$N(x) = N(b_s) + N_B = 0 \quad (\text{A.122})$$

**Parabolic**

$$T(x) = T(b_s) + R_B - \int_{b_s}^x q(\xi) d\xi = \dots = \left( \frac{1}{2} - \frac{3}{4}\chi + \frac{1}{4}\chi^3 \right) L \quad (\text{A.123})$$

$$M(x) = M(b_s) - \int_{b_s}^x T(\xi) d\xi = \dots = \left( -\frac{1}{4}\chi + \frac{3}{16}\chi^2 - \frac{1}{32}\chi^4 + \frac{3}{32} \right) Lb \quad (\text{A.124})$$

**Elliptical**

$$T(x) = \dots = \left( \frac{1}{2} - \frac{1}{\pi} \arcsin \chi - \frac{1}{\pi} \chi \sqrt{1 - \chi^2} \right) L \quad (\text{A.125})$$

$$M(x) = \dots = \left[ \frac{1}{2\pi} \left( \chi \arcsin \chi + \sqrt{1 - \chi^2} \right) + \frac{1}{6\pi} (\chi^2 - 1) \sqrt{1 - \chi^2} - \frac{1}{4}\chi \right] Lb \quad (\text{A.126})$$

**Linear**

$$T(x) = \dots = \left[ \frac{1}{2} - \left( 2 - \frac{4}{\pi} \right) \chi - \left( \frac{4}{\pi} - \frac{3}{2} \right) \chi^2 \right] L \quad (\text{A.127})$$

$$M(x) = \dots = \left[ -\frac{1}{4}\chi + \frac{1}{3\pi} + \left( \frac{1}{2} - \frac{1}{\pi} \right) \chi^2 + \left( \frac{2}{3\pi} - \frac{1}{4} \right) \chi^3 \right] Lb \quad (\text{A.128})$$

**A.3.5. Internal Forces - Complete**

The equations from the two chunks can be combined together taking advantage of the step function, defined as follows:

$$\text{step}(\zeta) = \begin{cases} 0 & \zeta \leq 0 \\ 1 & \zeta > 0 \end{cases} \quad (\text{A.129})$$

**Parabolic**

$$\begin{aligned} N(x) &= \frac{3}{32} \frac{b}{h_s} (\text{step}(\chi - \chi_s) - 1) L = \frac{3}{32} \frac{1}{\gamma_s} (\text{step}(\chi - \chi_s) - 1) L \\ &= \frac{3}{32} \frac{\Delta}{\gamma_{s,0}} (\text{step}(\chi - \chi_s) - 1) L \end{aligned} \quad (\text{A.130})$$

$$T(x) = \left( \frac{1}{2} - \frac{3}{4}\chi + \frac{1}{4}\chi^3 - \frac{3}{16} \frac{1}{\chi_s} + \frac{3}{16} \frac{1}{\chi_s} \text{step}(\chi - \chi_s) \right) L \quad (\text{A.131})$$

$$\begin{aligned} M(x) &= \left( -\frac{1}{4}\chi + \frac{3}{16}\chi^2 - \frac{1}{32}\chi^4 + \frac{3}{32} \frac{\chi}{\chi_s} \right. \\ &\quad \left. - \frac{3}{32} \frac{\chi - \chi_s}{\chi_s} \text{step}(\chi - \chi_s) \right) Lb \end{aligned} \quad (\text{A.132})$$



**Elliptical**

$$N(x) = \frac{1}{3\pi} \frac{b}{b_s} \frac{b_s}{h_s} (\text{step}(\chi - \chi_s) - 1)L = \frac{1}{3\pi} \frac{\Delta}{\gamma_{s,0}} (\text{step}(\chi - \chi_s) - 1)L \quad (\text{A.133})$$

$$T(x) = \left[ \frac{1}{2} - \frac{1}{\pi} \arcsin \chi - \frac{1}{\pi} \chi \sqrt{1 - \chi^2} - \frac{2}{3\pi} \frac{1}{\chi_s} + \frac{2}{3\pi} \frac{1}{\chi_s} \text{step}(\chi - \chi_s) \right] L \quad (\text{A.134})$$

$$M(x) = \left[ \frac{1}{2\pi} \left( \chi \arcsin \chi + \sqrt{1 - \chi^2} \right) + \frac{1}{6\pi} (\chi^2 - 1) \sqrt{1 - \chi^2} - \frac{1}{4} \chi + \frac{1}{3\pi} \left( \frac{\chi}{\chi_s} - 1 \right) - \frac{1}{3\pi} \left( \frac{\chi}{\chi_s} - 1 \right) \text{step}(\chi - \chi_s) \right] Lb \quad (\text{A.135})$$

**Linear**

$$N(x) = \frac{1}{3\pi} \frac{\Delta}{\gamma_{s,0}} (\text{step}(\chi - \chi_s) - 1)L \quad (\text{A.136})$$

$$T(x) = \dots = \left[ \frac{1}{2} - \left( 2 - \frac{4}{\pi} \right) \chi - \left( \frac{4}{\pi} - \frac{3}{2} \right) \chi^2 - \frac{2}{3\pi} \frac{1}{\chi_s} + \frac{2}{3\pi} \frac{1}{\chi_s} \text{step}(\chi - \chi_s) \right] L \quad (\text{A.137})$$

$$M(x) = \dots = \left[ -\frac{1}{4} \chi + \left( \frac{1}{2} - \frac{1}{\pi} \right) \chi^2 + \left( \frac{2}{3\pi} - \frac{1}{4} \right) \chi^3 + \frac{1}{3\pi} \frac{\chi}{\chi_s} - \frac{1}{3\pi} \frac{\chi - \chi_s}{\chi_s} \text{step}(\chi - \chi_s) \right] Lb \quad (\text{A.138})$$

**A.3.6. Internal Forces - Strut**

The axial force acting on the strut, which is the only non-zero internal force.

**Parabolic**

$$N_s = \frac{3}{32} \frac{b}{b_s} \frac{\ell_s}{h_s} L = \frac{3}{16} \frac{\sqrt{\gamma_s^2 + \chi_s^2}}{\chi_s \gamma_s} L = \frac{3}{16} \frac{\sqrt{\gamma_{s,0}^2 + \Delta^2 \chi_s^2}}{\chi_s \gamma_{s,0}} L \quad (\text{A.139})$$

**Elliptical**

$$N_s = \frac{1}{3\pi} \frac{b}{b_s} \frac{\ell_s}{h_s} L = \frac{2}{3\pi} \frac{\sqrt{\gamma_{s,0}^2 + \Delta^2 \chi_s^2}}{\chi_s \gamma_{s,0}} L \quad (\text{A.140})$$

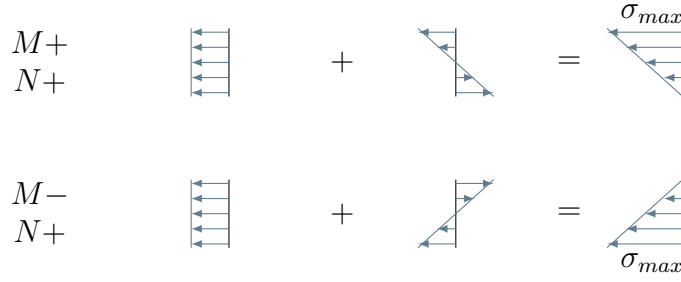


Figure A.5: Summation of bending stress and normal stress (clarification on presence of absolute value in the stress equation).

### Linear

Note: it is the same result of the elliptical distribution.

$$N_s = \frac{2}{3\pi} \frac{\sqrt{\gamma_{s,0}^2 + \Delta^2 \chi_s^2}}{\chi_s \gamma_{s,0}} L \quad (\text{A.141})$$

### A.3.7. Stress

Notes: only bending moment and axial load are considered, torsion and shear have been ignored. For sake of clarity, the absolute value is needed to find the maximum stress, see Figure A.5.

### Parabolic

$$\begin{aligned} \sigma(\chi) &= \frac{|M(\chi)|}{W_{\min}} + \frac{|N(\chi)|}{A} \\ &= \left| -\frac{1}{4}\chi + \frac{3}{16}\chi^2 - \frac{1}{32}\chi^4 + \frac{3}{32} \frac{\chi}{\chi_s} - \frac{3}{32} \frac{\chi - \chi_s}{\chi_s} \text{step}(\chi - \chi_s) \right| \frac{|L|}{A} \frac{b}{r_g^2} y_{\max} \\ &\quad + \frac{3}{32} \frac{\Delta}{\gamma_{s,0}} [1 - \text{step}(\chi - \chi_s)] \frac{|L|}{A} \\ &\approx \left| -\frac{1}{4}\chi + \frac{3}{16}\chi^2 - \frac{1}{32}\chi^4 + \frac{3}{32} \frac{\chi}{\chi_s} - \frac{3}{32} \frac{\chi - \chi_s}{\chi_s} \text{step}(\chi - \chi_s) \right| \frac{|L|}{A} \frac{b}{r_g} \\ &\quad + \frac{3}{32} \frac{\Delta}{\gamma_{s,0}} [1 - \text{step}(\chi - \chi_s)] \frac{L}{A} \\ &\approx \left| -\frac{1}{2}\chi + \frac{3}{8}\chi^2 - \frac{1}{16}\chi^4 + \frac{3}{16} \frac{\chi}{\chi_s} - \frac{3}{16} \frac{\chi - \chi_s}{\chi_s} \text{step}(\chi - \chi_s) \right| \frac{|L|}{A} \frac{\lambda_0 \Delta^2}{(t/c)} \\ &\quad + \frac{3}{32} \frac{\Delta}{\gamma_{s,0}} [1 - \text{step}(\chi - \chi_s)] \frac{L}{A} \end{aligned} \quad (\text{A.142})$$

**Elliptical**

$$\begin{aligned}
\sigma(\chi) &= \frac{|M(\chi)|}{W_{\min}} + \frac{|N(\chi)|}{A} \\
&= \left| \frac{1}{2\pi} \left( \chi \arcsin \chi + \sqrt{1 - \chi^2} \right) + \frac{1}{6\pi} (\chi^2 - 1) \sqrt{1 - \chi^2} - \frac{1}{4} \chi \right. \\
&\quad \left. + \frac{1}{3\pi} \left( \frac{\chi}{\chi_s} - 1 \right) [1 - \text{step}(\chi - \chi_s)] \right| \frac{|L|b}{A r_g^2} y_{\max} \\
&\quad + \frac{1}{3\pi} \frac{\Delta}{\gamma_{s,0}} [1 - \text{step}(\chi - \chi_s)] \frac{|L|}{A} \\
&\approx \left| \frac{1}{\pi} \left( \chi \arcsin \chi + \sqrt{1 - \chi^2} \right) + \frac{1}{3\pi} (\chi^2 - 1) \sqrt{1 - \chi^2} - \frac{1}{2} \chi \right. \\
&\quad \left. + \frac{2}{3\pi} \left( \frac{\chi}{\chi_s} - 1 \right) [1 - \text{step}(\chi - \chi_s)] \right| \frac{|L| \lambda_0 \Delta^2}{A (t/c)} \\
&\quad + \frac{1}{3\pi} \frac{\Delta}{\gamma_{s,0}} [1 - \text{step}(\chi - \chi_s)] \frac{|L|}{A}
\end{aligned} \tag{A.143}$$

**Linear**

$$\begin{aligned}
\sigma(\chi) &= \frac{|M(\chi)|}{W_{\min}} + \frac{|N(\chi)|}{A} \\
&\approx \left| -\frac{1}{2} \chi + \left( 1 - \frac{2}{\pi} \right) \chi^2 + \left( \frac{4}{3\pi} - \frac{1}{2} \right) \chi^3 \right. \\
&\quad \left. + \frac{2}{3\pi} \frac{\chi}{\chi_s} - \frac{2}{3\pi} \frac{\chi - \chi_s}{\chi_s} \text{step}(\chi - \chi_s) \right| \frac{|L| \lambda_0 \Delta^2}{A (t/c)} \\
&\quad + \frac{1}{3\pi} \frac{\Delta}{\gamma_{s,0}} [1 - \text{step}(\chi - \chi_s)] \frac{|L|}{A}
\end{aligned} \tag{A.144}$$

**Strut - Parabolic**

$$\sigma_s = \frac{|N_s|}{A_s} = \frac{3}{16} \frac{\sqrt{\gamma_{s,0}^2 + \Delta^2 \chi_s^2}}{\chi_s \gamma_{s,0}} \frac{|L|}{A_s} \tag{A.145}$$

**Strut - Elliptical**

$$\sigma_s = \frac{|N_s|}{A_s} = \frac{2}{3\pi} \frac{\sqrt{\gamma_{s,0}^2 + \Delta^2 \chi_s^2}}{\chi_s \gamma_{s,0}} \frac{|L|}{A_s} \tag{A.146}$$

### Strut - Linear

Note: it is the same result of the elliptical distribution.

$$\sigma_s = \frac{|N_s|}{A_s} = \frac{2}{3\pi} \frac{\sqrt{\gamma_{s,0}^2 + \Delta^2 \chi_s^2}}{\chi_s \gamma_{s,0}} \frac{|L|}{A_s} \quad (\text{A.147})$$

### A.3.8. Maximum Stress

In order to size a constant section wing, it is necessary to find the overall maximum stress along the wing. In case of cantilever wing this was always at the root, in case of strut braced wing it turns out to be harder to find its location and so, its value. For this reason, the maximum stress is searched analytically only for the parabolic lift distribution, and then findings are applied also to the other distributions.

#### Parabolic

Axial load is constant, so the most stressed section along the wing corresponds to the section at which the bending moment is maximum.

$$\max_{\chi} \tilde{M}(\chi) : \frac{\partial \tilde{M}}{\partial \chi} = 0 \quad (\text{A.148})$$

$$\frac{\partial \tilde{M}}{\partial \chi} = -1 + \frac{3}{2}\chi - \frac{1}{2}\chi^3 + \frac{3}{8} \frac{1}{\chi_s} - \frac{3}{8} \frac{1}{\chi_s} \text{step}(\chi - \chi_s) \quad (\text{A.149})$$

$$\chi > \chi_s \rightarrow \frac{\partial \tilde{M}}{\partial \chi} = -1 + \frac{3}{2}\chi - \frac{1}{2}\chi^3 \quad (\text{A.150})$$

The only solution for  $\chi > \chi_s$  is at the tip ( $\chi = 1$ ) in which the bending moment is zero (the slope of the function is monotonic decreasing:  $\frac{\partial^2 \tilde{M}}{\partial \chi^2} = \frac{3}{2} - \frac{3}{2}\chi^2$ ), so the maximum bending moment must be at  $\chi \leq \chi_s$ .

The exact location of the maximum for  $\chi \leq \chi_s$  is obtained by solving the following third order equation:

$$\chi \leq \chi_s \rightarrow \frac{\partial \tilde{M}}{\partial \chi} = -1 + \frac{3}{2}\chi - \frac{1}{2}\chi^3 + \frac{3}{8} \frac{1}{\chi_s} = 0 \quad (\text{A.151})$$

but the resulting expression of the analytical solution is of poor utility:

$$\chi_0 = \begin{cases} \sqrt[3]{\left(\frac{3}{8} \frac{1}{\chi_s} - 1\right) + \sqrt{\frac{9}{64} \frac{1}{\chi_s} - \frac{3}{4} \frac{1}{\chi_s}}} & \chi_s \leq \frac{3}{16} \\ + \sqrt[3]{\left(\frac{3}{8} \frac{1}{\chi_s} - 1\right) - \sqrt{\frac{9}{64} \frac{1}{\chi_s} - \frac{3}{4} \frac{1}{\chi_s}}} & \\ 2 \cos \left[ \frac{1}{3} \text{atan} \left( \frac{\sqrt{\frac{3}{4} \frac{1}{\chi_s} - \frac{9}{64} \frac{1}{\chi_s^2}}}{\frac{3}{8} \frac{1}{\chi_s} - 1} \right) \right] & \chi_s > \frac{3}{16} \end{cases} \quad (\text{A.152})$$

Figure A.6 indicates maximum bending moment and its location along the wing as a function of strut breakpoint  $\chi_s$  (obtained numerically from equation A.148). The maximum bending moment is at the strut breakpoint for  $\chi_s \leq 0.55$ , when  $\chi_s > 0.55$

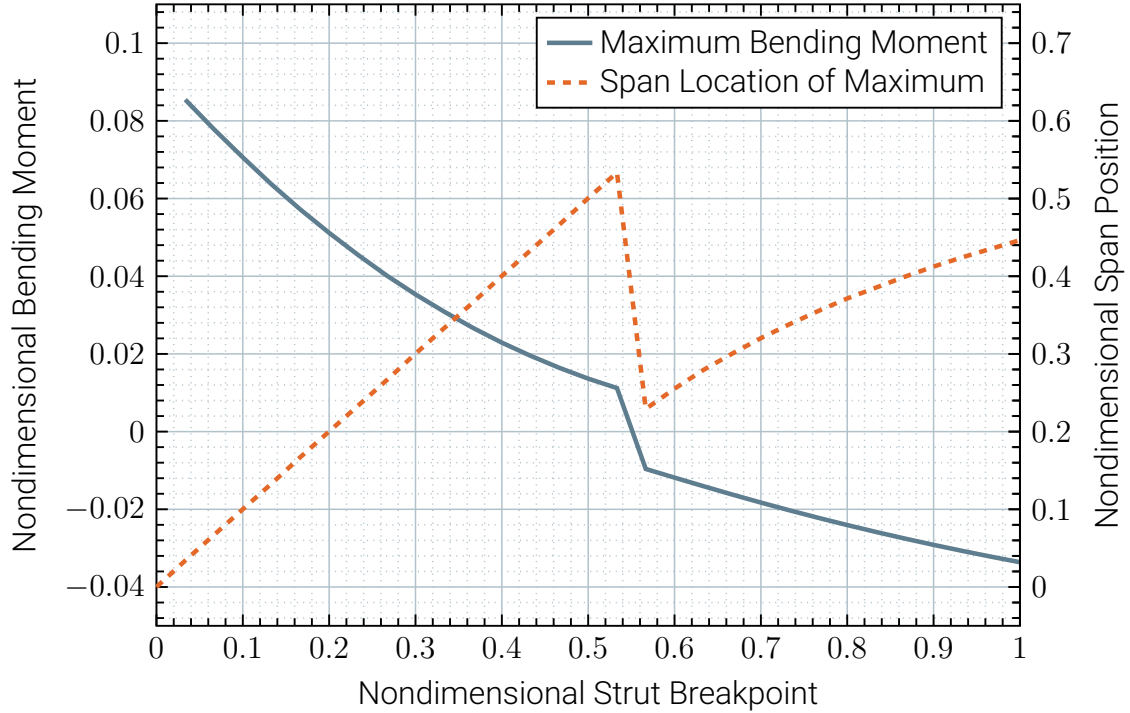


Figure A.6: Maximum bending moment and its span-wise location for different  $\chi_s$  (numerical solution).

the maximum bending moment is in the inner part of the wing. It can be also seen that this point is the optimal strut breakpoint, in the sense that it leads to the lowest maximum stress. So the optimal strut breakpoint is  $\chi_{s,opt} \approx 0.55$  for the parabolic lift distribution.

Fortunately, the maximum stress for  $\chi > \chi_{s,opt}$  is not of much interest, because this solution is sub-optimal and it also leads to longer strut that generates more drag and that is more prone to buckling. For  $\chi \leq \chi_{s,opt}$  the location of the maximum is known (it is at the strut breakpoint), so it can be easily computed:

$$\begin{aligned}
 \sigma_{\max} &= \frac{|M(b_s)|}{W_{\min}} + \frac{|N|}{A} \\
 &= \left( -\frac{1}{4}\chi_s + \frac{3}{16}\chi_s^2 - \frac{1}{32}\chi_s^4 + \frac{3}{32} \right) \frac{|L|b}{W_{\min}} + \frac{3}{32} \frac{\Delta}{\gamma_{s,0}} \frac{|L|}{A} \\
 &= \left( -\frac{1}{4}\chi_s + \frac{3}{16}\chi_s^2 - \frac{1}{32}\chi_s^4 + \frac{3}{32} \right) \frac{|L|b}{r_g^2 A} y_{\max} + \frac{3}{32} \frac{\Delta}{\gamma_{s,0}} \frac{|L|}{A} \\
 &\approx \left( -\frac{1}{4}\chi_s + \frac{3}{16}\chi_s^2 - \frac{1}{32}\chi_s^4 + \frac{3}{32} \right) \frac{|L|b}{r_g A} + \frac{3}{32} \frac{\Delta}{\gamma_{s,0}} \frac{|L|}{A} \\
 &\approx \left( -\frac{1}{2}\chi_s + \frac{3}{8}\chi_s^2 - \frac{1}{16}\chi_s^4 + \frac{3}{16} \right) \frac{|L|}{A} \frac{\lambda_0 \Delta^2}{(t/c)} + \frac{3}{32} \frac{\Delta}{\gamma_{s,0}} \frac{|L|}{A}
 \end{aligned} \tag{A.153}$$

## Elliptical

The same reasoning done for parabolic lift distribution applies to elliptical lift distribution but it gives a different numerical result. In fact, the optimal strut breakpoint (that gives the lowest maximum stress) is  $\chi_{s,opt} \approx 0.6$ .

$$\begin{aligned} \sigma_{\max} &= \frac{|M(b_s)|}{W_{\min}} + \frac{|N|}{A} \approx \left[ \frac{1}{\pi} \left( \chi_s \arcsin \chi_s + \sqrt{1 - \chi_s^2} \right) \right. \\ &\quad \left. + \frac{1}{3\pi} (\chi_s^2 - 1) \sqrt{1 - \chi_s^2} - \frac{1}{2} \chi_s \right] \frac{|L| \lambda_0 \Delta^2}{A (t/c)} + \frac{1}{3\pi} \frac{\Delta}{\gamma_{s,0}} \frac{|L|}{A} \end{aligned} \quad (\text{A.154})$$

## Linear

The optimal strut breakpoint (that gives the lowest maximum stress) for the linear lift distribution is  $\chi_{s,opt} \approx 0.65$ .

$$\begin{aligned} \sigma_{\max} &= \frac{|M(b_s)|}{W_{\min}} + \frac{|N|}{A} \\ &\approx \left[ -\frac{1}{2} \chi_s + \left( 1 - \frac{2}{\pi} \right) \chi_s^2 + \left( \frac{4}{3\pi} - \frac{1}{2} \right) \chi_s^3 + \frac{2}{3\pi} \right] \frac{|L| \lambda_0 \Delta^2}{A (t/c)} \\ &\quad + \frac{1}{3\pi} \frac{\Delta}{\gamma_{s,0}} \frac{|L|}{A} \end{aligned} \quad (\text{A.155})$$

### A.3.9. Strut Buckling

The same load distribution has been considered but with a negative load. This is done to use the structural constraint given by the load factors, for example  $n_{lim} = \langle n_{\max}, n_{\min} \rangle = \langle +4, -2 \rangle$ . The positive limits is higher in modulus than the negative limit, so the strut area is sized from the positive load factor. The ratio between the two limits is defined:

$$n_{\text{ratio}} = \frac{|n_{\max}|}{|n_{\min}|} = \frac{|L_+|}{|L_-|} \quad (\text{A.156})$$

$$\sigma_{s,cr} = \frac{|N_{s,cr}|}{A_s} = \frac{\pi^2 E J_s}{\ell_s^2} \frac{1}{A_s} = \frac{\pi^2 E}{\ell_s^2} r_{gs}^2 \quad (\text{A.157})$$

$$\sigma_s \leq \sigma_{s,cr} \quad (\text{A.158})$$

As the area of the strut  $A_s$  as been already sized then:

$$\sigma_{s,-} = \frac{|N_{max,-}|}{A_s} = \frac{|N_{max,-}|}{|N_{max,+}|} \sigma_{\max} = \dots = \frac{\sigma_{\max}}{n_{\text{ratio}}} \quad (\text{A.159})$$

so it is possible to calculate the minimum required radius of gyration:

$$\sigma_{s,-} \leq \frac{\pi^2 E}{\ell_s^2} r_{gs}^2 \quad \rightarrow \quad r_{gs} \geq \sqrt{\frac{\sigma_{s,-} \ell_s^2}{\pi^2 E}} = \sqrt{\frac{1}{n_{\text{ratio}}} \frac{\sigma_{\max}}{\pi^2 E} \ell_s^2} \quad (\text{A.160})$$

and the minimum required thickness of the strut:

$$t_s = c_s (t/c)_s \gtrsim \sqrt{\frac{1}{n_{\text{ratio}}} \frac{\sigma_{\max}}{\pi^2 E} (\gamma_{s,0}^2 + \Delta^2 \chi_s^2) S \lambda_0} \quad (\text{A.161})$$

### A.3.10. Mass

The mass of the wing ( $m_w$ ) refers to the full wing (both sides). The mass of the struts ( $m_s$ ) includes both struts. The mass of the wing assembly (wing + struts) is simply given by:

$$m_{wa} = m_w + m_s \quad (\text{A.162})$$

#### Strut - Parabolic

$$A_s = \frac{3}{16} \frac{\sqrt{\gamma_{s,0}^2 + \Delta^2 \chi_s^2}}{\chi_s \gamma_{s,0}} \frac{|L|}{\sigma_{\max}} \quad (\text{A.163})$$

$$\ell_s = \sqrt{b_s^2 + h_s^2} = \frac{1}{2} b \sqrt{\chi_s^2 + \gamma_s^2} = \frac{1}{2} b_0 \sqrt{\Delta^2 \chi_s^2 + \gamma_{s,0}^2} \quad (\text{A.164})$$

$$\begin{aligned} m_s &= 2\rho A_s \ell_s = 2\rho \frac{3}{32} \frac{\gamma_{s,0}^2 + \Delta^2 \chi_s^2}{\chi_s \gamma_{s,0}} \frac{|L|}{\sigma_{\max}} b_0 \\ &= \frac{3}{16} \frac{\gamma_{s,0}^2 + \Delta^2 \chi_s^2}{\chi_s \gamma_{s,0}} \frac{\rho}{\sigma_{\max}} \sqrt{\lambda_0} \sqrt{S} |L| \end{aligned} \quad (\text{A.165})$$

#### Strut - Elliptical

$$A_s = \frac{2}{3\pi} \frac{\sqrt{\gamma_{s,0}^2 + \Delta^2 \chi_s^2}}{\chi_s \gamma_{s,0}} \frac{|L|}{\sigma_{\max}} \quad (\text{A.166})$$

$$m_s = 2\rho A_s \ell_s = \frac{2}{3\pi} \frac{\gamma_{s,0}^2 + \Delta^2 \chi_s^2}{\chi_s \gamma_{s,0}} \frac{\rho}{\sigma_{\max}} \sqrt{\lambda_0} \sqrt{S} |L| \quad (\text{A.167})$$

#### Strut - Linear

Note: it is the same of the elliptical distribution.

$$A_s = \frac{2}{3\pi} \frac{\sqrt{\gamma_{s,0}^2 + \Delta^2 \chi_s^2}}{\chi_s \gamma_{s,0}} \frac{|L|}{\sigma_{\max}} \quad (\text{A.168})$$

$$m_s = 2\rho A_s \ell_s = \frac{2}{3\pi} \frac{\gamma_{s,0}^2 + \Delta^2 \chi_s^2}{\chi_s \gamma_{s,0}} \frac{\rho}{\sigma_{\max}} \sqrt{\lambda_0} \sqrt{S} |L| \quad (\text{A.169})$$

#### Constant Section Wing - Parabolic

In this case the resisting area is sized at the section with the highest stress and it is kept constant along the span. The equation is valid only for  $\chi_s \leq \chi_{s,opt} \approx 0.55$ , because it has been assumed that the maximum stress is at the strut breakpoint.

$$A \approx \left( -\frac{1}{2} \chi_s + \frac{3}{8} \chi_s^2 - \frac{1}{16} \chi_s^4 + \frac{3}{16} \right) \frac{|L|}{\sigma_{\max}} \frac{\lambda_0 \Delta^2}{(t/c)} + \frac{3}{32} \frac{\Delta}{\gamma_{s,0}} \frac{|L|}{\sigma_{\max}} \quad (\text{A.170})$$

$$m_w = \rho Ab \approx \left( -\frac{1}{2}\chi_s + \frac{3}{8}\chi_s^2 - \frac{1}{16}\chi_s^4 + \frac{3}{16} \right) \frac{\rho}{\sigma_{\max}} \frac{\sqrt{\lambda_0^3 \Delta^3}}{(t/c)} \sqrt{S} |L| + \frac{3}{32} \frac{\Delta^2}{\gamma_{s,0}} \frac{\rho}{\sigma_{\max}} \sqrt{\lambda_0} \sqrt{S} |L| \quad (\text{A.171})$$

### Constant Section Wing - Elliptical

In this case the equation is valid only for  $\chi_s \leq \chi_{s,opt} \approx 0.6$ .

$$A \approx \left[ \frac{1}{\pi} \left( \chi_s \arcsin \chi_s + \sqrt{1 - \chi_s^2} \right) + \frac{1}{3\pi} (\chi_s^2 - 1) \sqrt{1 - \chi_s^2} - \frac{1}{2}\chi_s \right] \frac{|L|}{\sigma_{\max}} \frac{\lambda_0 \Delta^2}{(t/c)} + \frac{1}{3\pi} \frac{\Delta}{\gamma_{s,0}} \frac{|L|}{\sigma_{\max}} \quad (\text{A.172})$$

$$m_w = \rho Ab \approx \left[ \frac{1}{\pi} \left( \chi_s \arcsin \chi_s + \sqrt{1 - \chi_s^2} \right) + \frac{1}{3\pi} (\chi_s^2 - 1) \sqrt{1 - \chi_s^2} - \frac{1}{2}\chi_s \right] \frac{\rho}{\sigma_{\max}} \frac{\sqrt{\lambda_0^3 \Delta^3}}{(t/c)} \sqrt{S} |L| + \frac{1}{3\pi} \frac{\Delta^2}{\gamma_{s,0}} \frac{\rho}{\sigma_{\max}} \sqrt{\lambda_0} \sqrt{S} |L| \quad (\text{A.173})$$

### Constant Section Wing - Linear

In this case the equation is valid only for  $\chi_s \leq \chi_{s,opt} \approx 0.65$ .

$$A \approx \left[ -\frac{1}{2}\chi_s + \left(1 - \frac{2}{\pi}\right)\chi_s^2 + \left(\frac{4}{3\pi} - \frac{1}{2}\right)\chi_s^3 + \frac{2}{3\pi} \right] \frac{|L|}{\sigma_{\max}} \frac{\lambda_0 \Delta^2}{(t/c)} + \frac{1}{3\pi} \frac{\Delta}{\gamma_{s,0}} \frac{|L|}{\sigma_{\max}} \quad (\text{A.174})$$

$$m_w = \rho Ab \approx \left[ -\frac{1}{2}\chi_s + \left(1 - \frac{2}{\pi}\right)\chi_s^2 + \left(\frac{4}{3\pi} - \frac{1}{2}\right)\chi_s^3 + \frac{2}{3\pi} \right] \frac{\rho}{\sigma_{\max}} \frac{\sqrt{\lambda_0^3 \Delta^3}}{(t/c)} \sqrt{S} |L| + \frac{1}{3\pi} \frac{\Delta^2}{\gamma_{s,0}} \frac{\rho}{\sigma_{\max}} \sqrt{\lambda_0} \sqrt{S} |L| \quad (\text{A.175})$$

### Variable Section Wing - Parabolic

In this case the resisting area is sized at each section, so the stress is kept constant all along the span.

$$A(\chi) \approx \left| -\frac{1}{2}\chi + \frac{3}{8}\chi^2 - \frac{1}{16}\chi^4 + \frac{3}{16} \frac{\chi}{\chi_s} - \frac{3}{16} \frac{\chi - \chi_s}{\chi_s} \text{step}(\chi - \chi_s) \right| \frac{|L|}{A} \frac{\lambda_0 \Delta^2}{(t/c)} + \frac{3}{32} \frac{\Delta}{\gamma_{s,0}} [1 - \text{step}(\chi - \chi_s)] \frac{L}{A} \quad (\text{A.176})$$



$$\begin{aligned}
m_w &= \int_0^1 \rho A(\chi) b d\chi \approx \frac{\rho}{\sigma_{\max}} \frac{\sqrt{\lambda_0^3 \Delta^3}}{(t/c)} \sqrt{S} |L| \times \\
&\times \int_0^1 \left| -\frac{1}{2}\chi + \frac{3}{8}\chi^2 - \frac{1}{16}\chi^4 + \frac{3}{16} \frac{\chi}{\chi_s} - \frac{3}{16} \frac{\chi - \chi_s}{\chi_s} \text{step}(\chi - \chi_s) \right| d\chi \\
&+ \frac{3}{32} \chi_s \frac{\Delta^2}{\gamma_{s,0} \sigma_{\max}} \sqrt{\lambda_0} \sqrt{S} |L| \\
&\approx \frac{\rho}{\sigma_{\max}} \frac{\sqrt{\lambda_0^3 \Delta^3}}{(t/c)} \sqrt{S} |L| I_P(\chi_s) + \frac{3}{32} \chi_s \frac{\Delta^2}{\gamma_{s,0} \sigma_{\max}} \sqrt{\lambda_0} \sqrt{S} |L|
\end{aligned} \tag{A.177}$$

Unfortunately this last integral requires a numerical solution, but later on the results are interpolated with polynomials and their coefficients are given in Table A.1.

### Variable Section Wing - Elliptical

$$\begin{aligned}
A(\chi) &\approx \left| \frac{1}{\pi} \left( \chi \arcsin \chi + \sqrt{1 - \chi^2} \right) + \frac{1}{3\pi} (\chi^2 - 1) \sqrt{1 - \chi^2} - \frac{1}{2}\chi \right. \\
&+ \left. \frac{2}{3\pi} \left( \frac{\chi}{\chi_s} - 1 \right) [1 - \text{step}(\chi - \chi_s)] \right| \frac{|L|}{\sigma_{\max}} \frac{\lambda_0 \Delta^2}{(t/c)} \\
&+ \frac{1}{3\pi} \frac{\Delta}{\gamma_{s,0}} [1 - \text{step}(\chi - \chi_s)] \frac{|L|}{\sigma_{\max}}
\end{aligned} \tag{A.178}$$

$$\begin{aligned}
m_w &= \int_0^1 \rho A(\chi) b d\chi \approx \frac{\rho}{\sigma_{\max}} \frac{\sqrt{\lambda_0^3 \Delta^3}}{(t/c)} \sqrt{S} |L| \int_0^1 \left| \frac{1}{\pi} \left( \chi \arcsin \chi + \sqrt{1 - \chi^2} \right) \right. \\
&+ \left. \frac{1}{3\pi} (\chi^2 - 1) \sqrt{1 - \chi^2} - \frac{1}{2}\chi + \frac{2}{3\pi} \left( \frac{\chi}{\chi_s} - 1 \right) [1 - \text{step}(\chi - \chi_s)] \right| d\chi \\
&+ \frac{1}{3\pi} \chi_s \frac{\Delta^2}{\gamma_{s,0} \sigma_{\max}} \sqrt{\lambda_0} \sqrt{S} |L| \\
&\approx \frac{\rho}{\sigma_{\max}} \frac{\sqrt{\lambda_0^3 \Delta^3}}{(t/c)} \sqrt{S} |L| I_E(\chi_s) + \frac{1}{3\pi} \chi_s \frac{\Delta^2}{\gamma_{s,0} \sigma_{\max}} \sqrt{\lambda_0} \sqrt{S} |L|
\end{aligned} \tag{A.179}$$

Unfortunately this last integral requires a numerical solution, but later on the results are interpolated with polynomials and their coefficients are given in Table A.1.

### Variable Section Wing - Linear

$$\begin{aligned}
A(\chi) &\approx \left| -\frac{1}{2}\chi + \left( 1 - \frac{2}{\pi} \right) \chi^2 + \left( \frac{4}{3\pi} - \frac{1}{2} \right) \chi^3 \right. \\
&+ \left. \frac{2}{3\pi} \frac{\chi}{\chi_s} - \frac{2}{3\pi} \frac{\chi - \chi_s}{\chi_s} \text{step}(\chi - \chi_s) \right| \frac{|L|}{\sigma_{\max}} \frac{\lambda_0 \Delta^2}{(t/c)} \\
&+ \frac{1}{3\pi} \frac{\Delta}{\gamma_{s,0}} [1 - \text{step}(\chi - \chi_s)] \frac{|L|}{\sigma_{\max}}
\end{aligned} \tag{A.180}$$

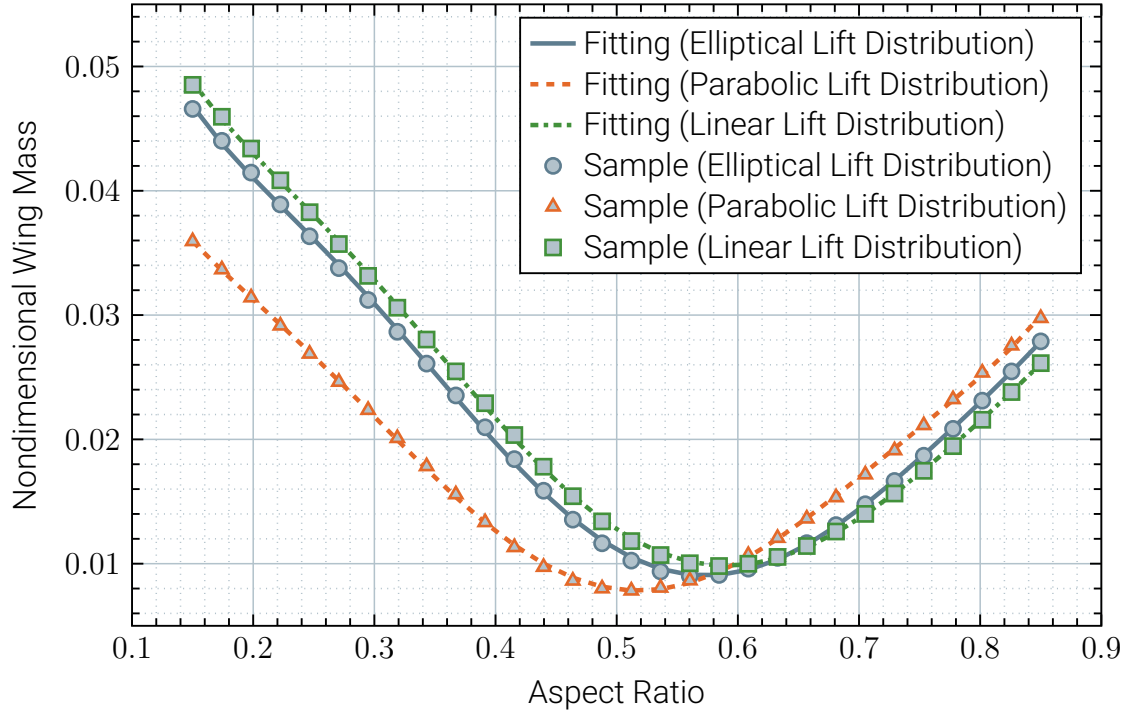


Figure A.7: Numerical integration of  $I_P(\chi_s)$ ,  $I_E(\chi_s)$  and  $I_L(\chi_s)$  together with their correspondent polynomial interpolations.

$$\begin{aligned}
 m_w &= \int_0^1 \rho A(\chi) b d\chi \approx \frac{\rho}{\sigma_{\max}} \frac{\sqrt{\lambda_0^3} \Delta^3}{(t/c)} \sqrt{S} |L| \int_0^1 \left| -\frac{1}{2}\chi + \left(1 - \frac{2}{\pi}\right)\chi^2 \right. \\
 &\quad \left. + \left(\frac{4}{3\pi} - \frac{1}{2}\right)\chi^3 + \frac{2}{3\pi} \frac{\chi}{\chi_s} - \frac{2}{3\pi} \frac{\chi - \chi_s}{\chi_s} \text{step}(\chi - \chi_s) \right| d\chi \\
 &\quad + \frac{1}{3\pi} \chi_s \frac{\Delta^2}{\gamma_{s,0}} \frac{\rho}{\sigma_{\max}} \sqrt{\lambda_0} \sqrt{S} |L| \\
 &\approx \frac{\rho}{\sigma_{\max}} \frac{\sqrt{\lambda_0^3} \Delta^3}{(t/c)} \sqrt{S} |L| I_L(\chi_s) + \frac{1}{3\pi} \chi_s \frac{\Delta^2}{\gamma_{s,0}} \frac{\rho}{\sigma_{\max}} \sqrt{\lambda_0} \sqrt{S} |L|
 \end{aligned} \tag{A.181}$$

Unfortunately this last integral requires a numerical solution, but later on the results are interpolated with polynomials and their coefficients are given in Table A.1.

### Integrals Interpolations

Integrals  $I_P(\chi_s)$ ,  $I_E(\chi_s)$  and  $I_L(\chi_s)$  have been integrated numerically for various values of  $\chi_s$ . The resulting functions have been interpolated using a sixth order polynomial in the form of:

$$I(\chi_s) = C_6 + C_5\chi_s + C_4\chi_s^2 + C_3\chi_s^3 + C_2\chi_s^4 + C_1\chi_s^5 + C_0\chi_s^6 \tag{A.182}$$

Figure A.7 shows the results of numerical integration and the corresponding polynomial interpolations. Table A.1 contains the coefficients of the polynomials.

	$C_0$	$C_1$	$C_2$	$C_3$	$C_4$	$C_5$	$C_6$
$I_P$	7.3729	-21.8847	24.8689	-13.4524	3.6813	-0.5827	0.0749
$I_E$	6.9733	-22.5414	28.1720	-16.9872	5.2202	-0.8854	0.1069
$I_L$	5.4573	-18.0120	22.9419	-14.0406	4.3651	-0.7638	0.1022

Table A.1: Coefficients resulting from interpolation of  $I_P$ ,  $I_E$  and  $I_L$ , computed through numerical integration for various  $\chi_s$ .

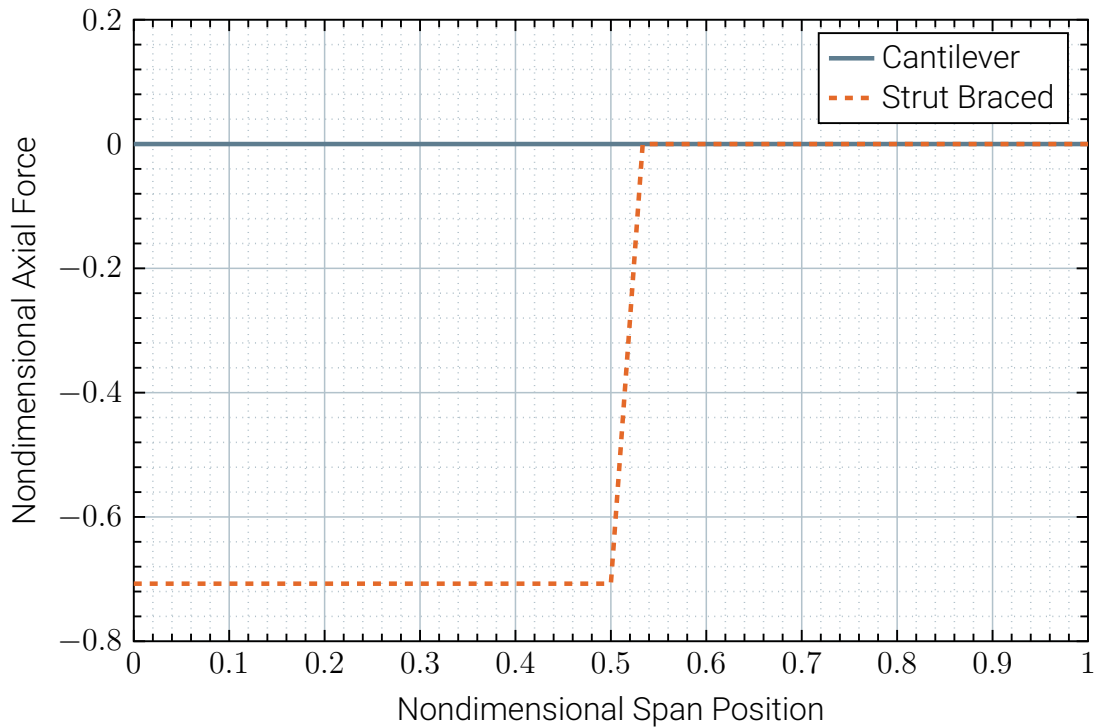


Figure A.8: Nondimensional axial force comparison.

## A.4. Comparison

In this section various results of the cantilever wing are compared with those of the strut-braced wing.

**Axial Force.** Figure A.8 shows a comparison of nondimensional axial forces between cantilever and strut braced wings, in case with elliptical lift distribution with  $\chi_s = 0.5$ ,  $\gamma_{s,0} = 0.15$  and  $\Delta = 1$ .

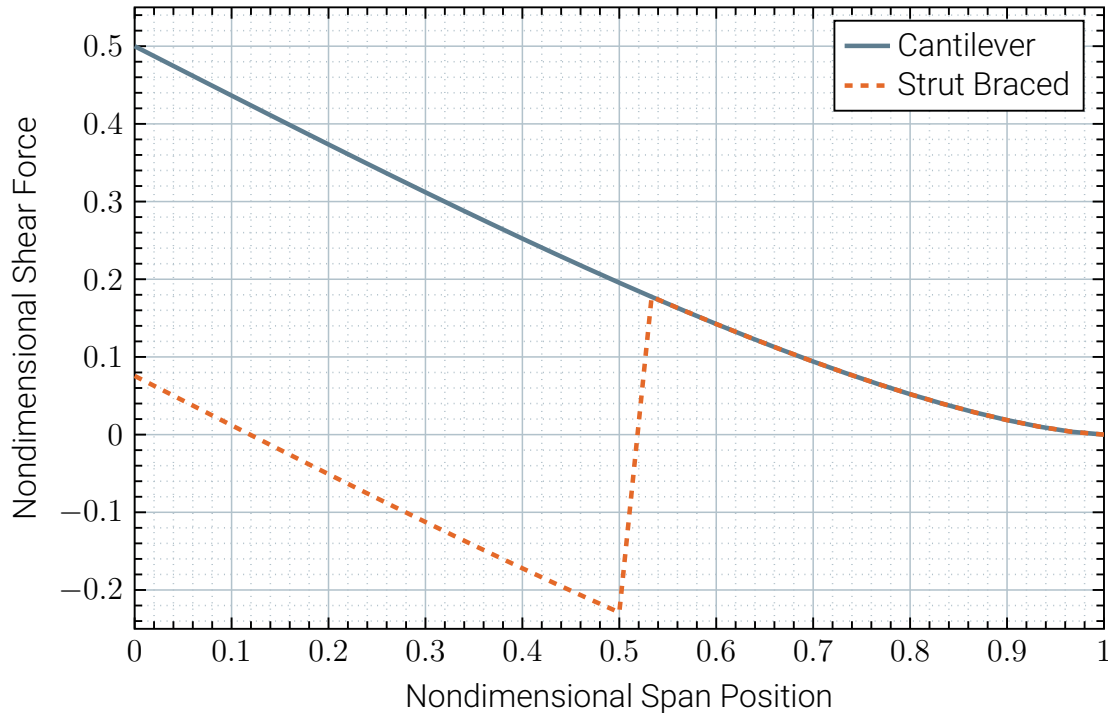


Figure A.9: Nondimensional shear force comparison.

**Shear Force.** Figure A.9 shows a comparison of nondimensional shear forces of cantilever and strut braced wings, in case of elliptical lift distribution with  $\chi_s = 0.5$ .

**Bending Moment.** Figure A.10 shows a comparison of nondimensional bending moment of cantilever and strut braced wings, in case of elliptical lift distribution with  $\chi_s = 0.5$ .

**Stress.** Figure A.11 shows a comparison between the nondimensional stress of cantilever and strut braced wing, in case of elliptical lift distribution with  $\chi_s = 0.5$ ,  $\gamma_{s,0} = 0.15$ ,  $\Delta = 1$ ,  $\lambda_0 = 9$  and  $(t/c) = 0.12$ .

**Mass.** Figure A.12 shows a comparison between the nondimensional wing mass of cantilever and strut braced wings, in case of elliptical lift distribution with  $\chi_s = 0.5$ ,  $\gamma_{s,0} = 0.15$ ,  $\lambda_0 = 9$  and  $(t/c) = 0.12$ .

## A.5. Validation

The validation presented in Section 5.3 involves statistical equations gathered from literature, specifically from [22], [65] and [67]. For the sake of completeness those equations are reported below.

**Important note:** The statistical equations have been copied as they are, so refer to Table A.2 for nomenclature and units adopted in them. Do not consider this nomenclature and units valid elsewhere in the document, and do not consider the nomenclature adopted in the rest of the document valid within these statistical equations.

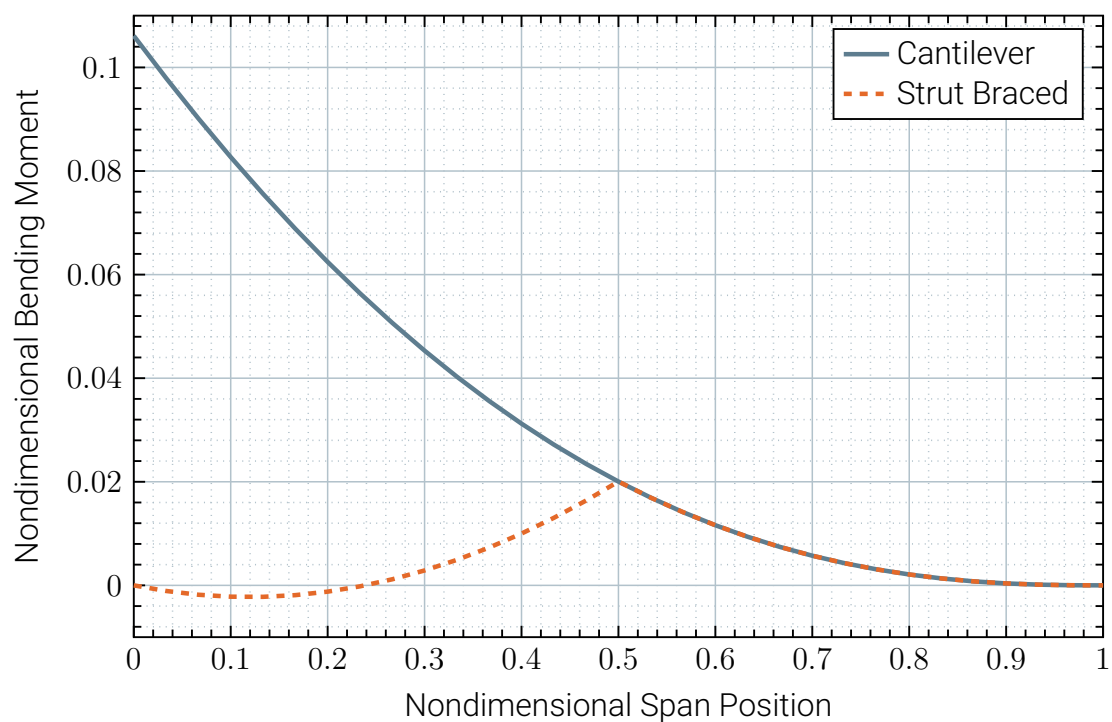


Figure A.10: Nondimensional bending moment comparison.

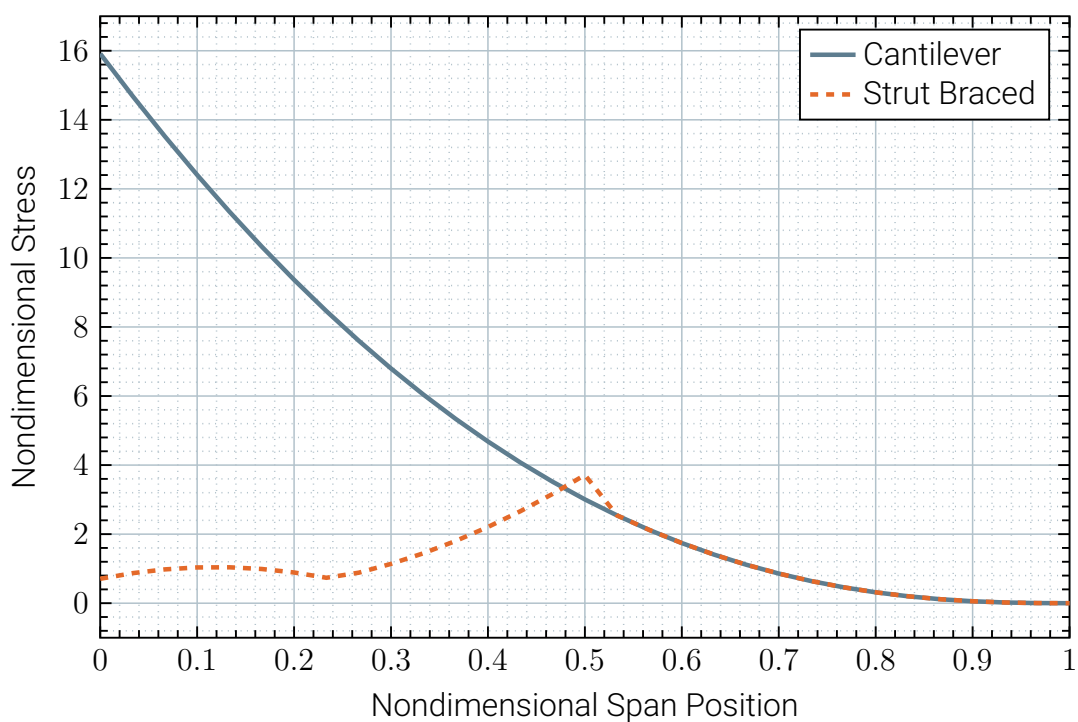


Figure A.11: Nondimensional stress comparison.

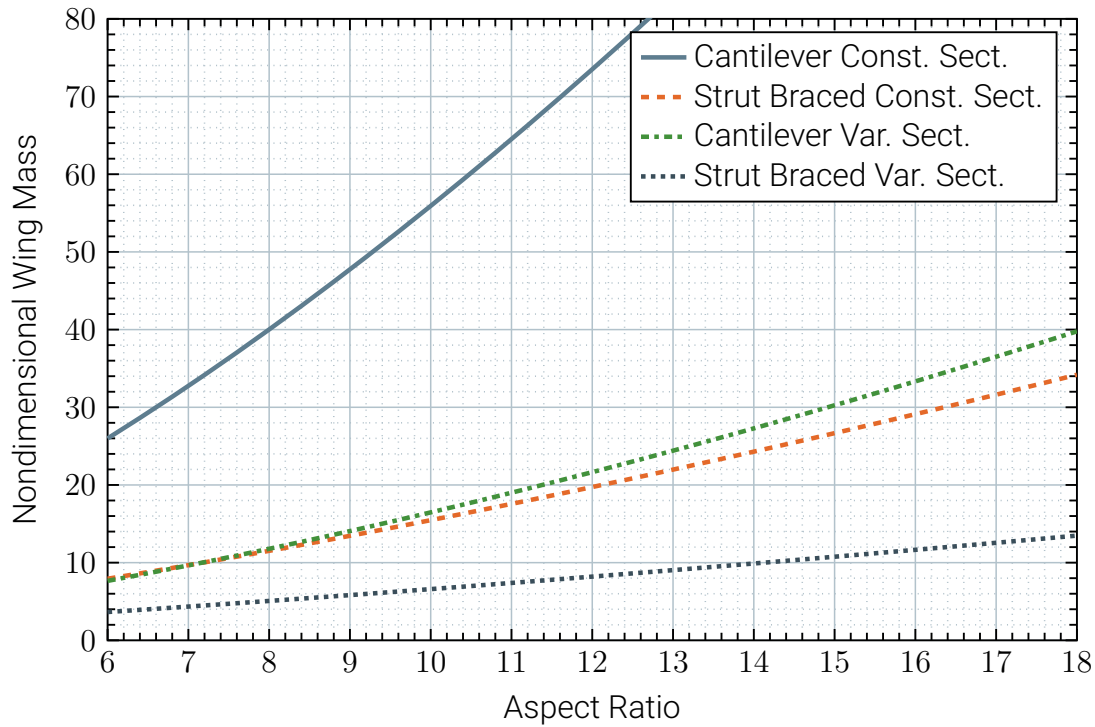


Figure A.12: Nondimensional wing assembly mass comparison (including struts).

Symbol	Units	Description
$S$	ft <sup>2</sup>	Wing area
$A$	-	Aspect ratio
$M_H$	-	Maximum level Mach number at sea level
$W_{TO}$	lbs	Take-off mass
$n_{ult}$	-	Design ultimate load factor
$\lambda$	-	Wing taper ratio
$(t/c)_m$	-	Maximum wing thickness ratio
$\Lambda_{1/2}$	deg	Wing semi-chord sweep angle
$W_{MZF}$	lbs	Maximum zero fuel mass ( $W_{TO} - W_F$ )
$b$	ft	Wing span
$t_r$	ft	Maximum thickness of wing root chord
$W_{dg}$	lbs	Design flight gross mass
$N_z$	-	Ultimate load factor
$S_w$	ft <sup>2</sup>	Trapezoidal wing area
$(t/c)_{root}$	-	Thickness-to-chord ratio at root
$S_{csw}$	ft <sup>2</sup>	Control surface area (wing-mounted, includes flaps)
MAC	ft	Mean Aerodynamic Chord
$(\frac{t}{c})_{max}$	-	Maximum thickness-to-chord ratio
$\rho_{mat}$	lbs/ft <sup>3</sup>	Density of construction material
$AR$	-	Aspect ratio
$K_\rho$	-	Parameter "wing density factor", see values in [67]
$g$	ft/s <sup>2</sup>	Gravitational acceleration

Table A.2: Nomenclature and units adopted *only* for the statistical equations.

**GD Method.** Wing mass statistical equation [22].

$$W_W = \frac{0.00428(S^{0.48})(A)(M_H)^{0.43}(W_{TO}n_{ult})^{0.84}(\lambda)^{0.14}}{[100(t/c)_m]^{0.76}(\cos \Lambda_{1/2})^{1.54}} \quad (A.183)$$

**Torenbeek.** Wing mass statistical equation [22].

$$W_W = 0.0017 W_{MZF} (b/\cos \Lambda_{1/2})^{0.75} [1 + \{6.3 \cos(\Lambda_{1/2})/b\}^{1/2}] \times (n_{ult})^{0.55} (bS/t_r W_{MZF} \cos \Lambda_{1/2})^{0.30} \quad (A.184)$$

**Raymer.** Wing mass statistical equation [65].

$$W_{wing} = 0.0051(W_{dg}N_z)^{0.557} S_w^{0.649} A^{0.5} (t/c)_{root}^{-0.4} (1 + \lambda)^{0.1} \times (\cos \Lambda)^{-1.0} S_{CSW}^{0.1} \quad (A.185)$$

**Sadraey.** Wing *weight* statistical equation [67], note that this equation may be employed in both SI and British units and that it yields the wing weight, not the wing mass as it was for the other equations.

$$W_W = S_W \cdot MAC \cdot \left(\frac{t}{C}\right)_{max} \cdot \rho_{mat} \cdot K_\rho \cdot \left(\frac{AR \cdot n_{ult}}{\cos(\Lambda_{0.25})}\right)^{0.6} \cdot \lambda^{0.04} \cdot g \quad (A.186)$$

**Cessna Method - Cantilever Wing.** Wing mass statistical equation [22], refer to Table A.2 for nomenclature and units.

$$W_W = 0.04674 (W_{TO})^{0.397} (S)^{0.360} (n_{ult})^{0.397} (A)^{1.712} \quad (A.187)$$

**Cessna Method - Strut Braced Wing.** Wing mass statistical equation [22], refer to Table A.2 for nomenclature and units.

$$W_W = 0.002933 (S)^{1.018} (A)^{2.473} (n_{ult})^{0.611} \quad (A.188)$$

## A.6. Others

### A.6.1. Displacements

#### Cantilever - Parabolic Lift Distribution

$$EJ_0 w''(x) = M(x) \quad EJ_0 w'(0) = 0, \quad EJ_0 w(0) = 0 \quad (A.189)$$

$$\begin{aligned} EJ_0 w'(x) &= EJ_0 w'(0) + \int_0^x M(\xi) d\xi \\ &= L \left( \frac{3}{64} b_0 x - \frac{1}{16} x^2 + \frac{1}{32} \frac{x^3}{b_0} - \frac{1}{320} \frac{x^5}{b_0^3} \right) \\ &= L b_0^2 \left( \frac{3}{64} \chi - \frac{1}{16} \chi^2 + \frac{1}{32} \chi^3 - \frac{1}{320} \chi^5 \right) \end{aligned} \quad (A.190)$$

$$\begin{aligned}
EJ_0w(x) &= EJ_0w(0) + \iint_0^x M(\xi)d\xi^2 \\
&= L \left( \frac{3}{256}b_0x^2 - \frac{1}{96}x^3 + \frac{1}{256}\frac{x^4}{b_0} - \frac{1}{3840}\frac{x^6}{b_0^3} \right) \quad (A.191)
\end{aligned}$$

$$\begin{aligned}
&= Lb_0^3 \left( \frac{3}{256}\chi^2 - \frac{1}{96}\chi^3 + \frac{1}{256}\chi^4 - \frac{1}{3840}\chi^6 \right) \\
w'(\chi) &= \frac{Lb_0^2}{EJ_0} \left( \frac{3}{64}\chi - \frac{1}{16}\chi^2 + \frac{1}{32}\chi^3 - \frac{1}{320}\chi^5 \right) \quad (A.192)
\end{aligned}$$

$$w(\chi) = \frac{Lb_0^3}{EJ_0} \left( \frac{3}{256}\chi^2 - \frac{1}{96}\chi^3 + \frac{1}{256}\chi^4 - \frac{1}{3840}\chi^6 \right) \quad (A.193)$$

### Strut Braced - Parabolic Lift Distribution

**Wing.** Vertical displacement of the wing, only bending moment is taken into account and the strut displacement is neglected.

$$EJw''(x) = M(x) \quad EJw(0) = 0, \quad EJw(b_s) = 0 \quad (A.194)$$

$$\begin{aligned}
EJw'(x) &= EJw'(0) + \int_0^x M(\xi)d\xi \\
&= EJw'(0) + \left( -\frac{1}{16}\chi^2 + \frac{1}{32}\chi^3 - \frac{1}{320}\chi^5 + \frac{3}{128}\frac{\chi^2}{\chi_s} \right. \\
&\quad \left. - \frac{3}{128}\frac{(\chi - \chi_s)^2}{\chi_s}\text{step}(\chi - \chi_s) \right) Lb^2 \quad (A.195)
\end{aligned}$$

$$\begin{aligned}
EJw(x) &= EJw(0) + \iint_0^x M(\xi)d\xi^2 \\
&= EJw'(0)\frac{1}{2}b\chi + \left( -\frac{1}{96}\chi^3 + \frac{1}{256}\chi^4 - \frac{1}{3840}\chi^6 + \frac{1}{256}\frac{\chi^3}{\chi_s} \right. \\
&\quad \left. - \frac{1}{256}\frac{(\chi - \chi_s)^3}{\chi_s}\text{step}(\chi - \chi_s) \right) Lb^3 \quad (A.196)
\end{aligned}$$

$$EJw(b_s) = 0 \rightarrow EJw'(0) = \left( \frac{1}{48}\chi_s^2 - \frac{1}{128}\chi_s^3 + \frac{1}{1920}\chi_s^5 - \frac{1}{128}\chi_s \right) Lb^2 \quad (A.197)$$

$$\begin{aligned}
w'(\chi) &= \frac{Lb^2}{EJ} \left( \frac{1}{48}\chi_s^2 - \frac{1}{128}\chi_s^3 + \frac{1}{1920}\chi_s^5 - \frac{1}{128}\chi_s - \frac{1}{16}\chi^2 + \frac{1}{32}\chi^3 - \frac{1}{320}\chi^5 \right. \\
&\quad \left. + \frac{3}{128}\frac{\chi^2}{\chi_s} - \frac{3}{128}\frac{(\chi - \chi_s)^2}{\chi_s}\text{step}(\chi - \chi_s) \right) \quad (A.198)
\end{aligned}$$

$$\begin{aligned}
w(\chi) &= \frac{Lb^3}{EJ} \left[ \left( \frac{1}{96}\chi_s^2 - \frac{1}{256}\chi_s^3 + \frac{1}{3840}\chi_s^5 - \frac{1}{256}\chi_s \right) \frac{1}{2}\chi - \frac{1}{96}\chi^3 + \frac{1}{256}\chi^4 \right. \\
&\quad \left. - \frac{1}{3840}\chi^6 + \frac{1}{256}\frac{\chi^3}{\chi_s} - \frac{1}{256}\frac{(\chi - \chi_s)^3}{\chi_s}\text{step}(\chi - \chi_s) \right] \quad (A.199)
\end{aligned}$$

$$u_w = \frac{Nx}{EA} = \frac{3}{32}\frac{\Delta}{\gamma_{s,0}}(\text{step}(\chi - \chi_s) - 1)\frac{Lb}{EA}\chi \quad (A.200)$$



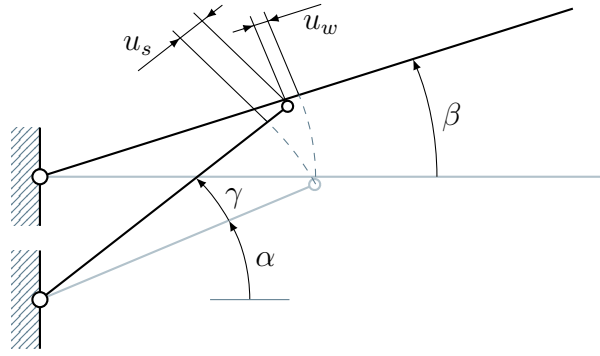


Figure A.13: Effect of the axial displacement of wing and strut on vertical displacement of the wing.

**Strut.** Axial displacement of the strut.

$$u_s = \frac{N_s x}{EA_s} = \frac{3}{32} \frac{\gamma_{s,0}^2 + \Delta^2 \chi_s^2}{\chi_s \gamma_{s,0} \Delta} \frac{Lb}{EA_s} \chi \quad (\text{A.201})$$

**Complete.** The contribution to the vertical displacement of the wing given by the axial displacement of the strut is added. Figure A.13 shows the effect of the axial displacements of wing and strut on the vertical displacement of the wing.

$$C = \langle (b_s + u_w) \cos \beta, (b_s + u_w) \sin \beta \rangle \quad (\text{A.202a})$$

$$C = \langle (\ell_s + u_s) \cos(\alpha + \gamma), (\ell_s + u_s) \sin(\alpha + \gamma) - h_s \rangle \quad (\text{A.202b})$$

$$(b_s + u_w) \cos \beta = (\ell_s + u_s) \cos(\alpha + \gamma) \quad (\text{A.203a})$$

$$(b_s + u_w) \sin \beta = (\ell_s + u_s) \sin(\alpha + \gamma) - h_s \quad (\text{A.203b})$$

$$\cos(\alpha + \gamma) = \cos \alpha \cos \gamma - \sin \alpha \sin \gamma \approx \cos \alpha - \gamma \sin \alpha \quad (\text{A.204a})$$

$$\sin(\alpha + \gamma) = \sin \alpha \cos \gamma + \cos \alpha \sin \gamma \approx \sin \alpha + \gamma \cos \alpha \quad (\text{A.204b})$$

$$\cos \beta \approx 1 \quad (\text{A.204c})$$

$$\sin \beta \approx \beta \quad (\text{A.204d})$$

$$(b_s + u_w) = (\ell_s + u_s) \cos \alpha - (\ell_s + u_s) \gamma \sin \alpha \quad (\text{A.205a})$$

$$(b_s + u_w) \beta = (\ell_s + u_s) \sin \alpha + (\ell_s + u_s) \gamma \cos \alpha - h_s \quad (\text{A.205b})$$

$$\gamma = \frac{(\ell_s + u_s) \cos \alpha - (b_s + u_w)}{(\ell_s + u_s) \sin \alpha} \quad (\text{A.206a})$$

$$\beta = \frac{(\ell_s + u_s) \sin \alpha - h_s}{b_s + u_w} + \frac{(\ell_s + u_s) \cos \alpha}{b_s + u_w} \gamma \quad (\text{A.206b})$$

Recall that  $\cos \alpha = b_s/\ell_s$  and  $\sin \alpha = h_s/\ell_s$ , the equation for  $\beta$  becomes:

$$\begin{aligned}
 \beta &= \frac{(\ell_s + u_s) \sin \alpha - h_s}{b_s + u_w} + \frac{(\ell_s + u_s) \cos \alpha}{b_s + u_w} \frac{(\ell_s + u_s) \cos \alpha - (b_s + u_w)}{(\ell_s + u_s) \sin \alpha} \\
 &= \frac{\ell_s + u_s}{b_s + u_w} \frac{h_s}{\ell_s} - \frac{h_s}{b_s + u_w} + \frac{\ell_s + u_s}{b_s + u_w} \frac{b_s^2}{h_s \ell_s} - \frac{b_s}{h_s} \\
 &= \frac{1}{b_s + u_w} \frac{1}{h_s} \left[ u_s \frac{h_s^2}{\ell_s} + (\ell_s + u_s) \frac{b_s^2}{\ell_s} - b_s(b_s + u_w) \right] \\
 &= \frac{1}{b_s + u_w} \frac{1}{h_s} \left[ u_s \left( \frac{h_s^2}{\ell_s} + \frac{b_s^2}{\ell_s} \right) - b_s u_w \right] = \frac{u_s \ell_s - u_w b_s}{h_s b_s + h_s u_w}
 \end{aligned} \tag{A.207}$$

$$w_0 = \beta x \tag{A.208}$$

Wing section is sized to withstand bending loads, hence it is very stiff with respect to axial loads and it may be possible to consider  $u_w \approx 0$ , in this case:

$$\beta \approx \frac{\ell_s}{h_s b_s} u_s \approx \frac{3}{32} \frac{\sqrt{(\gamma_{s,0}^2 + \Delta^2 \chi_s^2)^3}}{\chi_s^2 \gamma_{s,0}^2 \Delta} \frac{L}{EA_s} \tag{A.209}$$

$$w_0 = \beta x \approx \frac{3}{32} \frac{\sqrt{(\gamma_{s,0}^2 + \Delta^2 \chi_s^2)^3}}{\chi_s^2 \gamma_{s,0}^2 \Delta} \frac{L}{EA_s} x \approx \frac{3}{32} \frac{\sqrt{(\gamma_{s,0}^2 + \Delta^2 \chi_s^2)^3}}{\chi_s^2 \gamma_{s,0}^2 \Delta} \frac{Lb}{EA_s} \chi \tag{A.210}$$

## A.6.2. Mass comparison coefficient

### Definitions

The mass comparison coefficient compares the mass of the wing assembly of a strut braced wing  $m_{wa} = m_w + m_s$  with the mass of a cantilever wing  $m_0$ . The comparison considers same wing surface  $S$ , same thickness-to-chord ratio ( $t/c$ ), same sizing lift  $L$  and same material, which means same  $\sigma_{\max}$  and  $\rho$ . The parameter  $\Delta = b/b_0$  allows to compare wings with different span.

$$\kappa_{m,w} = \frac{m_w}{m_0} \tag{A.211}$$

$$\kappa_{m,s} = \frac{m_s}{m_0} \tag{A.212}$$

$$\kappa_m = \frac{m_{wa}}{m_0} = \frac{m_w}{m_0} + \frac{m_s}{m_0} \tag{A.213}$$

Various mass comparison coefficients can be calculated, by combining different load distributions and different criteria for sizing the resisting section. In the following part only mass comparison coefficients calculated with same sizing criteria and same load distribution are shown.

The mass comparison coefficient depends only on geometrical quantities:

$$\kappa_m = \kappa_m(\Delta, \chi_s, \gamma_{s,0}, (t/c), \lambda_0) \tag{A.214}$$

In order to simplify the notation in the expressions for the mass coefficients consider the following definitions:

$$U_w = \frac{\rho}{\sigma_{\max}} \frac{\sqrt{\lambda_0^3}}{(t/c)} \sqrt{S} |L| \quad (\text{A.215})$$

$$U_s = \frac{\rho}{\sigma_{\max}} \sqrt{\lambda_0} \sqrt{S} |L| \quad (\text{A.216})$$

$$U_r = \frac{U_s}{U_w} = \frac{(t/c)}{\lambda_0} \quad (\text{A.217})$$

### Constant section wing - parabolic

$$\begin{aligned} \kappa_m &= \frac{m_w}{m_0} + \frac{m_s}{m_0} \\ &\approx \left( -\frac{8}{3} \chi_s + 2\chi_s^2 - \frac{1}{3} \chi_s^4 + 1 \right) \Delta^3 + \frac{1}{2} \frac{\Delta^2}{\gamma_{s,0}} U_r + \frac{\gamma_{s,0} + \Delta^2 \chi_s^2}{\gamma_{s,0} \chi_s} U_r \end{aligned} \quad (\text{A.218})$$

### Constant section wing - elliptical

$$\begin{aligned} \kappa_m &\approx \left[ \frac{3}{2} \left( \chi_s \arcsin \chi_s + \sqrt{1 - \chi_s^2} \right) + \frac{1}{2} (\chi_s^2 - 1) \sqrt{1 - \chi_s^2} - \frac{3\pi}{4} \chi_s \right] \Delta^3 \\ &+ \frac{1}{2} \frac{\Delta^2}{\gamma_{s,0}} U_r + \frac{\gamma_{s,0} + \Delta^2 \chi_s^2}{\gamma_{s,0} \chi_s} U_r \end{aligned} \quad (\text{A.219})$$

### Constant section wing - linear

$$\begin{aligned} \kappa_m &\approx \left[ -\frac{3\pi}{4} \chi_s + \left( \frac{3\pi}{2} - 2 \right) \chi_s^2 + \left( 2 - \frac{3\pi}{4} \right) \chi_s^3 + 1 \right] \Delta^3 \\ &+ \frac{1}{2} \frac{\Delta^2}{\gamma_{s,0}} U_r + \frac{\gamma_{s,0} + \Delta^2 \chi_s^2}{\gamma_{s,0} \chi_s} U_r \end{aligned} \quad (\text{A.220})$$

### Variable section wing - parabolic

$$\kappa_m \approx 20I_P(\chi_s) \Delta^3 + \frac{15}{8} \chi_s \frac{\Delta^2}{\gamma_{s,0}} U_r + \frac{15}{4} \frac{\gamma_{s,0}^2 + \Delta^2 \chi_s^2}{\gamma_{s,0} \chi_s} U_r \quad (\text{A.221})$$

### Variable section wing - elliptical

$$\kappa_m \approx 16I_E(\chi_s) \Delta^3 + \frac{16}{3\pi} \chi_s \frac{\Delta^2}{\gamma_{s,0}} U_r + \frac{32}{3\pi} \frac{\gamma_{s,0}^2 + \Delta^2 \chi_s^2}{\gamma_{s,0} \chi_s} U_r \quad (\text{A.222})$$

### Variable section wing - linear

$$\kappa_m \approx \frac{24\pi}{8-\pi} I_L(\chi_s) \Delta^3 + \frac{8}{8-\pi} \chi_s \frac{\Delta^2}{\gamma_{s,0}} U_r + \frac{16}{8-\pi} \frac{\gamma_{s,0}^2 + \Delta^2 \chi_s^2}{\gamma_{s,0} \chi_s} U_r \quad (\text{A.223})$$

### A.6.3. Weight correction factor

The weight correction factor is defined as:

$$\kappa_w = \frac{m_{empty}}{m_{empty0}} \quad (\text{A.224})$$

where  $m_{empty}$  is the empty mass of the aircraft with strut-braced wing, while  $m_{empty0}$  is the empty mass of the reference aircraft with cantilever wing. These masses can be decomposed as:

$$m_{empty} = m_{aircraft} + m_w \quad (\text{A.225})$$

$$m_{empty0} = m_{aircraft} + m_0 \quad (\text{A.226})$$

assuming that the only difference between the two is the wing mass (including the strut). Substituting in the previous equation, with some steps one obtains:

$$\begin{aligned} \kappa_w &= \frac{m_{empty}}{m_{empty0}} = \frac{m_{aircraft} + m_w}{m_{empty0}} = \frac{m_{aircraft}}{m_{empty0}} + \frac{m_w}{m_{empty0}} \\ &= \frac{m_{empty0} - m_0}{m_{empty0}} + \frac{m_w}{m_{empty0}} \\ &= 1 + \frac{m_0}{m_{empty0}} \left( \frac{m_w}{m_0} - 1 \right) = 1 + \frac{m_0}{m_{empty0}} (\kappa_m - 1) \end{aligned} \quad (\text{A.227})$$

where  $\kappa_m$  is the mass comparison coefficient calculated before, while  $m_{empty0}$  is known for the aircraft (or can be estimated) and  $m_0$  can be estimated with a statistical equation.

### A.6.4. Aerodynamics

#### Zero-Lift Drag Coefficient

The strut adds a contribution to the zero-lift drag coefficient. This contribution can be estimated using an approach suggested by Raymer [65].

$$\Delta C_{D0, strut} = C_{f, strut} F F_{strut} Q_{strut} \frac{S_{wet, strut}}{S_{ref}} \quad (\text{A.228})$$

$$F F_{strut} = \left[ 1 + \frac{0.6}{(x/c)_m} \left( \frac{t}{c} \right) + 100 \left( \frac{t}{c} \right)^4 \right] [1.34 M^{0.18} (\cos \Lambda_m)^{0.28}] \quad (\text{A.229})$$

The boundary layer on the strut is considered to be entirely turbulent and it is assumed that there is any interference drag ( $Q_{strut} = 1$ ).

Type of Surface	Skin Roughness $k$ [m]
Smooth paint	$0.634 \times 10^{-5}$
Production sheet metal	$0.405 \times 10^{-5}$
Polished sheet metal	$0.152 \times 10^{-5}$
Smooth composite	$0.052 \times 10^{-5}$

Table A.3: Skin roughness value for different type of aircraft [65].

The following equations are used to calculate the zero-lift drag coefficient:

$$Re = \frac{\rho \ell V}{\mu} \quad (\text{A.230})$$

$$Ma = \frac{V}{a} = \frac{V}{\sqrt{\gamma R_{air} T}} \quad (\text{A.231})$$

$$C_f = C_{f,turb} = \frac{0.455}{(\log_{10} Re)^{2.58} (1 + 0.144 Ma^2)^{0.65}} \quad (\text{A.232})$$

$$C_{D0} = \sum_i C_{f,i} F F_i Q_i \frac{S_{wet,i}}{S_{ref}} + C_{D0,misc} \quad (\text{A.233})$$

When the skin surface is relatively rough, the flow will be extra turbulent and the friction coefficient will be higher. A cutoff Reynolds number is used instead of the Reynolds number when it is lower:

$$Re = \begin{cases} Re_{cutoff} & Re_{cutoff} \leq Re \\ Re & \end{cases} \quad (\text{A.234})$$

The cutoff Reynolds number is calculated with the following equation, with  $k$  chosen from Table A.3.

$$Re_{cutoff} = 38.21 \left( \frac{\ell}{k} \right)^k \quad (\text{A.235})$$

### Oswald's Factor

The common formulas used to estimate the Oswald's factor are usually not suitable for very high aspect ratio wing. I was not able to find an equation in literature, however in [73] it is presented a graph (copied in Figure A.14) that can be interpolated to be used within a software.

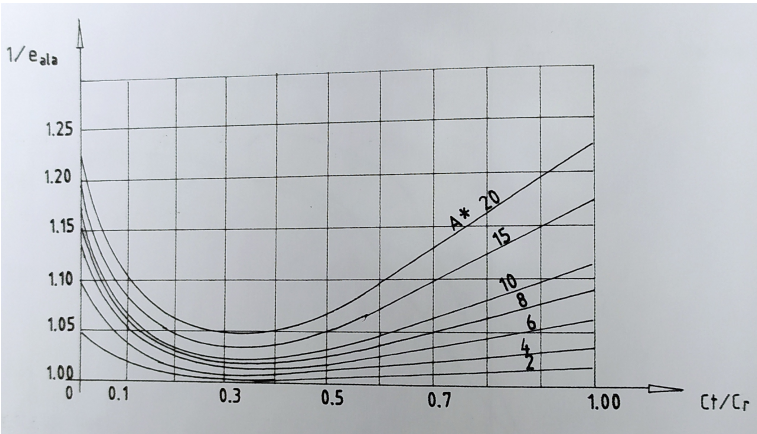


Figure A.14: Oswald's factor of wing, as function of taper ratio for various aspect ratio [73].